High Wall Loading Compact Tokamak Power Reactor - A Scoping Study, Progress Report for the Period 1 December 1983 - 30 September 1984

B. Badger, S.I. Abdel-Khalik, M. El-Afify, H. Attaya, M.L. Corradini, L.A. El-Guebaly, G.A. Emmert, K.Y. Huh, G.L. Kulcinski, E. Larsen, C.W. Maynard, J.F. Santarius, M.E. Sawan, I.N. Sviatoslavsky, W.F. Vogelsang, L.J. Wittenberg

October 1984

UWFDM-592

FUSION TECHNOLOGY INSTITUTE

UNIVERSITY OF WISCONSIN

MADISON WISCONSIN

High Wall Loading Compact Tokamak Power Reactor - A Scoping Study, Progress Report for the Period 1 December 1983 - 30 September 1984

B. Badger, S.I. Abdel-Khalik, M. El-Afify, H. Attaya, M.L. Corradini, L.A. El-Guebaly, G.A. Emmert, K.Y. Huh, G.L. Kulcinski, E. Larsen, C.W. Maynard, J.F. Santarius, M.E. Sawan, I.N. Sviatoslavsky, W.F. Vogelsang, L.J. Wittenberg

Fusion Technology Institute
University of Wisconsin
1500 Engineering Drive
Madison, WI 53706

http://fti.neep.wisc.edu

October 1984

UWFDM-592

HIGH WALL LOADING COMPACT TOKAMAK POWER REACTOR - A SCOPING STUDY

B. Badger, S.I. Abdel-Khalik, H. Attaya, M.L. Corradini, M. El-Afify,
L.A. El-Guebaly, G.A. Emmert, K.Y. Huh, G.L. Kulcinski,
E. Larsen, C.W. Maynard, J.F. Santarius, M.E. Sawan,
I.N. Sviatoslavsky, W.F. Vogelsang, L.J. Wittenberg

Fusion Technology Institute
1500 Johnson Drive
University of Wisconsin-Madison
Madison, Wisconsin 53706

October 1984

UWFDM-592

1. INTRODUCTION AND APPROACH TO THE PROBLEM

For several years it has been recognized that a major advance in tokamak reactor design has been needed in order to make fusion more attractive in the marketplace. The objectives of this fiscal year's work have been to investigate innovations which will produce a more desirable and economical tokamak reactor design. Initially, we have chosen to concentrate on a high beta, high power density but low overall power configuration. Because of the limited nature of this program we were able to investigate only selected aspects of such a reactor design and in no way do we claim that all the ramifications of such a design have been examined. However, we do feel that significant progress has been made toward our initial objective and we expect that future efforts will prove that such an attractive tokamak design can be made.

The overall approach of this year's work was to first use a parametric analysis (see Chapter 2) to establish an aggressive but credible point design which could satisfy the general objective of the study. To that end, we attempted to limit the total thermonuclear power to approximately 1000 MW_{th}. Secondly, we wanted to find a design point which could satisfy that condition at the highest credible power density. Based on past studies of tokamaks with neutron wall loadings of 1 to 4 MW/m^2, we decided to design a 10 MW/m^2 environment which would represent a significant increase over the previous work while still allowing a reasonably credible blanket to be designed. As a third constraint, we decided to work on a preconceptual design in which all of the PF coils (except the inboard bean coil) were placed outside the TF coils. This last constraint turned out to be much more severe than originally thought.

After the initial parametric study established the first order plasma parameters (beta, plasma radii, magnetic fields, etc.) we split our effort into parallel efforts on plasma physics and engineering. On the physics side, we investigated the MHD equilibrium of the proposed plasma and coil configurations which could satisfy our original objectives (see Chapter 3). In a related area, we examined the sensitivity of the plasma scaling laws we were using to the specific models assumed (see Chapter 4).

At the same time we were examining the plasma physics issues, the engineering aspects of high power density blanket designs were being investigated. We were able to evolve a new blanket design which retains many of the safety and simplicity features of our earlier work on WITAMIR and MARS while at the same time demonstrates an ability to operate under high wall loadings (see Chapter 5). This innovative blanket design will work for not only the specific design point in this study but it should have more universal applications in all future compact tokamak systems.

A separate effort was also conducted on finding a high performance shield to protect the inner leg of the superconducting TF coil and also to protect the normal conducting bean coil. A new material, boron hydride, was identified as a potential shield material and more optimum combinations of TiH_2, Pb, and boron/water (see Chapters 6 and 7) were identified as well. The applicability of the advanced shield designs involved in the present work should have implications for even near term devices such as TFCX or INTOR.

In the process of this research, we found it necessary to work with large, cumbersome computer codes for magnetic field, neutronic, and stress analyses. It was difficult to mate the output of these codes so we found it necessary to spend some time coupling codes such as EFFI, MCNP, and NASTRAN

(see Chapter 8). The effort spent in this area was well worth the extra time because now such codes can be applied in future research without delay.

Finally, it was necessary during the course of this contract to assist other U.S. groups working in the area of magnetic fusion. Considerable time and travel expense was incurred in analyzing the RF launchers for INTOR, serving on the advisory board of INTOR, serving on the advisory committees of TFCX and BCSS, assisting LLNL with MARS, as well as giving lesser assistance to GA Technologies (nuclear data), LLNL (FPD), and DOE.

2. PARAMETER SURVEY

To relate and integrate the different tasks in this project, it was required to establish a design point upon which the different tasks would be carried out. The choice of this point was based on an extensive parameter survey in the tokamak design space using the FEDC Tokamak Systems Code (TSC).[1]

2.1 General Criteria for the Design

We have set two criteria for the design. First the system should be compact. A compact system is defined as one which has high power density, high wall loading, and low mass utilization. For the same power, a compact system is significantly smaller than a conventional one. With the right choice of materials in the compact system, the economy of a fusion reactor will be significantly improved.

The second criterion for the design is to aim at a small system, that is small in both the physical size and the output power (~ 1000 MW). Although the "economy of scale" does not favor small systems, a small system has the most important advantage of being affordable because of the small capital cost, and can be completed more quickly.

2.2 Comparison Between Compact and Conventional Systems

To illustrate the differences between conventional and compact systems, Table 2-1 shows some important reactor parameters for the STARFIRE[2] reactor and the RIGGATRON[3] reactor designs. It is evident from the parameter comparison of the conventional design (STARFIRE), and of the extremely compact design (RIGGATRON), that there is a wide range of the design space between these two design points.

Table 2-1. Conventional and Compact Design Parameter Comparison

	STARFIRE	RIGGATRON
β (%)	6.7	20.
Plasma Radius (m)	1.94	0.34
Major Radius (m)	7.00	0.85
Aspect Ratio	3.6	2.5
Max. Field at TF Coil (T)	11.1	10-16 (normal magnet)
Thermal Power (MW_{th})	4033.	1325.
Net Power (MW_e)	1200.	355.
Plasma Power Density (MW/m^3)	4.5	500.
Neutron Wall Loading (MW/m^2)	3.6	68.4
System Power Density (MW_{th}/m^3)	0.3	5.2 (LWR ~ 20)
Mass Utilization (tonne/MW_{th})	4.0	0.28 (LWR ~ .2)

2.3 Scope of the Parameter Survey and the FEDC TSC

As mentioned above there is a wide range in the tokamak design space that has not been invoked before, especially for high power density designs. In our survey we studied the effect of some important parameters on the design space and showed how the fusion power as a function of the aspect ratio changes for different values of: plasma radius, maximum field at the toroidal coil, β (plasma kinetic pressure/magnetic pressure), wall loading, thickness of the inboard shield, etc.

The code that we have used in the parametric survey is the Tokamak Systems Code (TSC), Version 2, of the Fusion Engineering Design Center (FEDC).[1] The code flow diagram is shown in Fig. 2-1. Most of the modules shown in this figure are based on simplified models of the related theories.

The code serves as a good tool for a parametric survey like this one, but certainly its output should be checked with more sophisticated codes, and this will be the subject of Chapter 8.

2.4 Assumptions

Some general assumptions and conditions for the reactors have been established at the beginning of the study. These assumptions and conditions are:

A. Steady State - RF Startup - RF Current Drive

The recent experimental success[4] in using lower hybrid (LH) and ICRF (Ion Cyclotron Radio Frequency) waves in starting and driving the plasma current is very encouraging, and we believe that the steady-state operation of tokamaks using RF is attainable in the future.

The use of RF heating and current drive has the advantage of eliminating the need for using ohmic heating, and thus removes an important constraint on the size of the inner core of the reactor; this is an

TOKAMAK SYSTEMS CODE FLOW DIAGRAM

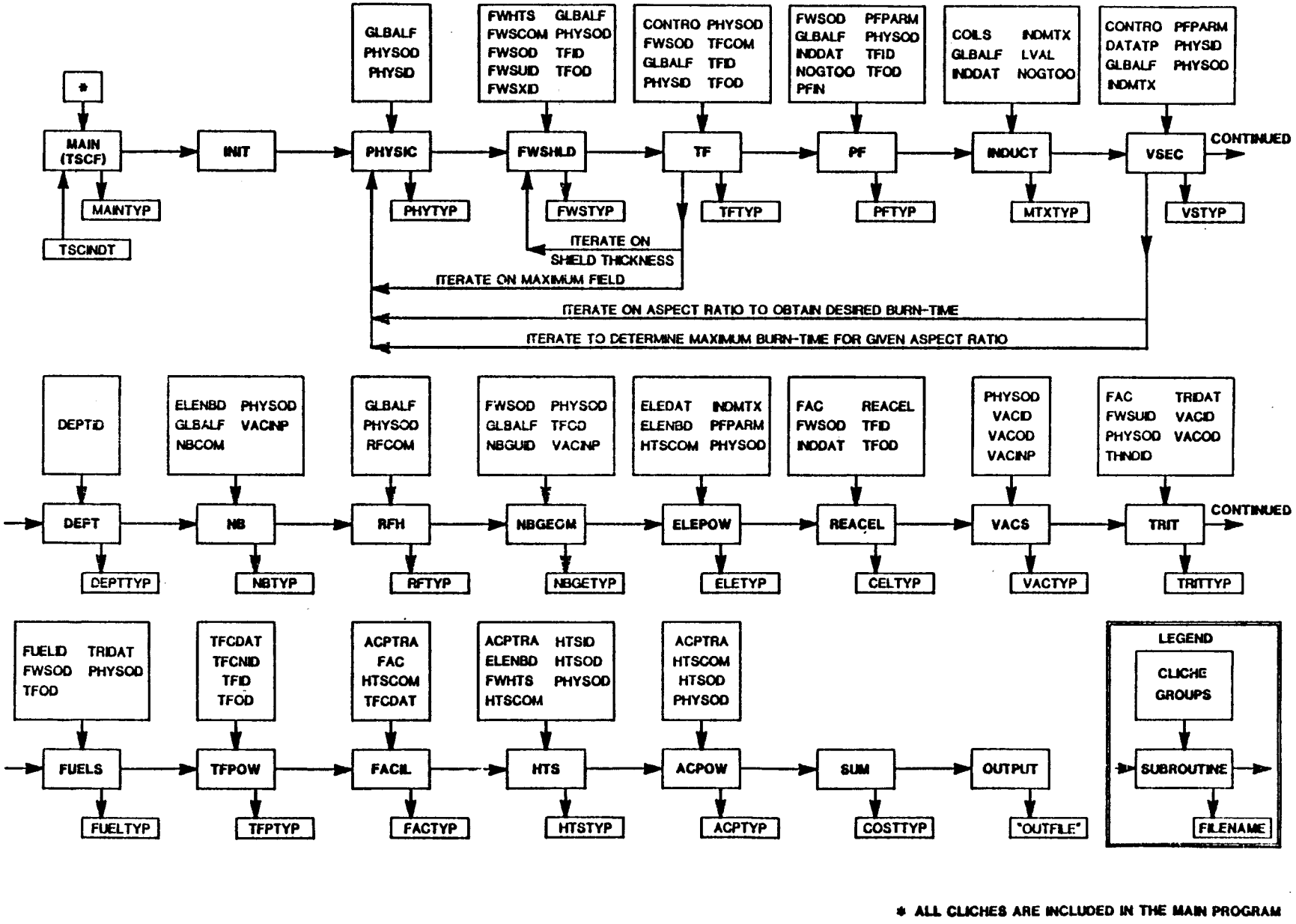

Fig. 2-1. Flow Diagram of the TSC (FEDC).

important step toward a compact and small reactor. On the other hand, since the required RF power is proportional to the plasma volume, small reactors could be ignited with only a few megawatts of supplementary power;[5] thus the use of RF in a small, compact system is favorable.

B. No Inboard Breeding

For a compact small reactor, inboard breeding has two unwanted effects. First it increases the total thickness of the inboard blanket/shield, which means an increase in size of the reactor as well as an increase in the maximum field at the toroidal field magnets. Second, it complicates the design and the maintenance of the reactor. With careful design of the outboard blanket sufficient tritium breeding could be achieved without the need of an inboard breeding blanket.

C. β Values

Recently[6] it has been shown that the β limit could be increased up to 15% in the first stability regime and, with a modest "bean" indentation of about .2, the second stability regime could be accessed in which β might approach 1. In this parameter survey we have covered both regimes, and in this report we show the design space for four values of β, namely 8, 10, 15 and 20%.

D. Fusion Power

As we stated previously, we aimed at the lowest possible fusion power of about 1000 MW. However, for completeness and for the sake of comparison with other designs, and to show how the fusion power changes when one or more parameters change, we covered a wide range of the fusion power (300 $\rightarrow$ 6000 MW).

E. Neutron Wall Loading

A peak value of the neutron wall loading of ~ 10 MW/m^2 at the inboard wall is assumed. An optimized inboard shield thickness that can protect the magnet at this value of the neutron loading was found to be 66 cm. The detailed dimensions from the inner edge of the plasma to the winding pack of the inner leg of the TF coil are shown in Table 2-2.

F. Maximum Field at the TF Magnet

This was limited to a minimum of 10 T (maximum field for NbTi) and to a maximum of 16 T (maximum field for Nb_3Sn).

G. Fixed Plasma Input Parameters

Table 2-3 shows some of the plasma parameters that were assumed fixed in the parametric survey. The choice of these parameters was based on the results and conclusions of previous conceptual designs.

2.5 Results and Discussion

In this section we present some of the results of the parameter survey and show in particular the effect of β, the wall loading, and the inboard shield thickness on the design space. With respect to the wall loading, the independent parameter is the field at the plasma center. We modified the physics module in the TSC so that it iterates on either the field at the plasma center or the aspect ratio (in case the maximum field at the TF magnet is specified) to achieve the required input value of the wall loading. The wall loading is calculated in this code as the neutron fusion power over the plasma surface. The poloidal distribution of the wall loading was found by using the NEWLIT code (see Chapter 8).

Table 2-2. Inboard Dimensions (cm)

Scrapeoff	6
First Wall	1
Shield	66
Gap	3
Cryostat	17
TOTAL	93

Table 2-3. Fixed Plasma Input Parameters

Elongation	1.6
Triangularity	0.3
Safety Factor	2
T_i (keV)	13
T_e (keV)	13
Z_{eff}	1.5
Z_{imp}	8

All of the following figures have the same format, and it might be constructive to explain beforehand this common format. The fusion power is given as a function of the aspect ratio for different plasma radii, and is shown by the solid lines. The value of plasma radius (in cm) and the magnetic field (in tesla) at the major radius are written at the right end of each solid line. The dashed lines are the contours of the maximum field at the TF magnets, the value of which (in tesla) is written at the upper end of each dashed line. In every figure, each point has the same value of β and the same value of neutron wall loading (Γ_{av}). Those are written in the upper caption of the figure. This format proved to be a very handy tool in the design process and allows some degree of freedom in the choice of the required parameters.

A. Effect of β

Figure 2-2 shows the design space for a neutron wall loading of 10 MW/m^2 and for four values of β: 8, 10, 15 and 20%. Each subplot in Fig. 2-2 is shown separately in Fig. 2-2a, 2-2b, 2-2c, and 2-2d. Since the fusion power is proportional to $\beta^2 B^4$, it is clear from Fig. 2-2 that for the same plasma radius and the same power level, an increase of β would decrease the required field at the plasma, the maximum field at the TF magnet (B_{max}), and the aspect ratio. The decrease of B_{max} would make the use of NbTi magnets possible. The general effect of β as seen in this figure is to move the design space toward smaller size and lower power, in accordance with the second general criterion we have for the design (Sec. 2.1).

B. Effect of Wall Loading (Γ_{av})

Figure 2-3 shows the design space for a β value of 10% and for three different values of wall loading (Γ_{av}): 5, 10, 20 MW/m^2. The subplots in

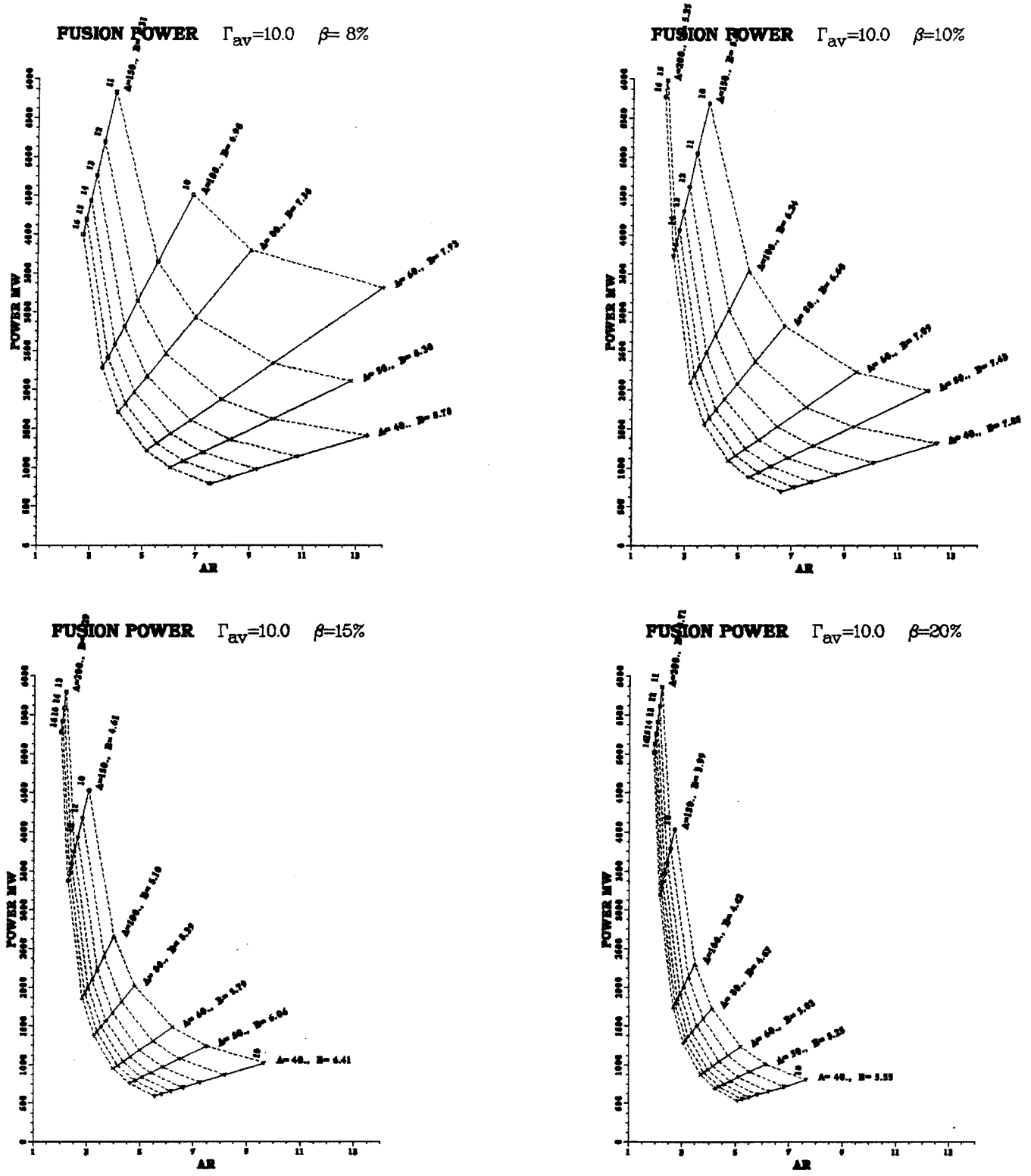

Fig. 2-2. Effect of β, (Γ_{av} = 10 MW/m^2).

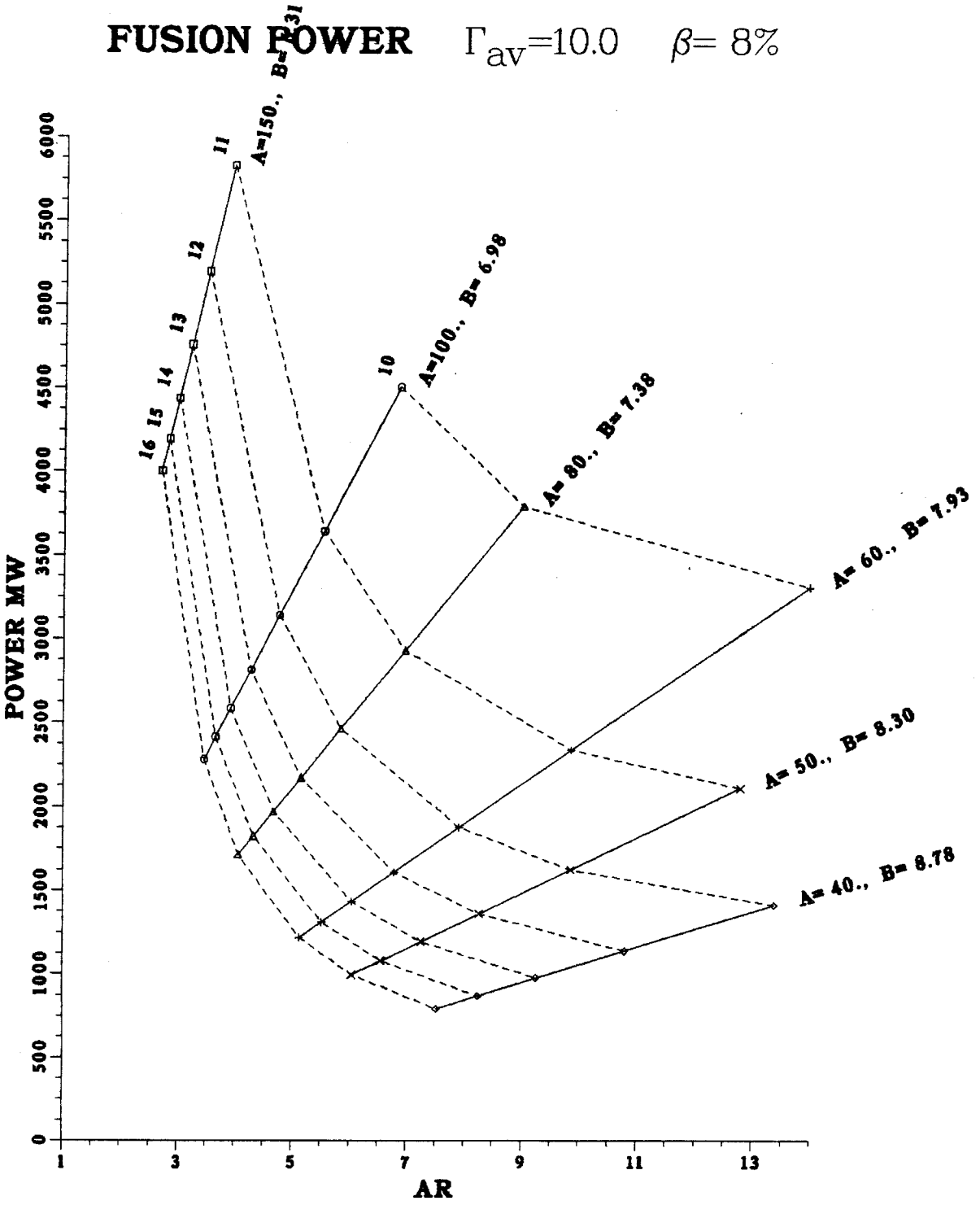

Fig. 2-2a. Case for β = 8%, Γ_{av} = 10 MW/m^2.

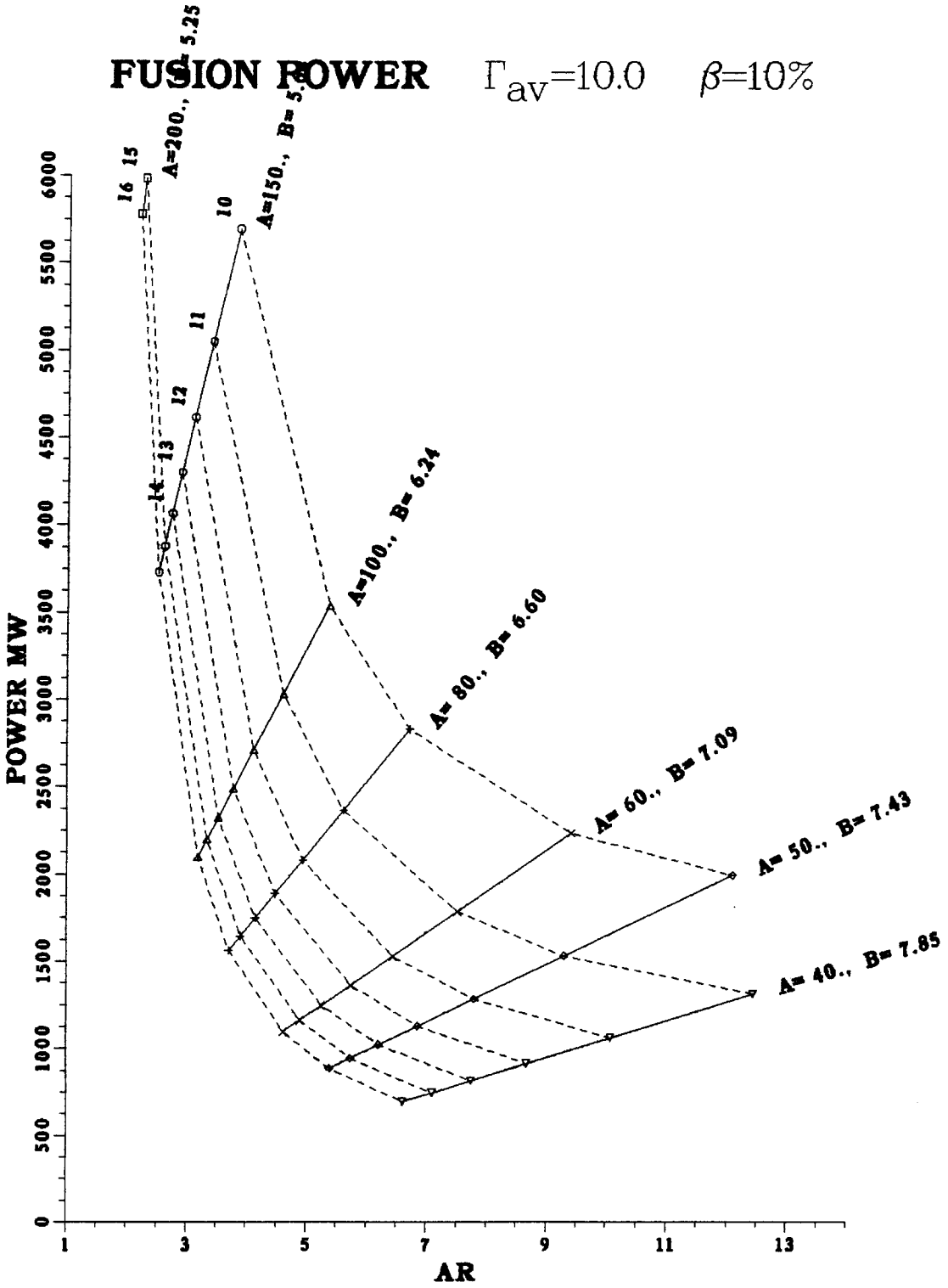

Fig. 2-2b. Case for β = 10%, Γ_{av} = 10 MW/m^2.

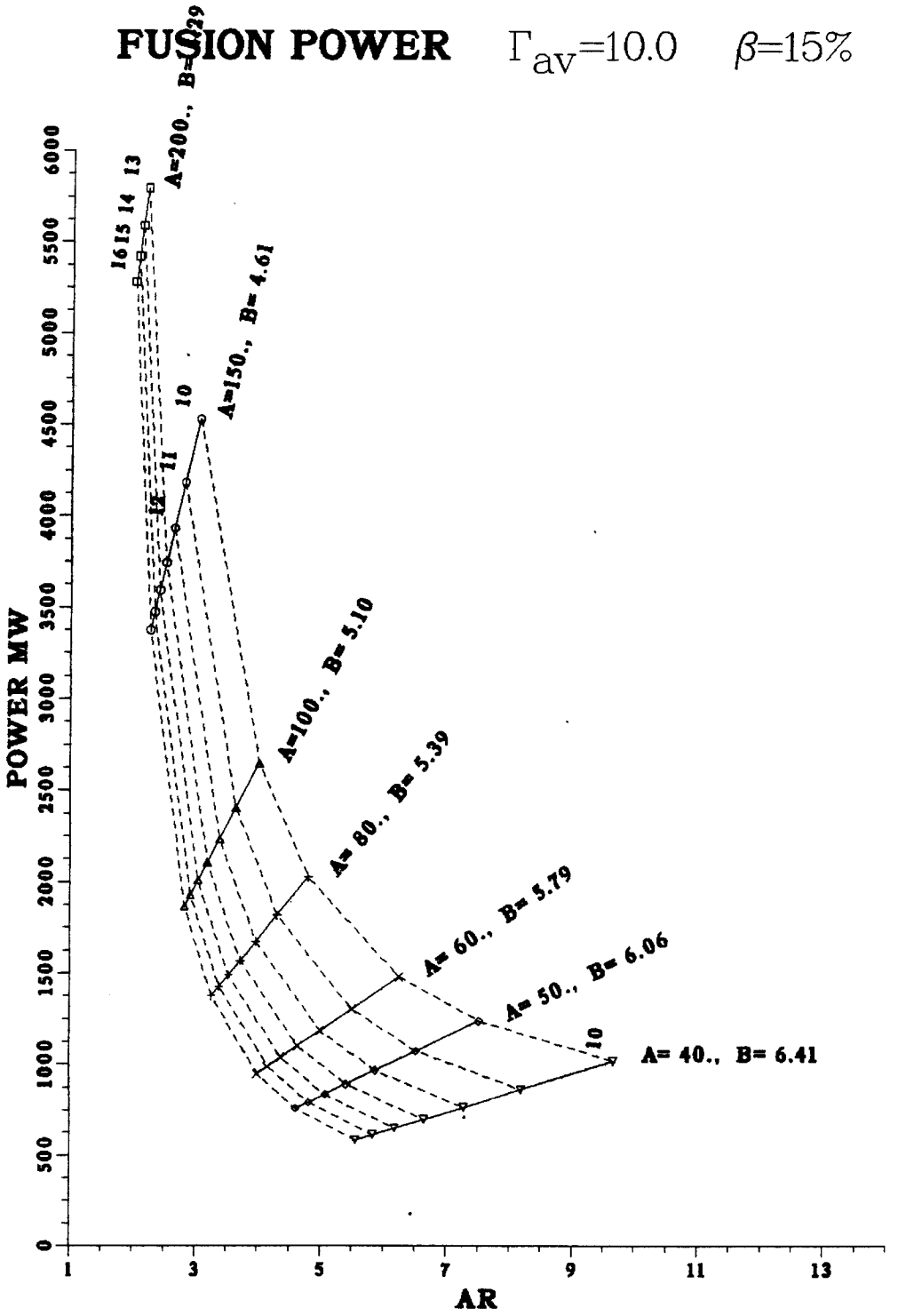

Fig. 2-2c. Case for β = 15%, Γ_{av} = 10 MW/m^2.

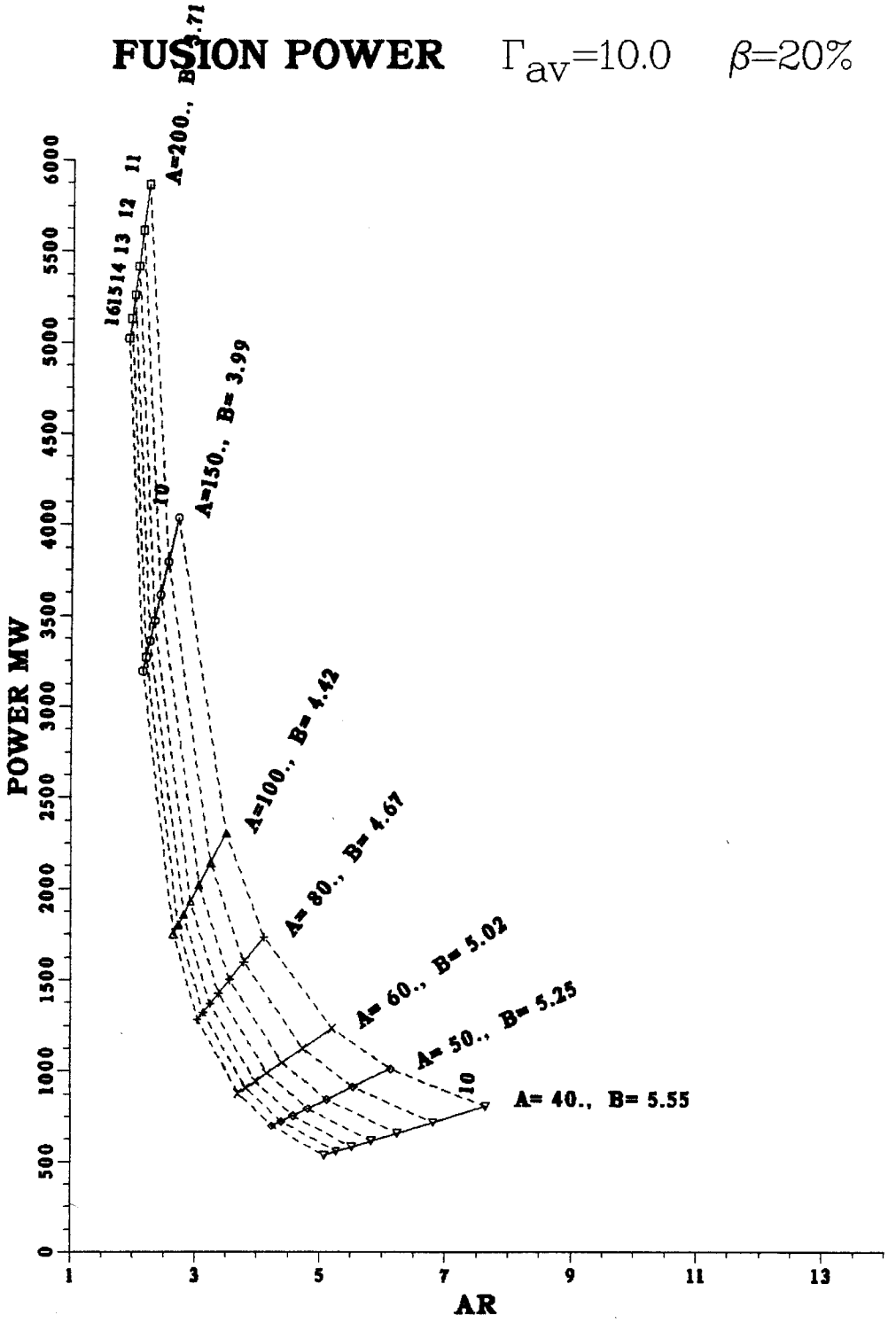

Fig. 2-2d. Case for β = 20%, Γ_{av} = 10 MW/m^2.

Fig. 2-3 are shown in Fig. 2-3a, 2-3b, and 2-3c. The general effect of wall loading (for the same β) is to move the design space towards higher power, larger size, and higher field. It is evident from Fig. 2-3 that the two general criteria of the design, i.e. compactness (higher wall loading) and smallness (of size and power), are not parallel. To have a small reactor with very high wall loading, a very high magnetic field (> 16 T) is required.

C. Effect of the Inboard Shield Thickness

The inboard shield thickness (Δ_s) should be optimized to fully protect the magnet with the least possible thickness. This thickness determines the maximum field at the inner leg of the magnets and/or the field at the plasma center. Consequently the change of Δ_s would affect the design space. To show this effect, we consider two values for Δ_s. Figure 2-4a shows part of the design space for Γ_{av} = 10 MW/m^2, β = 20%, and Δ_s = 66 cm. The design point of the base case is shown by circles. Figure 2-4b shows the design space for the same Γ_{av}, the same β, and Δ_s = 79 cm. To keep the same power, the same plasma radius, and the same aspect ratio, the maximum field will increase from 12.29 T (Δ_s = 66 cm) to 14 T (Δ_s = 79 cm). On the other hand, to keep the same maximum field (12.29 T) and the same plasma radius, the aspect ratio increases from 4.33 (Δ_s = 66 cm) to 4.9 (Δ_s = 79 cm), and the fusion power increases by about 100 MW.

D. Design Base Case

Table 2-4 shows a list of the parameters of the design point that was chosen as the base case for this project. The plasma radius of 60 cm was selected to achieve good confinement (see Section 4). A lower value of the plasma radius would result in poor confinement, although low B_{max} and

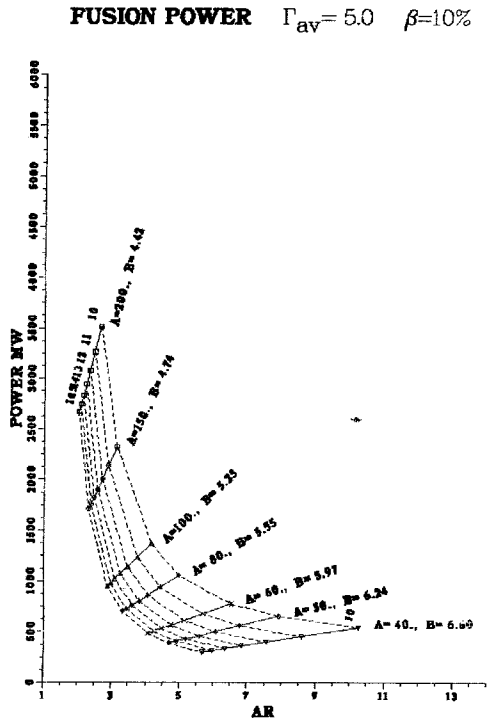

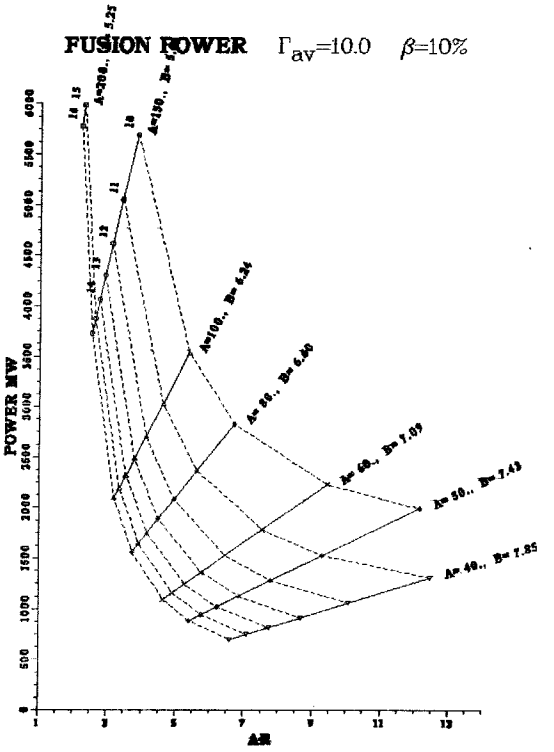

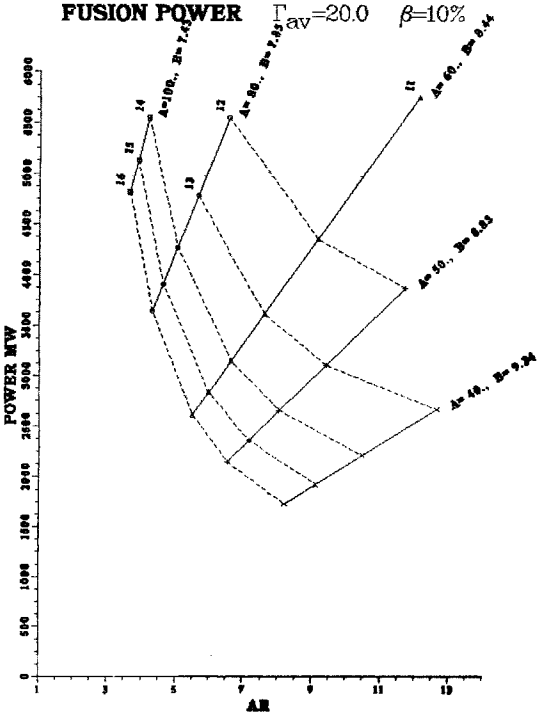

Fig. 2-3. Effect of Γ_{av} (β = 10%).

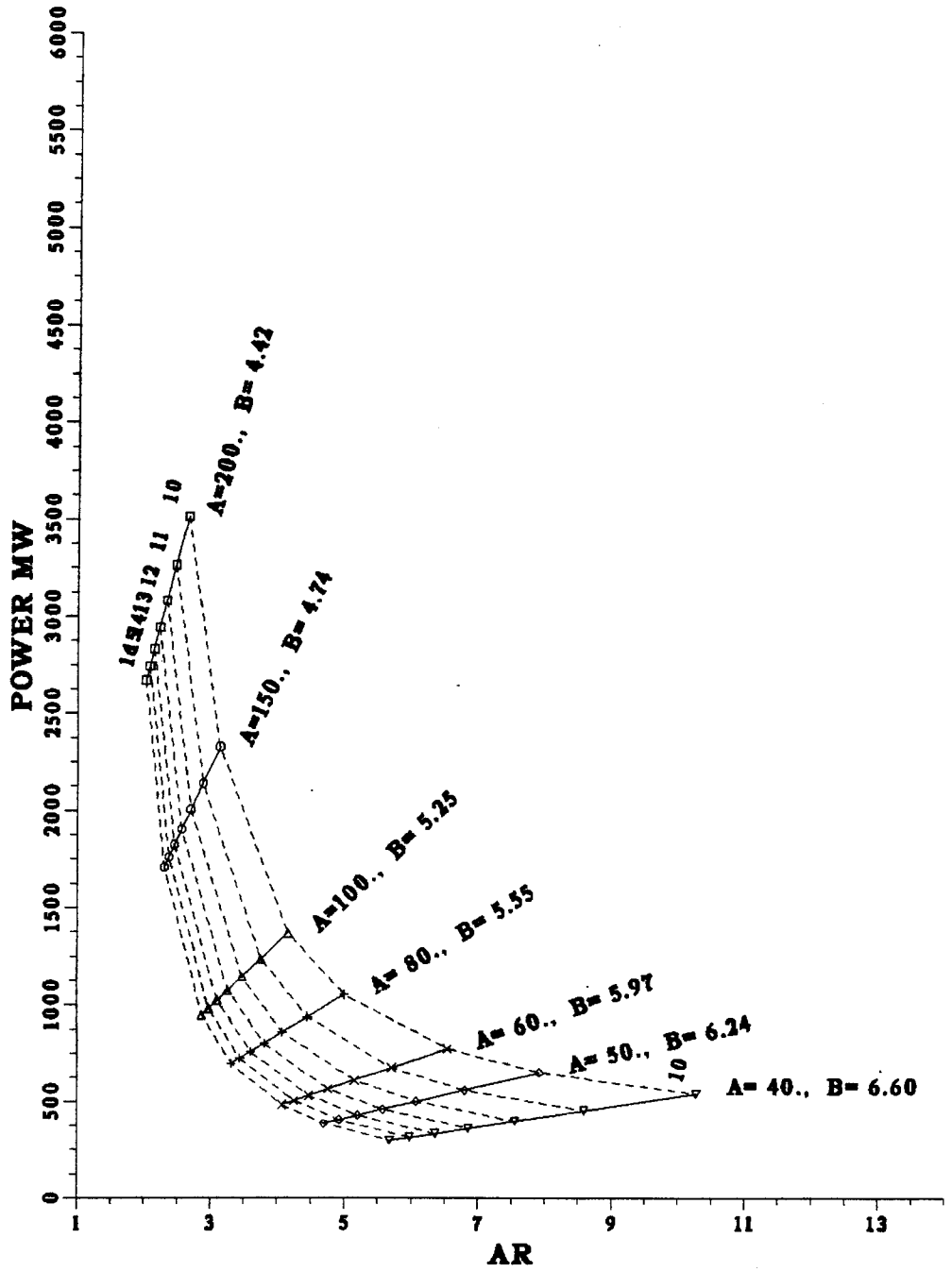

Fig. 2-3a. Case for Γ_{av} = 5 MW/m^2, β = 10%.

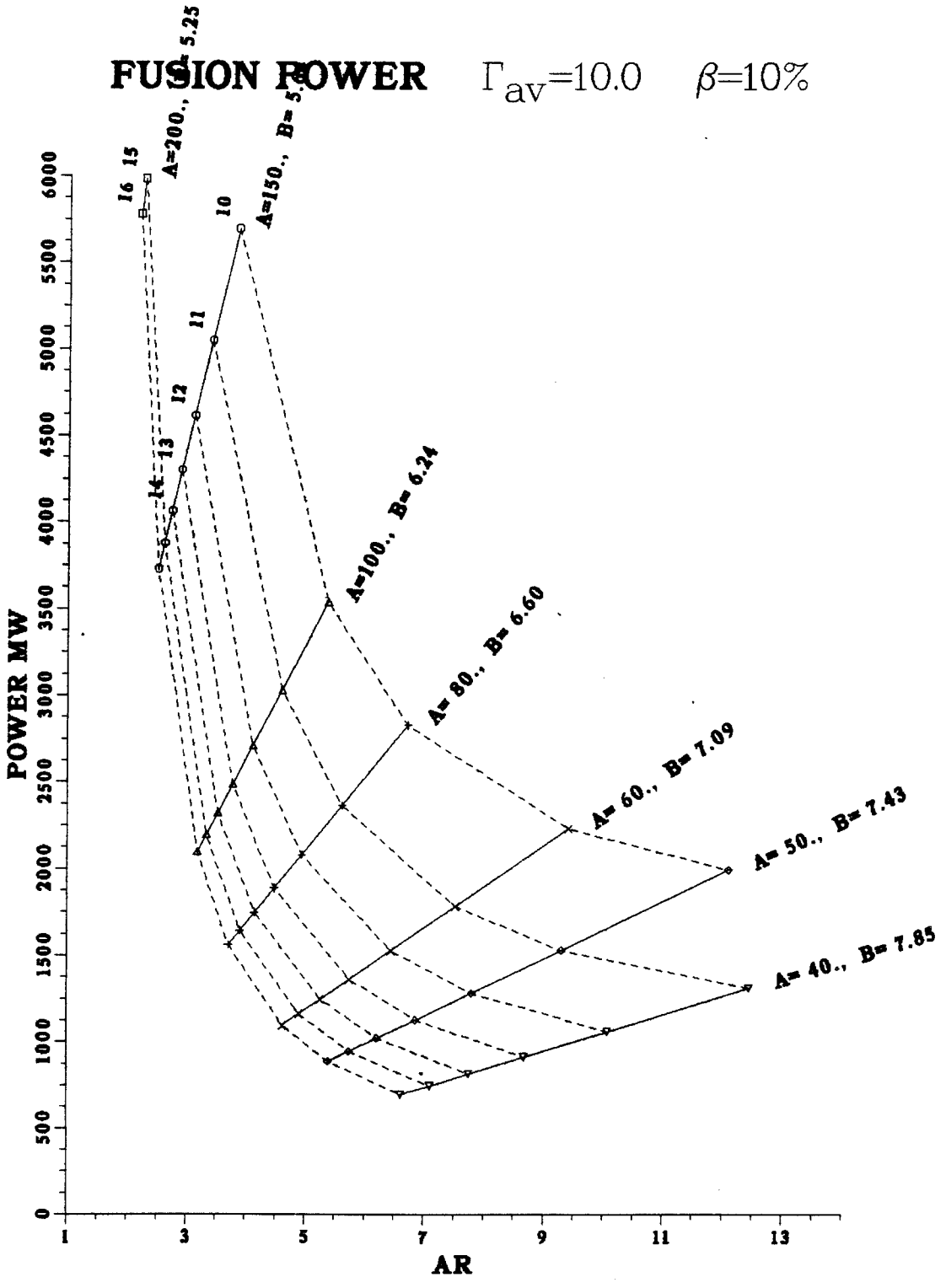

Fig. 2-3b. Case for Γ_{av} = 10 MW/m^2, β = 10%.

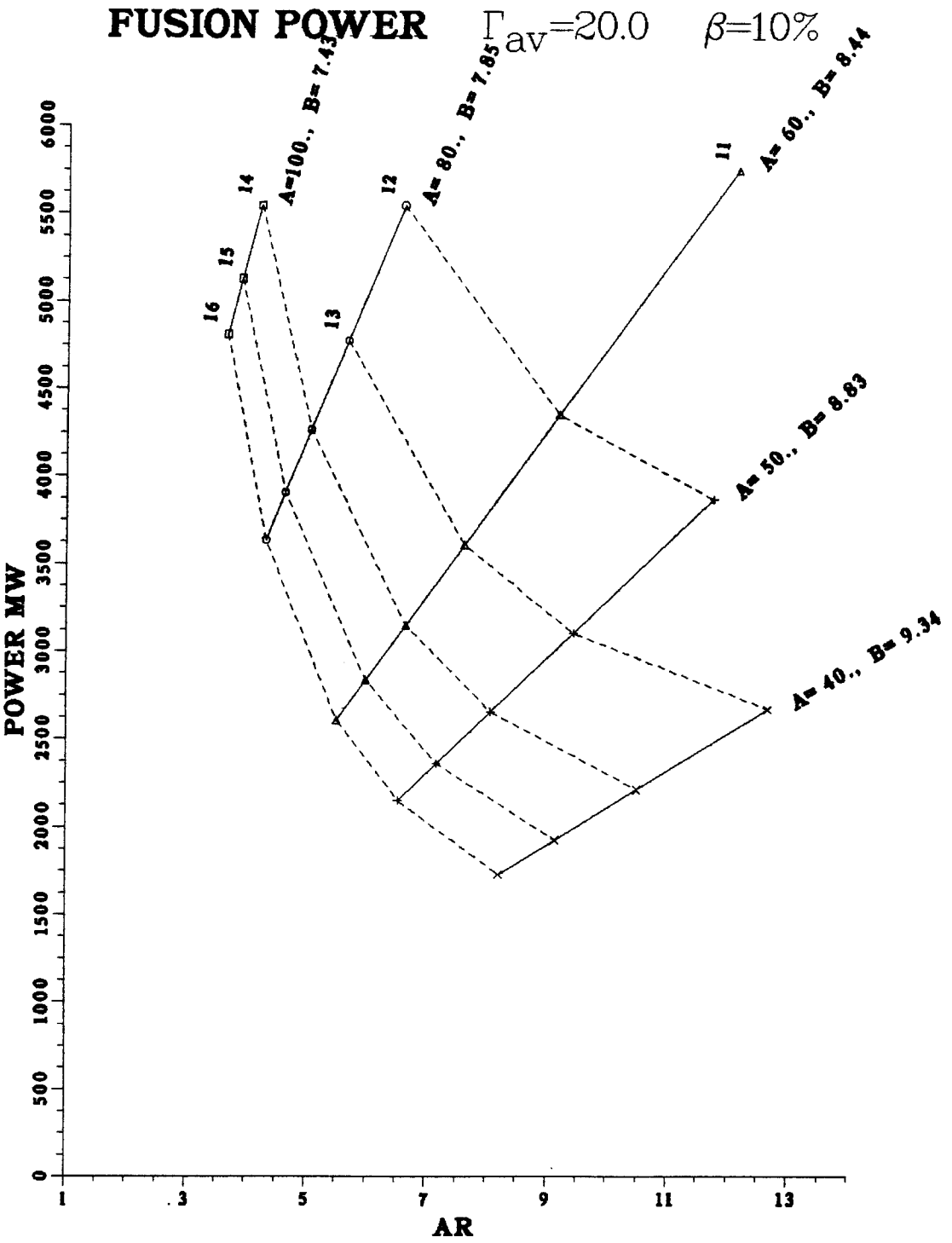

Fig. 2-3c. Case for Γ_{av} = 20 MW/m^2, β = 10%.

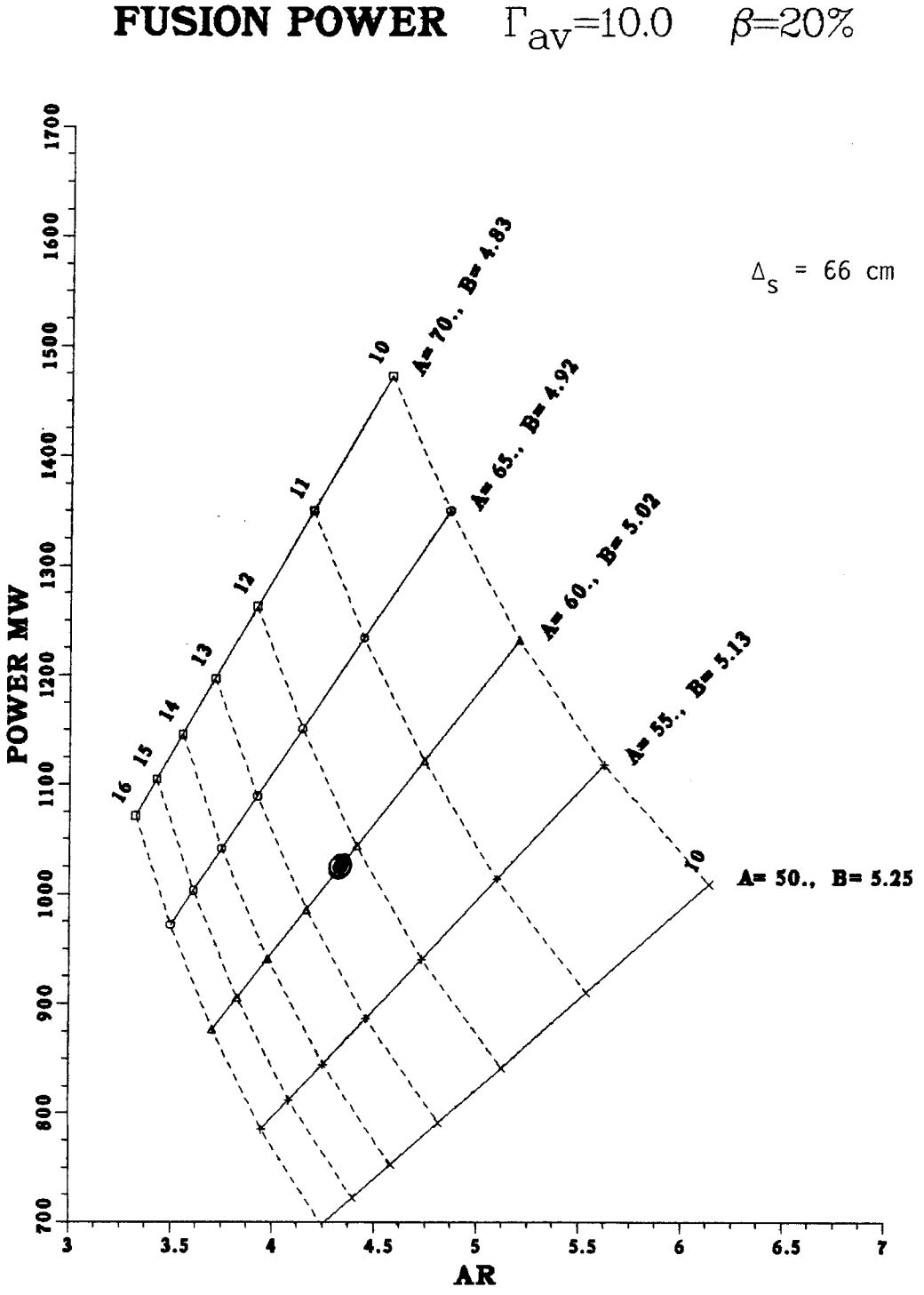

Fig. 2-4a. Case for Δ_s = 66 cm (base case), (Γ_{av} = 10 MW/m^2, β = 20%).

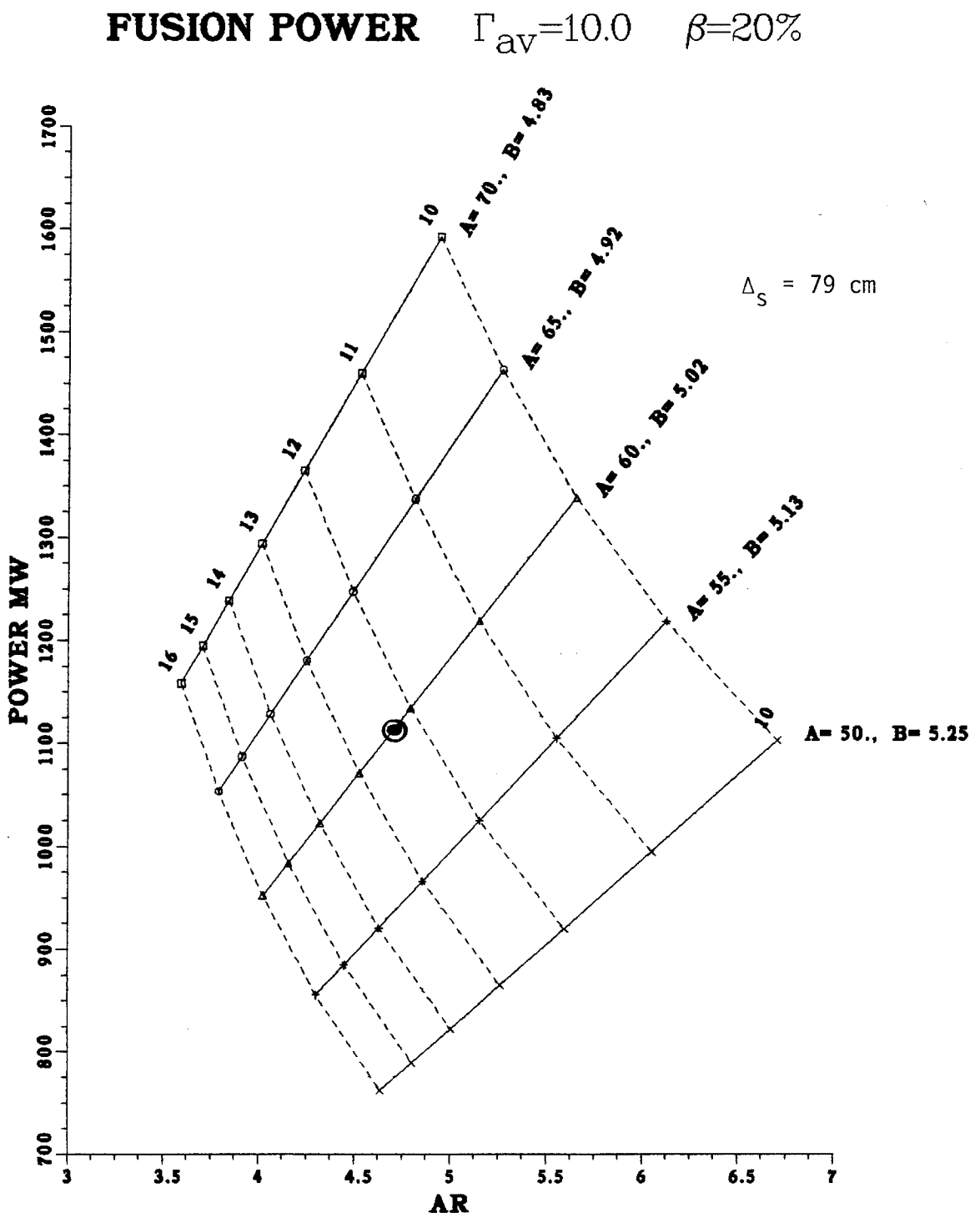

Fig. 2-4b. Case for Δ_s = 79 cm (Γ_{av} = 10 MW/m^2, β = 20%).

Table 2-4. Reactor Parameters (Base Case)

Plasma Radius (cm)	60.
Major Radius (cm)	260.
Inboard Shield Thickness (cm)	66.
B_{max} (T)	12.29
B_o (T)	5.02
Fusion Power (MW)	1025.
Inboard Peak Neutron Load (MW/m^2)	9.3
Max. Neutron Load (MW/m^2)	11.76
System Power Density (MW/m^3)	2.15
β	0.20
β_p	3.3
n_i (m^{-3})	4.2×10^{20}
n_e (m^{-3})	4.5×10^{20}
τ_e (s)	0.395

small power could be achieved. On the other hand, a higher value of the plasma radius would improve the confinement, but the fusion power and/or B_{max} would be outside the design boundaries. The value of β was chosen according to the scenario discussed in the next section. The average neutron current on the plasma surface is 10 MW/m^2. It turned out that the peak value of inboard neutron wall loading was 9.3 MW/m^2.

The system power density for this design turned out to be 2.15 MW/m^3, i.e. about 7.2 times that of STARFIRE (see Table 2-1).

References for Chapter 2

1. R. Lowell Reid and Don Steiner, "Parametric Studies for the Fusion Engineering Device," Nuclear Technology/Fusion 4, 120 (1983).

2. C.C. Baker et al., "STARFIRE - A Commercial Tokamak Fusion Power Plant Study," ANL/FPP-80-1 (1980).

3. R.A. Krakowski et al., "The Technology of Compact Fusion Reactor Concepts," Nuclear Technology/Fusion 4, 343 (1983).

4. J.C. Hosea, "Radio Frequency Heating and Current Drive Experiments on the Princeton Large Torus," Trans. Am. Nucl. Soc. 46, 184 (1984).

5. M. Porkolab, "Fusion," Vol. 1, Part B, p. 151, Ed. E. Teller (1981).

6. P. Rutherford, at INTOR meeting in Atlanta, GA (May, 1984).

3. MHD EQUILIBRIUM

3.1 Introduction

This chapter discusses issues related to poloidal field coil design for a high beta tokamak. The original tasks were to investigate "the required poloidal magnetic field magnet set and its suitability for a reactor where adequate space is needed for the blanket and shield between the plasma and the magnets. In addition, it is highly desirable to avoid poloidal magnets which interlock the toroidal magnet set." To this end, it was required that "We utilize MHD equilibrium and stability codes existing in the fusion community to evaluate magnetic field configurations, and we will do some refinement of magnet designs." It was clearly stated, because of the level of effort, "We will not do MHD equilibrium and stability theory per se."

Two early realizations from equilibrium calculations led to a modification of the planned approach: (1) For a high beta scenario in which a bean-shaped plasma plays a role, a "bean" coil which interlocks the toroidal field coils is necessary, and (2) when taking advantage of high beta by decreasing major and minor plasma radii, it becomes much more difficult to find reasonable equilibrium field coil sets than it is at large radii -- even for a D-shaped plasma. The first consideration implies that the bean coil must be normal conducting. The second realization led to the decision to concentrate the manpower on MHD equilibrium, which is the more fundamental problem, rather than on MHD stability. The rapidly developing, but early, state of MHD stability theory for bean shaped tokamaks also prompted this decision.

Since the thrust of this study was to investigate a high beta, moderate power level reactor (on the order of 1000 MW fusion), a low operating power for the bean coil was a high priority. Early calculations showed this to be

impossible in steady state, so the following scenario was proposed:

1. Begin with a low beta, D-shaped plasma.
2. Raise the indentation and the beta to reach a moderate beta, bean-shaped plasma.
3. Raise the beta to get into the second stability regime for a D-shaped plasma, while maintaining a bean shape.
4. Relax the indentation to zero and run steady state as a high beta plasma in the second stability regime.

Indentation is defined as d/2a, with d and a defined in Fig. 3-1.[1] The figure also shows other notation which has become standard. Figure 3-2[2] shows, qualitatively, the rationale for choosing this scenario: In order to reach the second stability regime, it appears necessary to indent the plasma to a value of ~ 0.2-0.3. However, once the second stability regime has been reached, the indentation may be relaxed while remaining at high beta with a stable plasma. Relevant calculations and further considerations will be discussed in Section 3.2.

Good progress on important aspects of this scenario has been made. However, further work and unanswered questions remain, as elaborated upon in Section 3.2.

3.2 MHD Equilibrium Calculations

The MHD equilibrium calculations detailed in this section were the prime focus of this contract in the area of MHD issues. The main reason for the lower priority assigned to MHD stability calculations was that: (1) Equilibrium is the more basic problem -- without it, stability questions are meaningless, and (2) reasonable equilibrium field coil sets were very difficult to find at small major and minor radii. In fact, in some aspects of the

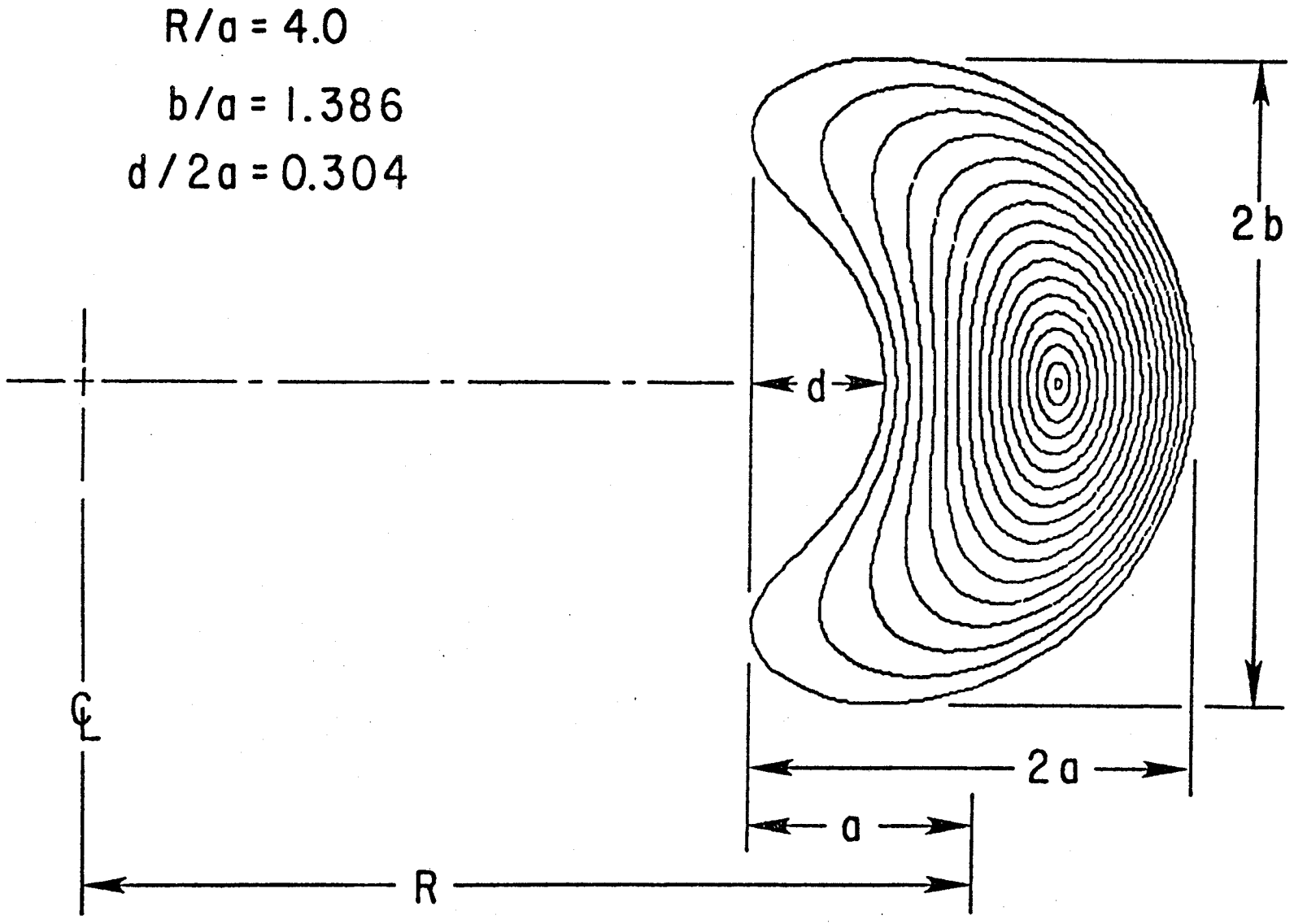

Fig. 3-1. Standard notation for bean-shaped plasmas.

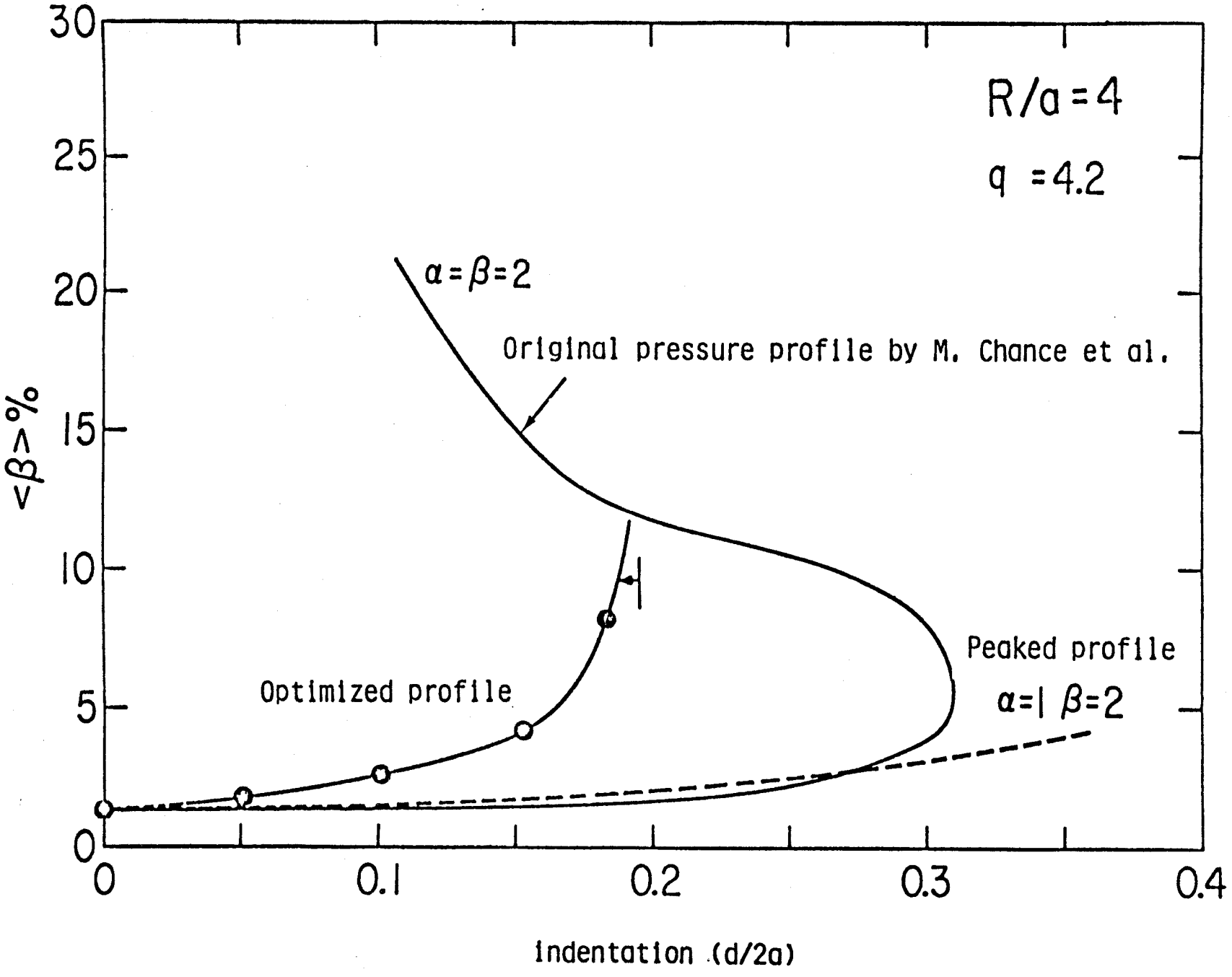

Fig. 3-2. Average β vs. indentation.

scenarios sketched in Section 3.1, satisfactory coil sets were not achieved. This difficulty at small radius has not been previously documented and is a major stumbling block in the way of effectively utilizing high beta regimes.

Because high beta cases satisfying all of the design criteria were not found, the cases are all based upon the coil locations shown in Fig. 3-3. This coil set, with bean coils plus a set of 34 coils external to, but following the contour of the TF coils, allowed convergence of the computer code in a maximum of cases. With a smaller subset of these coils, especially at high beta, the code would converge only within a very limited range of parameters. Clearly, this coil set would be unwieldy to build, but it suffices to illustrate the problems which arise in trying to reach high-beta -- even with an almost optimum coil set in terms of shaping the field.

The chief tool used in this analysis was the FEDC MHD equilibrium code,[3] which had been used successfully to design a conceptual coil set for TFCX. The code was slightly modified to allow the plasma boundary to be specified by a standard "bean" formula.[4] This allows contact between the results of the code and most of the published MHD stability theory for bean shaped tokamak plasmas. The code was normally run by specifying the plasma boundary, plasma current, toroidal magnetic field, and location of the poloidal field coils; the coil currents were then returned as output. An advantage of this code over some of the other available codes is that the functions of defining magnetic fields and of defining the coils needed to generate those fields were integrated into a single code. A variety of options exist within the code for shaping plasma pressure and current profiles.

As discussed in the introduction, the scenario envisioned was to continuously vary the plasma shape and beta from a low beta D-shape to a high beta D-

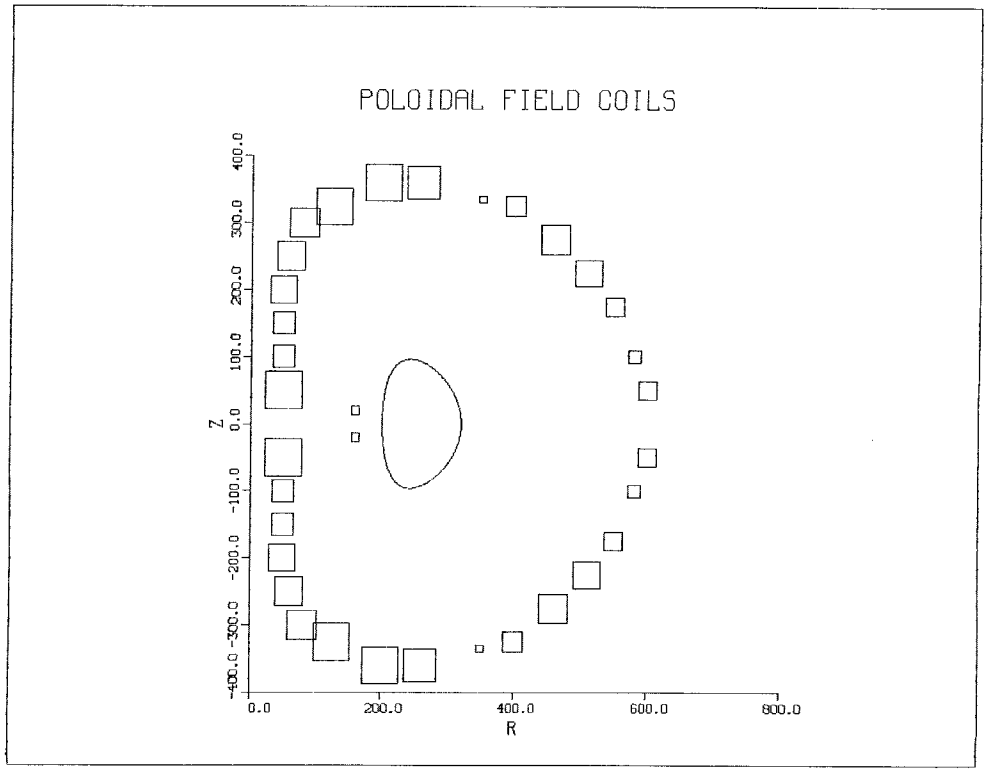

Fig. 3-3. One possible poloidal field coil set for the low-beta, D-shaped regime.

shape, with a high beta bean shape as an intermediate stage. The high beta D-shaped plasma, in the second stability regime, would be the steady-state operating mode. The possibility of operating steady-state as a highly indented bean shape was considered. This was rejected because the high current required in the bean coil led to large recirculating power fractions and the large size of the bean coil caused a variety of engineering difficulties. Four phases of the operating scenario and related calculations will be highlighted in turn.

3.2.1 Low Beta, D-shaped Plasma

The regime of low beta D-shaped plasmas has, of course, received much attention. The region of interest here, however, is somewhat different than in most other work since a tokamak reactor of small size and low beta would not be economically feasible. Although cases with reasonable currents were found, the currents were considerably larger than comparable cases with larger radii. Of course, the total mass of the coils with reduced radii may actually be smaller, but the large currents and cross sections can still create difficult engineering problems.

An interesting discovery was that it may be worthwhile to partially energize the bean coil. Since this coil is much closer to the plasma than the other PF coils, which must remain outside the TF coils, it is very efficient in helping to shape the D. For a typical case of 0.8 MA in the bean coil, only 3 MW of electrical power are required. Figure 3-3 shows the result of energizing the bean coil.

3.2.2 Moderate Beta, Bean Shaped Plasma

A case with moderate beta, ~ 6.6%, and indentation, ~ 0.05, is shown in Fig. 3-4. Plasma pressure and current profiles are shown in Fig. 3-5a, while

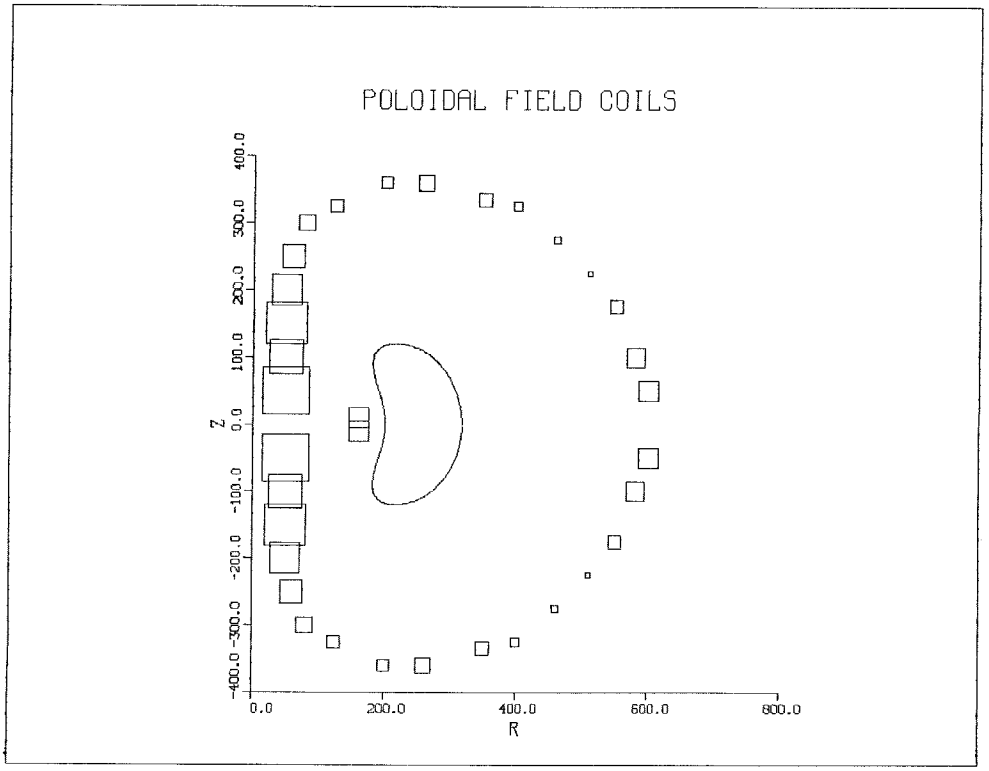

Fig. 3-4. A poloidal field coil set for a case with moderate beta and small indentation.

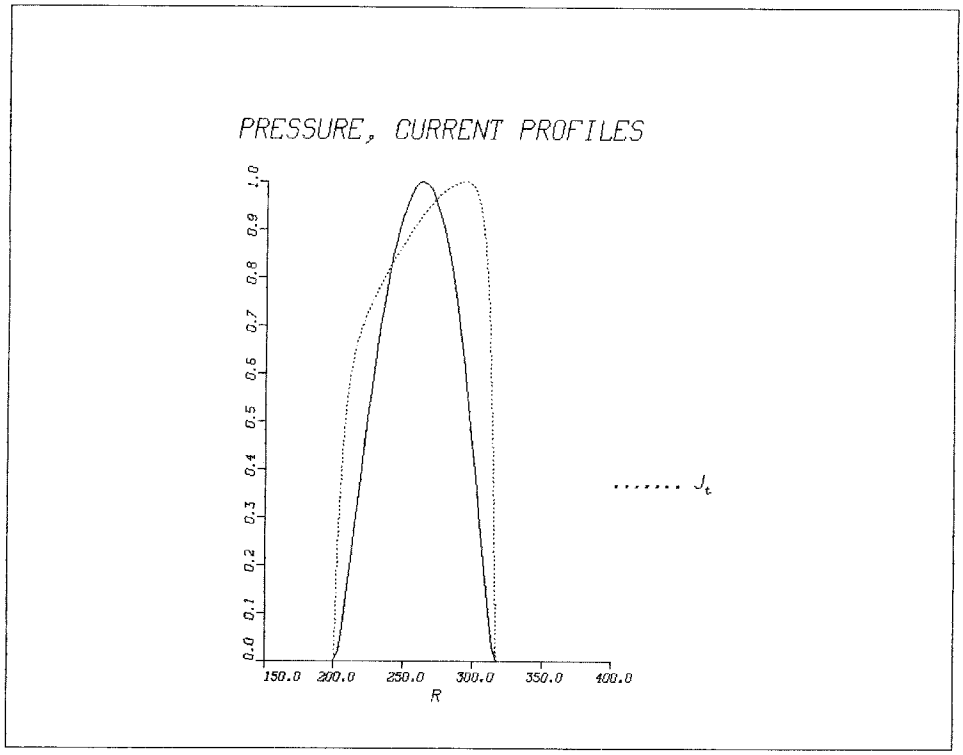

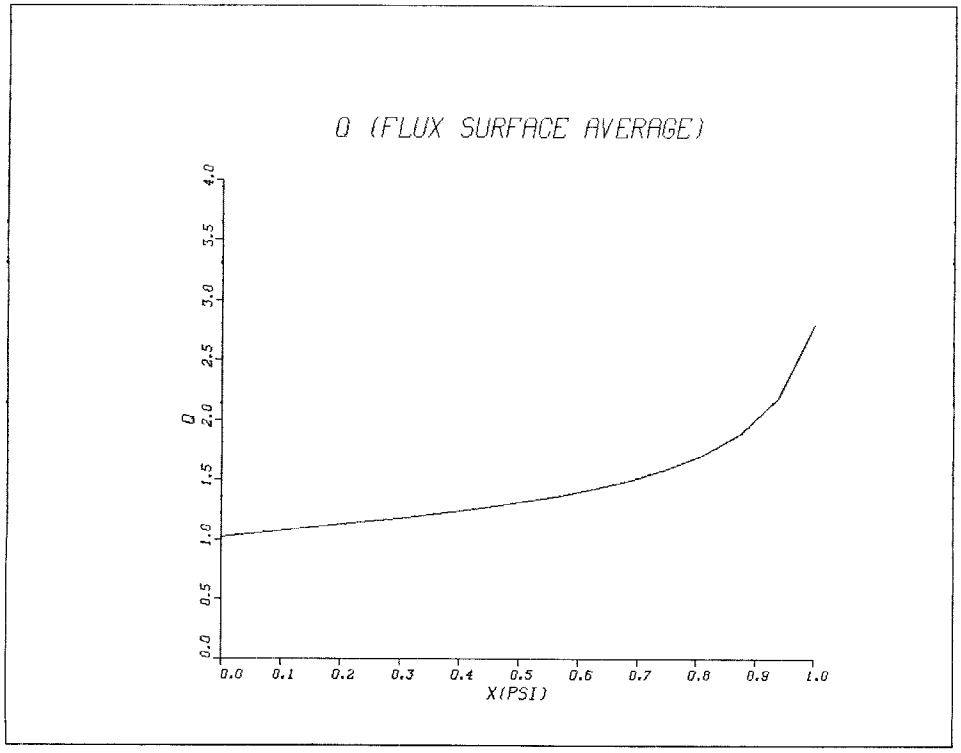

Fig. 3-5. (a) Pressure and current vs. major radius.
(b) Flux surface averaged Q vs. ψ.

Fig. 3-5b gives the flux surface averaged q profile. Although equilibria in this regime were relatively easy to find, shaping the q profile and plasma contour as desired was much more difficult than in the previous case.

3.2.3 High Beta, Bean Shaped Plasma

The difficulties inherent in shaping a small major and minor radius plasma with coils located outside of the TF coils become severe in this regime. At 20% beta, the plasma surface contour reached indentations of ~ 0.15, but no cases were found which satisfied the goal of d/2a = 0.3 without strongly distorting the flux surfaces from the standard formula. The q profiles for these cases also differed considerably from the range q(axis) = 1 to q(surface) ~ 4 which was the goal for MHD stability reasons. Furthermore, at 20% beta, q(axis) is too small by about a factor of 1.6. Thus, although some of these cases may be adequate for the purpose of reaching the second stability regime for a D-shape, making contact with established MHD stability theory for bean shapes was not possible.

For comparison, a proposed case for the PBX experiment is shown in Fig. 3-6.[5] This case had 10% beta and d/2a = 0.26. Note that while the plasma size is similar to that of interest here, the bean coil is only about 10 cm from the indentation and the other PF coils are also quite close to the plasma.

A major constraint is the requirement for adequate neutron shielding of the bean coil. For the small radii involved, it appears critical to get the coils doing the shaping close to the plasma. Adequate shielding and scrape-off layer thickness led to placing the bean coil some 40 cm from the inner edge of the plasma. This may simply be inadequate when trying to reach a plasma minor radius of 60 cm. Some cases were run to see whether placing

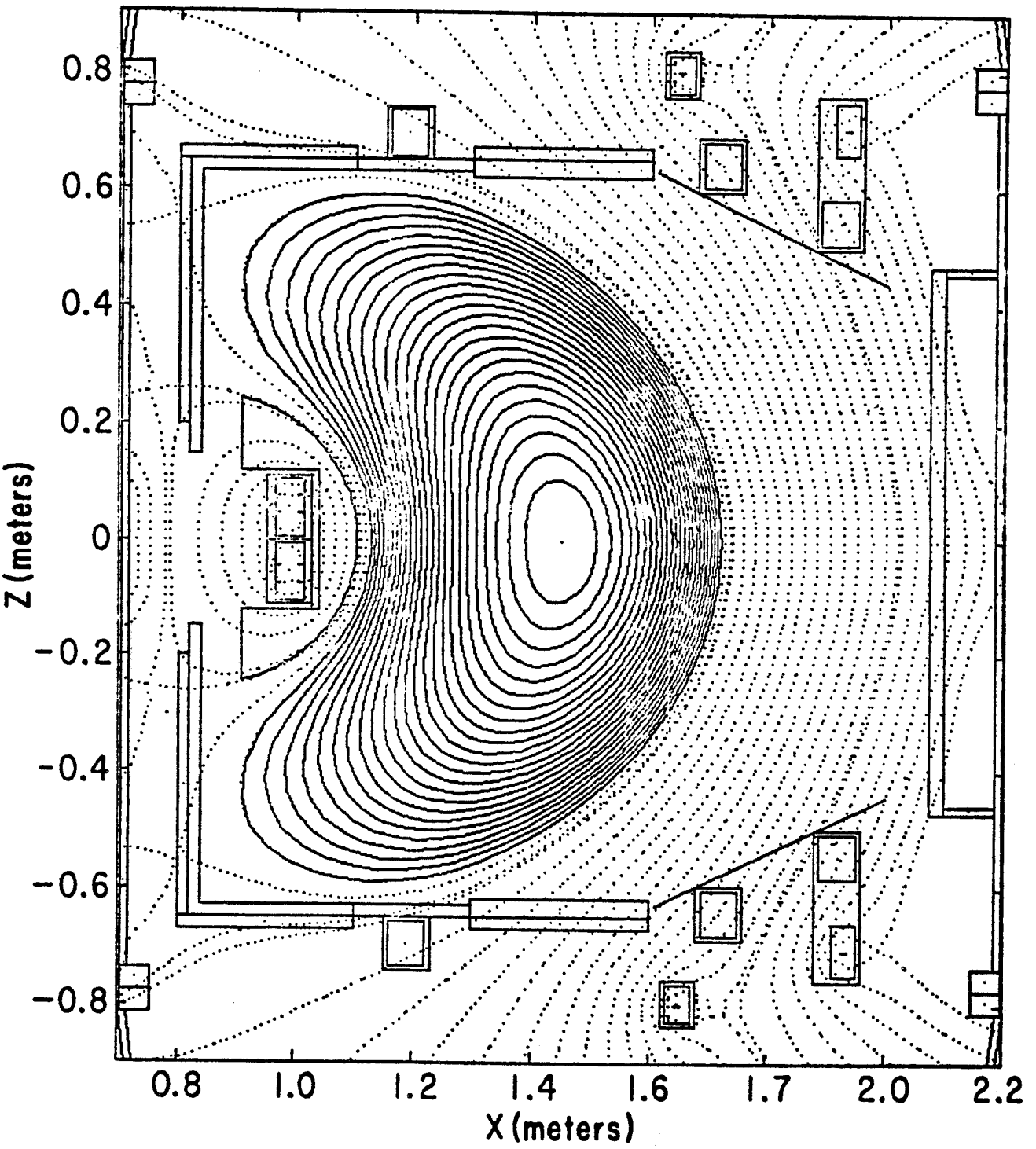

Fig. 3-6. Flux surfaces and poloidal field coil set for PBX.

coils (which would necessarily be normal conducting) interlocking the TF coils and inside the shielding would help form the bean shape. The added constraint is then that the total power needed for these coils is small. Unfortunately, little success was attained.

3.2.4 High Beta, D-shaped Plasma

Even for a D-shaped plasma, small radii cause a multitude of problems. In fact, cases with the design goals of 20% beta or with q(axis) = 1 and q(surface) ~ 4 could be found, but no cases which simultaneously satisfied these criteria were identified. In general, increasing the plasma current increased the allowed beta value, but decreased q(axis). The only non-geometric parameter available to change q(axis) is then the toroidal magnetic field magnitude. However, this value has already been pushed close to the limits allowed in the present state of the art in superconducting coil design.

3.3 Conclusions

The most important result of this work is that a very serious potential problem for small radius, high beta plasmas has been identified. The difficulty in achieving acceptable coil sets in this regime implies that the most obvious mode of taking advantage of high beta in a tokamak may not be available. It is therefore strongly advised that further work on the problem be initiated immediately. In particular, other MHD equilibrium computer codes and techniques should be used to investigate this regime.

Acceptable, moderate beta cases were found, and these could lead to a useful, small tokamak reactor. However, to achieve the required fusion power densities would then require a substantial increase in the toroidal magnetic field, far beyond what we thought credible in this study.

References for Chapter 3

1. M.S. Chance, S.C. Jardin, and T.H. Stix, Ph. Rev. Let. 51, 1963 (1983).

2. R.C. Grimm et al., "MHD Stability Properties of Bean-Shaped Tokamaks," Princeton Plasma Physics Laboratory Report PPPL-2090 (1984).

3. D.J. Strickler, J.B. Miller, K.E. Rothe, and Y-K.M. Peng, "Equilibrium Modeling of the TFCX Poloidal Field Coil System," Fusion Engineering Design Center Report ORNL/FEDC-83/10 (1984).

4. J. Manickam, R.C. Grimm, and M. Okabayashi, Phys. Rev. Let. 51, 1959 (1983).

5. K. Bol et al., "PBX: The Princeton Beta Experiment," Princeton Plasma Physics Laboratory Report PPPL-2032 (1983).

4. PLASMA CONFINEMENT SCALING

In the previous section, MHD equilibrium and beta optimization studies were described. These parametric studies and associated MHD equilibrium calculations were used to determine a "design point" for this scoping study. Our target was a fusion power of about 1000 MW with a high wall loading ($\simeq$ 10 MW/m^2) and a volume averaged beta of about 20%. The parametric studies were useful in choosing a design point near this target with reasonable values for the magnetic field, plasma major and minor radii, and other basic parameters. The systems code checks to see if the plasma energy confinement is adequate by calculating the ignition margin assuming "INTOR" scaling.

INTOR scaling is somewhat dated and does not adequately describe recent experimental results. A variety of newer alternative scaling "laws" have emerged in recent years in an attempt to better fit present results. In this section we consider the influence of these more recent scaling laws on the ignition margin for our design point and other possible design points in the neighborhood of the chosen point. This is done by calculating the plasma size, and therefore the fusion power, required to achieve a given ignition margin. In this calculation, beta is fixed at 20% and the mean plasma temperature is taken to be 13 keV, which corresponds to the maximum fusion power density for a given beta. The plasma is assumed to be vertically elongated with an ellipticity, K, of 1.6. The presence of any "beaniness" required to achieve the high beta is ignored, since the scaling laws are based on experimental data obtained from plasmas with the usual circular or D-shape, not bean-shaped plasmas.

We consider a low aspect ratio, low q (A = 4.3, q = 2) case, which is the design point chosen, and a higher aspect ratio and Q case (A = 7, q = 4).

This latter case would correspond to a higher fusion power (1500 MW) at the same plasma minor radius (60 cm), but may ease considerably the demands on the poloidal field magnet set required for MHD equilibrium.

The definition of the ignition parameter, M, used in this study is the ratio of the alpha heating power to the power lost by transport across the magnetic field. Thus

$$M = \frac{\frac{n^2}{4} \langle \sigma v \rangle_f Q_\alpha V}{3 \frac{n^2 kT}{n\tau_E} V} \simeq \frac{n\tau_E}{\frac{12\ kT}{\langle \sigma v \rangle_f Q_\alpha}} . \qquad (4.1)$$

Here τ_E is the global energy confinement time, n is the plasma density, T is the plasma temperature (taken equal for ions and electrons), $\langle \sigma v \rangle_f$ is the Maxwellian-averaged fusion reaction rate, Q_α is the energy deposited in the plasma per fusion event, and V is the plasma volume. We assume good alpha confinement and take Q_α = 3.5 MeV. The quantities n, T, and $\langle \sigma v \rangle_f$ are actually spatially dependent; the scaling laws which yield τ_E are based on a global energy balance with no spatial (profile) information. Consequently, we use Eq. (4.1) in a global sense and interpret n and T in Eq. (4.1) as global averages. The fusion reactivity, $\langle \sigma v \rangle_f$, is a function of T; the value of the denominator at T = 13 keV is about 2 x 10^{14} s/cm^3. Hence we take

$$M = \frac{n\tau_E\ (s/cm^3)}{2 \times 10^{14}} . \qquad (4.2)$$

With this definition of M, M = 1 is an ignited plasma in energy balance; M > 1 is super-ignited and the plasma temperature will rise. Alternately, one

can view M > 1 as providing a safety factor for energy loss through channels not treated in the scaling law considered, or a safety factor against errors in the scaling law itself.

The calculational procedure is to first select the toroidal magnetic field, B_T, at the magnetic axis. This determines the plasma density, since β and T are already fixed. Given the aspect ratio, A, and the MHD safety factor, q, we then compute the minor radius, a, to achieve a given M value. Finally, we compute the fusion power, P, implied by this minor radius. The results are presented as graphs of the fusion power versus B_T for a given M, A, and Q.

First we consider INTOR scaling,

$$\tau_E = 5 \times 10^{-19}\, na^2 \,. \tag{4.3}$$

All quantities in this section have units of cm, amp, MW, eV, or s. Then

$$n = 1.24 \times 10^{18} \frac{\beta B_T^2}{T}$$

$$a = 2 \times 10^{16} \sqrt{\frac{M}{n}}$$

and

$$P_f = \frac{\pi^2}{2} a^3 A K n^2 \langle \sigma v \rangle_f Q_f \,.$$

The results are shown in Fig. 4-1 for M = 0.3, 1, and 3 for both the low and high aspect ratio cases. According to INTOR scaling, our design point (B = 5 T, A = 4.3, q = 2) ignites at about 600 MW and has an ignition margin of about

Fig. 4-1

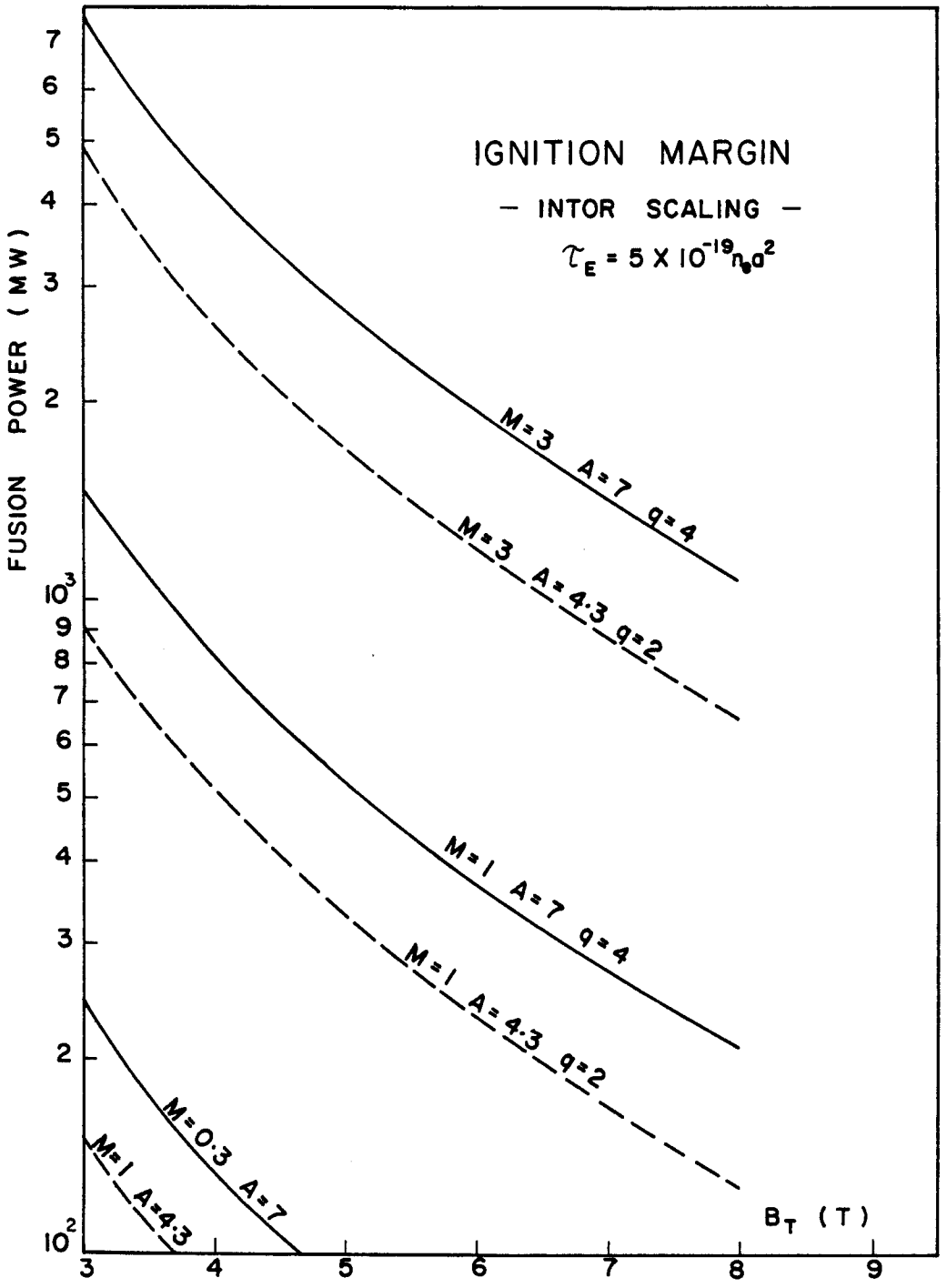
IGNITION MARGIN
— INTOR SCALING —
$\tau_E = 5 \times 10^{-19} n_e a^2$
FUSION POWER (MW)
10^3
10^2
M=3 A=7 q=4
M=3 A=4.3 q=2
M=1 A=7 q=4
M=1 A=4.3 q=2
M=0.3 A=7
M=1 A=4.3
B_T (T)
3
4
5
6
7
8
9

2 at the design power level. The higher aspect ratio case (A = 7, q = 4) has a design power level of 1500 MW and is ignited with the same margin.

Second, we consider "ohmic" scaling,

$$\tau_E = 7.1 \times 10^{-22}\ naR^2\ \sqrt{q} \tag{4.4}$$

which is similar to neo-Alcator scaling. This scaling fits the ohmic heating phase of a broad range of devices from small size up to TFTR and JET, as far as the density and basic size scaling is concerned. The separate a and R scaling has also been tested in TFTR by varying a and R separately. The ignition margin obtained with this scaling is shown in Fig. 4-2. This scaling is very favorable, and even rather small plasmas will ignite. Figure 4-2 shows the curious result that there is no improvement in M with increasing magnetic field for a given fusion power.

Next, we consider Mirnov scaling,

$$\tau_E = 0.39 \times 10^{-8}\ I_{pa} \tag{4.5}$$

where I_p is the plasma current in amps. This scaling is sometimes used in the TFCX studies. The ignition margin for this scaling is shown in Fig. 4-3. This scaling favors lower aspect ratio and q, in comparison to the previous scalings. In this case, the 1000 MW design point (A = 4.3) has a reasonable margin (~ 2.5), but the 1500 MW case (A = 7, q = 4) does not ignite.

Confinement studies of tokamaks with strong neutral beam heating have shown more pessimistic results for τ_E. There are two modes of operation, the L-mode (meaning low confinement) and the H-mode (for high confinement). We

Fig. 4-2

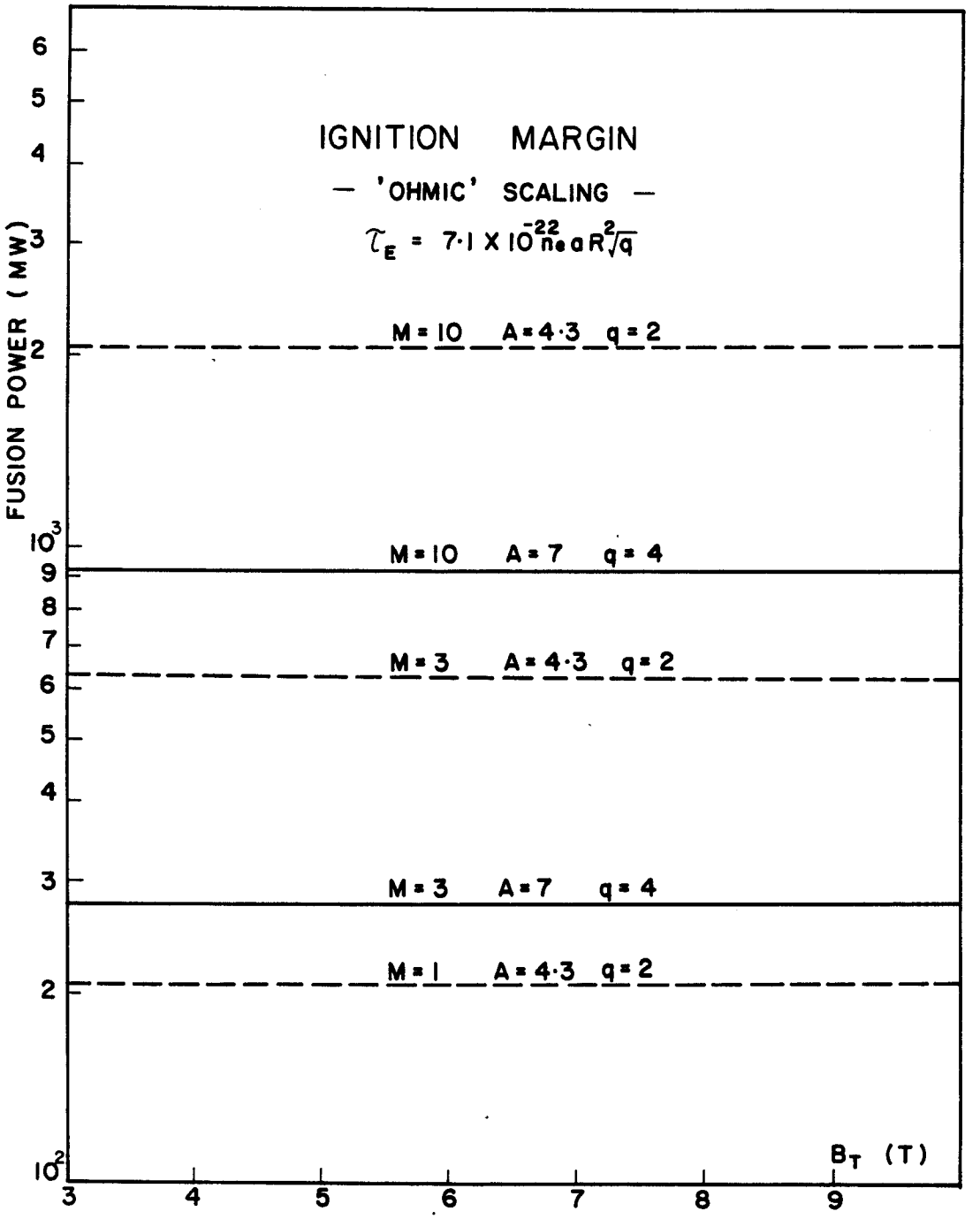
IGNITION MARGIN
— 'OHMIC' SCALING —
$\tau_E = 7.1 \times 10^{-22} n_e a R^2 \sqrt{q}$
M = 10 A = 4·3 q = 2
M = 10 A = 7 q = 4
M = 3 A = 4·3 q = 2
M = 3 A = 7 q = 4
M = 1 A = 4·3 q = 2
FUSION POWER (MW)
B_T (T)
6
5
4
3
2
10^3
9
8
7
6
5
4
3
2
10^2
3
4
5
6
7
8
9

Fig. 4-3

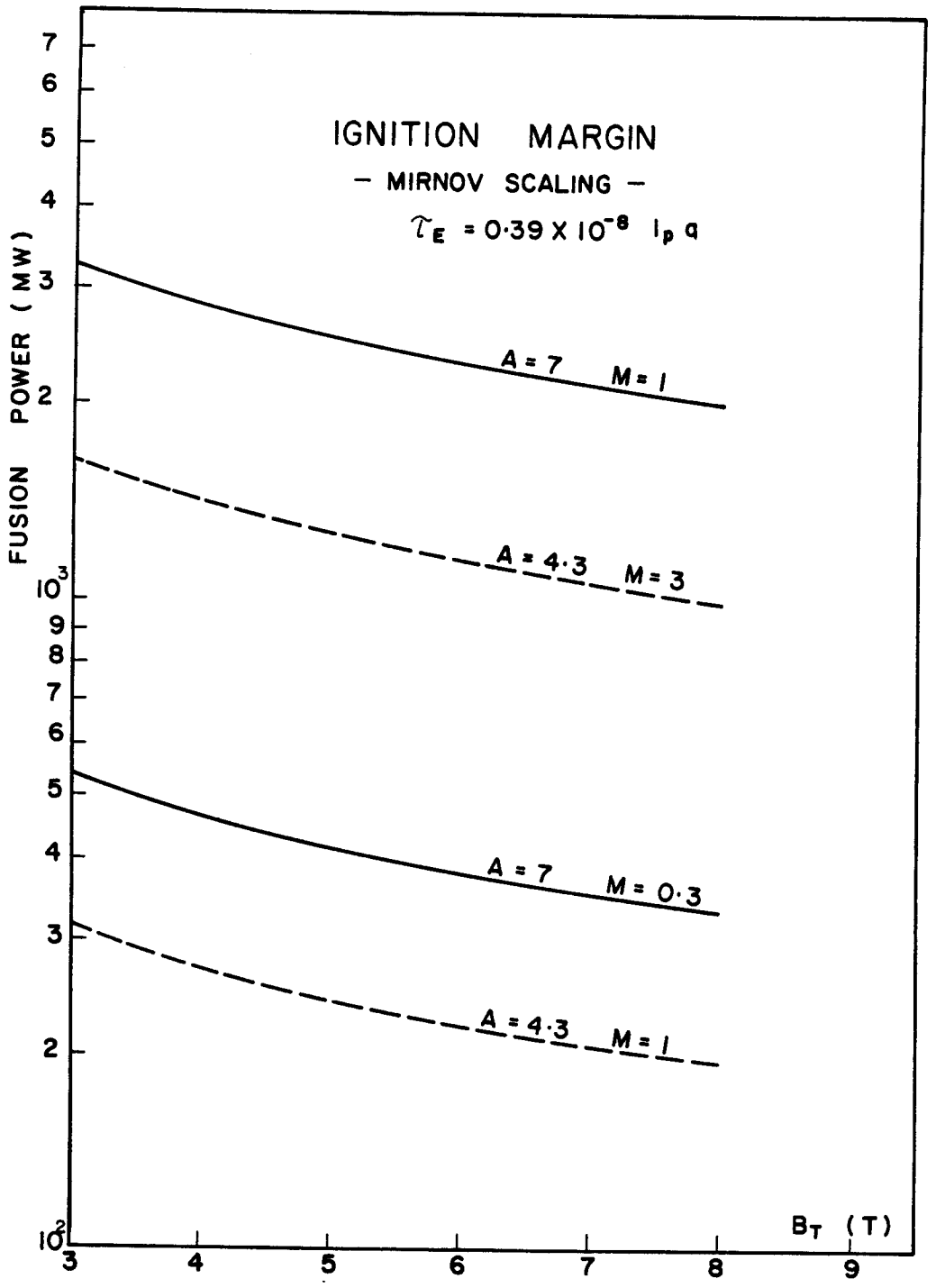
IGNITION MARGIN
– MIRNOV SCALING –
$\tau_E = 0.39 \times 10^{-8}\ I_p\ q$
A = 7 M = 1
A = 4.3 M = 3
A = 7 M = 0.3
A = 4.3 M = 1
FUSION POWER (MW)
B_T (T)
7
6
5
4
3
2
10^3
9
8
7
6
5
4
3
2
10^2
3
4
5
6
7
8
9

first consider L-mode scaling,

$$\tau_E = \frac{6.4 \times 10^{-8} \, I_p R^{1.75} \sqrt{K}}{a^{0.37} \sqrt{P_T}} \tag{4.6}$$

where P_T is the total heating power. The negative scaling with P_T, obtained from neutral beam injection experiments with $P_T \simeq$ 2-6 MW, has been seen in several devices, but with much scatter in the experimental data. How does one apply this result to alpha heating in a fusion plasma? Is it reasonable to replace P_T by the alpha heating power? If this is done, then the result is very pessimistic, and ignition is not even close.

The discovery of the H-mode in ASDEX, and its subsequent observation in other machines, has led to a more hopeful situation. In the H-mode, the confinement improves, compared with the L-mode. In most of the data, about a factor of 2 improvement is seen in the H-mode. A conservative position is to continue to use the scaling in Eq. (4.6) but with a factor of 2 improvement in the coefficient to account for the H-mode. One then eliminates P_T through the relation,

$$P_T = \frac{3n\tau}{\tau_E} (2\pi^2 R a^2 K)$$

which is equivalent to assuming that alpha heating is no different than neutral beam heating. The scaling law can now be put in a more instructive form,

$$\tau_E = \frac{1.7 \times 10^3 \, R^{2.5} a^{-2.74} I_P^2}{n\bar{T}} \, . \tag{4.7}$$

Note the negative scaling with temperature in Eq. (4.7); this result is still very pessimistic and ignition is impossible if Eq. (4.7) proves to be valid.

The impossibility of ignition with the above scaling comes from replacing P_T by the alpha heating power, P_α, and extrapolating from $P_T \simeq 2.6$ MW to $P_\alpha \simeq$ 300 MW with the $P_\alpha^{-1/2}$ dependence in Eq. (4.6). The ASDEX data does not, however, exhibit a decrease in τ_E with increasing P_T for the H-mode. There is also an indication of saturation of the drop of τ_E with P_T in high power injection experiments in D-III. This suggests that we replace Eq. (4.6) with a scaling where τ_E is independent of P_T. We retain the I_p, R, a, and K scaling in Eq. (4.6) and choose the coefficient by fitting the ASDEX data. This yields

$$\tau_E = 8.6 \times 10^{-11} \, I_p R^{1.75} a^{-0.37} \sqrt{K} \, . \qquad (4.8)$$

At constant aspect ratio, this gives

$$\tau_E \propto I_p a^{1.38}$$

which has a somewhat more favorable size scaling than Mirnov scaling. The results computed with this scaling are shown in Fig. 4-4. In this case, both design points are ignited with a substantial margin ($M \gtrsim 3$).

It is an open question as to whether alpha heating is similar to ohmic heating or to neutral beam heating. As in ohmic heating, the alpha power is transferred primarily to the electrons, is centrally peaked, and is axisymmetric. Neutral beam heating is non-axisymmetric in that the beams enter at only a few points, although it is generally assumed that the resulting fast

Fig. 4-4

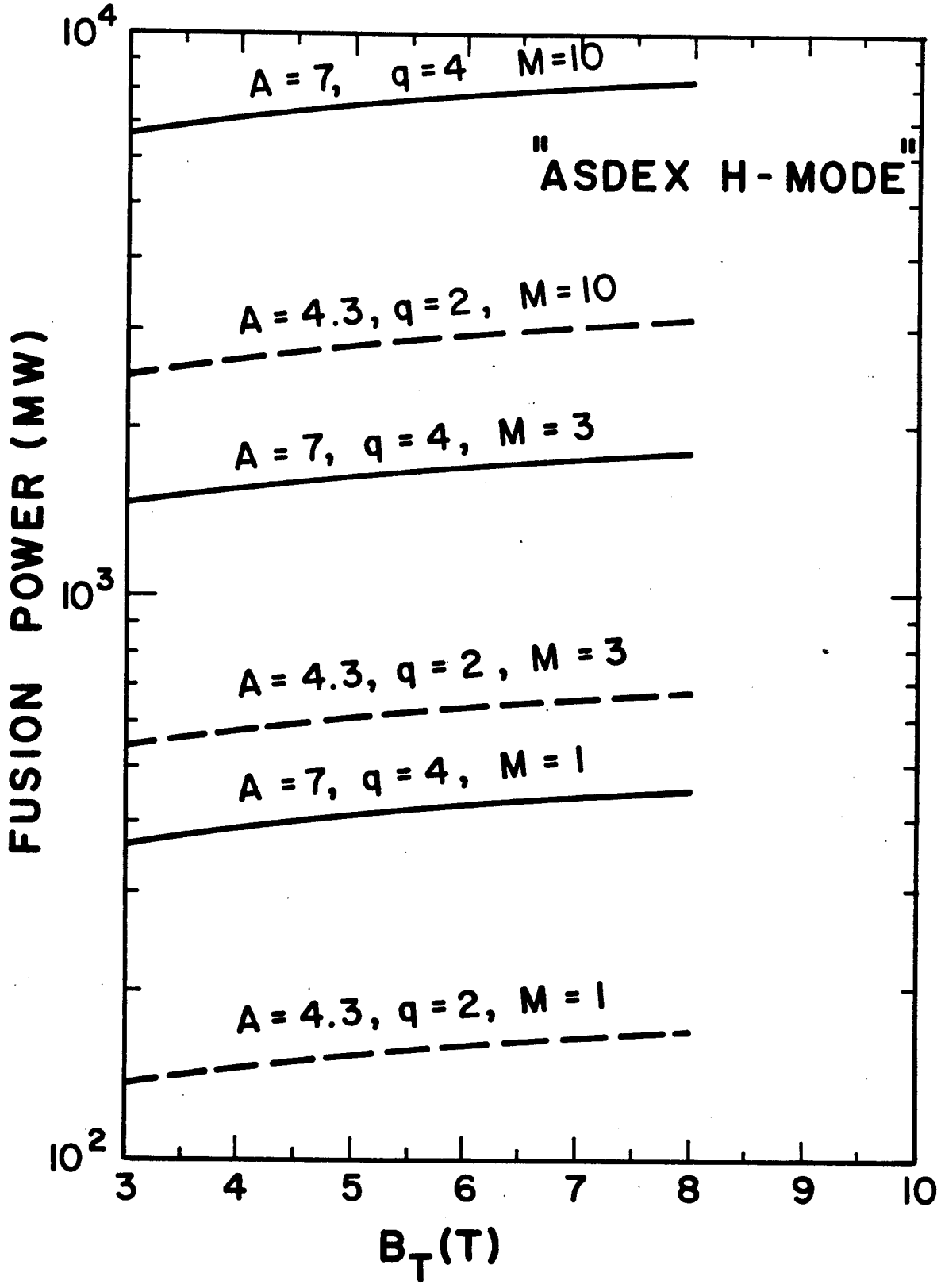
10^4
10^3
10^2
FUSION POWER (MW)
A = 7, q = 4 M = 10
"ASDEX H-MODE"
A = 4.3, q = 2, M = 10
A = 7, q = 4, M = 3
A = 4.3, q = 2, M = 3
A = 7, q = 4, M = 1
A = 4.3, q = 2, M = 1
3
4
5
6
7
8
9
10
B_T(T)

ion motion causes the energy deposition in the bulk plasma to be axisymmetric. The related neutral density, which also causes a power loss by charge exchange, is decidedly non-axisymmetric. Consequently, we cannot at this time choose on physics considerations between ohmic heating and neutral beam heating as being a better simulation of alpha heating.

From the above considerations of the various scaling laws available at this time, we see that there is a great range in the predicted ignition margin. For most of the scaling laws, an adequate ignition margin ($M > 1.5$) is obtained. On this basis the 1000 MW design point looks reasonable even though the plasma is fairly small ($a = 60$ cm). An inadequate margin, or no ignition at all, occurs for these size machines only with L-mode scaling or if only a factor of two improvement is obtained with the H-mode. The modified H-mode scaling based on ASDEX data is more favorable and leads to a good ignition margin.

5. IMPROVED BLANKET DESIGN

5.1 Introduction

Designing a blanket for a fusion power reactor is not a simple task in view of all the restrictions and requirements that must be imposed on it. The task becomes much more challenging when the blanket is for a compact high wall loading (HWL) reactor.

There are certain inalienable requirements that a blanket concept must satisfy, the most important of which are listed below:

1. The blanket must have a breeding ratio of > 1 and as high an energy multiplication as possible.
2. It must transfer the energy to a power cycle in a simple and efficient manner.
3. It should be safe and environmentally acceptable.
4. It must be reliable and maintainable.
5. It must be fabricable with modest extrapolations of present state of the art.
6. The materials should be readily available and reasonably priced.

The first requirement is essential if a fusion energy economy is to be self-sufficient. The second requirement is very important because it determines the efficiency of the power cycle and impacts the economics. The requirement that the blanket be safe and environmentally acceptable has taken on exceeding importance in recent years, with good justification. Among the important considerations are that the materials be compatible and the tritium inventory be reasonably low. The last three requirements are also very important but tend to be compromised to varying degrees.

A compact high wall loading (HWL) reactor has specific limitations which tend to exacerbate the requirements listed earlier. These limitations are:

1. Very high surface heating.
2. Very high nuclear heating.
3. Compact configuration leading to crowded components.
4. Unlikely breeding on the inboard side.
5. Frequent blanket/first wall replacement.

The result of the very high surface heating is that a separately cooled first wall is an absolute necessity. Clearly, providing a separately cooled first wall is an added complication; however, it eases the burden on the blanket design by eliminating the high surface heating on the blanket itself. In spite of this, the nuclear heating in the first several centimeters of the blanket is very high.

Setting a limit of ~ 1000 MW_{th} while utilizing high β in a tokamak fusion reactor leads to a compact configuration with a plasma radius of 0.6 m and an aspect ratio of 4.3. Furthermore, the requirement of a bean shaping coil on the inboard side needed to access the high β regimes makes it difficult to shield the TF coils. These two requirements combine to virtually eliminate the possibility of providing a breeding blanket on the inboard side. The possibility remains, however, for placing neutron multipliers on the inboard side in order to enhance breeding on the outboard side.

The high wall loading will necessarily require more frequent blanket replacement due to radiation damage. It is, therefore, essential that the blanket be designed for easy maintenance. Minimizing the mass of the blanket modules, insuring suitable configurations for removal from the reactor and allowing for good accessibility and clearances are important considerations.

In the next section we describe the blanket concept and give the reasons for its selection.

5.1.1 Concept Selection and Justification

The concept selected for the HWL blanket utilizes static $Li_{17}Pb_{83}$ contained in ferritic stainless steel HT-9 cylinders and cooled with circulating He gas. Lithium lead in various compositions has been recognized as a good breeding material in fusion reactors. Most recent designs[1-3], however, have utilized $Li_{17}Pb_{83}$ in self cooled blankets in which the material is pumped through the blanket and then to a steam generator. There are four problems with such a scheme:

1. MHD effects coming from pumping an electrically conducting fluid across magnetic field lines.
2. Corrosion of structures and corrosion product transport throughout the primary loop.
3. Tritium containment particularly in the steam generator.
4. Large, costly pipes and high LiPb inventory in the primary loop.

A separately cooled $Li_{17}Pb_{83}$ blanket gets around most of these problems. Since the breeding material is not circulated, there are no MHD losses, there are no corrosion product transport problems and the $Li_{17}Pb_{83}$ inventory is confined to the blanket. The tritium inventory in the blanket is very low, because the tritium diffuses into the helium coolant from which it is recovered by oxidation and collection on molecular sieves.

The static $Li_{17}Pb_{83}$ breeding material in the HWL blanket is contained in 15 cm OD, 14.5 cm ID cylinders oriented in the poloidal direction. The coolant tubes are immersed in the breeding material with the inlet and outlet connections made on the same end of the cylinder. Upon entering the cylinder,

the coolant tubes spiral in a helical pattern around the inner surface of the cylinder wall from one end to the other, then turn around and come back through the center, emerging through the same end as they entered.

The outstanding feature of this blanket design is its inherent safety. If a coolant tube develops a leak, the cylinder can withstand the full pressure of the coolant with ease. Another important feature of this blanket is that it can be completely drained of all breeding material prior to its removal for maintenance.

The Blanket Comparison and Selection Study (BCSS) has evaluated this concept, looking at three variations, pressurized modules (lobed submodule), pressurized canister and pressurized tubes.[4] The pressurized module design had a lobed construction and was selected for further evaluation. This design was initially given a ranking of 1, in a configuration where blankets were used both inboard and outboard. Subsequently this ranking was degraded to 1-B.[5] The critical issues identified at the time were:

- Temperature/heat flux limit on the first wall.
- Corrosion/compatibility temperature limits.
- Tritium recovery from the helium coolant.

The first issue is not relevant in the case of the HWL blanket, since the 10 MW/m^2 wall loading necessitates a separately cooled first wall.

The second issue has relevancy and has to be addressed. The BCSS set a temperature limit of 475°C[4] for a static $Li_{17}Pb_{83}$ breeder in HT-9 structure. This limit is based on a corrosion rate of 20 μm/y, a number which may be important in a small tube circulating system where plugging is of concern, but is quite arbitrary for a static system. Because of the high wall loading, the blanket will be replaced every two years, thus the structural degradation due

to thinning is inconsequential. Furthermore, experimental results of $Li_{17}Pb_{83}$ in HT-9 capsules (simulating a static system) show evidence of saturation,[6] where no weight loss is experienced after about 1000 hours at 500°C. We therefore feel that the temperature limit established is low for the blanket concept envisaged.

The final issue concerning tritium containment is perhaps the most serious one. Actually tritium recovery from the He gas is relatively straightforward. The problem is in preventing excessive tritium diffusion into the steam generator. It is significant to point out that four of the seven concepts selected by the BCSS for tokamaks have He gas as the coolant, although a sweep gas is used to remove the tritium from the breeding material. Nevertheless, a fair amount of tritium will end up in the He coolant. In the HWL reactor we recognize this problem and intend to show that tritium diffusion into the steam cycle can be maintained at acceptable limits.

In summary it can be said that the 1-B ranking given this blanket concept by the BCSS was based on somewhat different ground rules that those applicable to a HWL blanket. If the special circumstances of HWL were taken into account, the rating may well have been different.

5.2 Mechanical Design

5.2.1 First Wall

The first wall in the HWL reactor consists of a bank of tubes oriented in the toroidal direction fabricated from the ferritic stainless steel HT-9 and cooled with helium gas. Figure 5.2-1 shows several methods for fabricating continuous banks of tubes, but the preferred method is by extrusion (Fig. 5.2-1a). Such structures are presently being produced for high pressure fossile boilers and the same technology can be extended to materials such as HT-9.

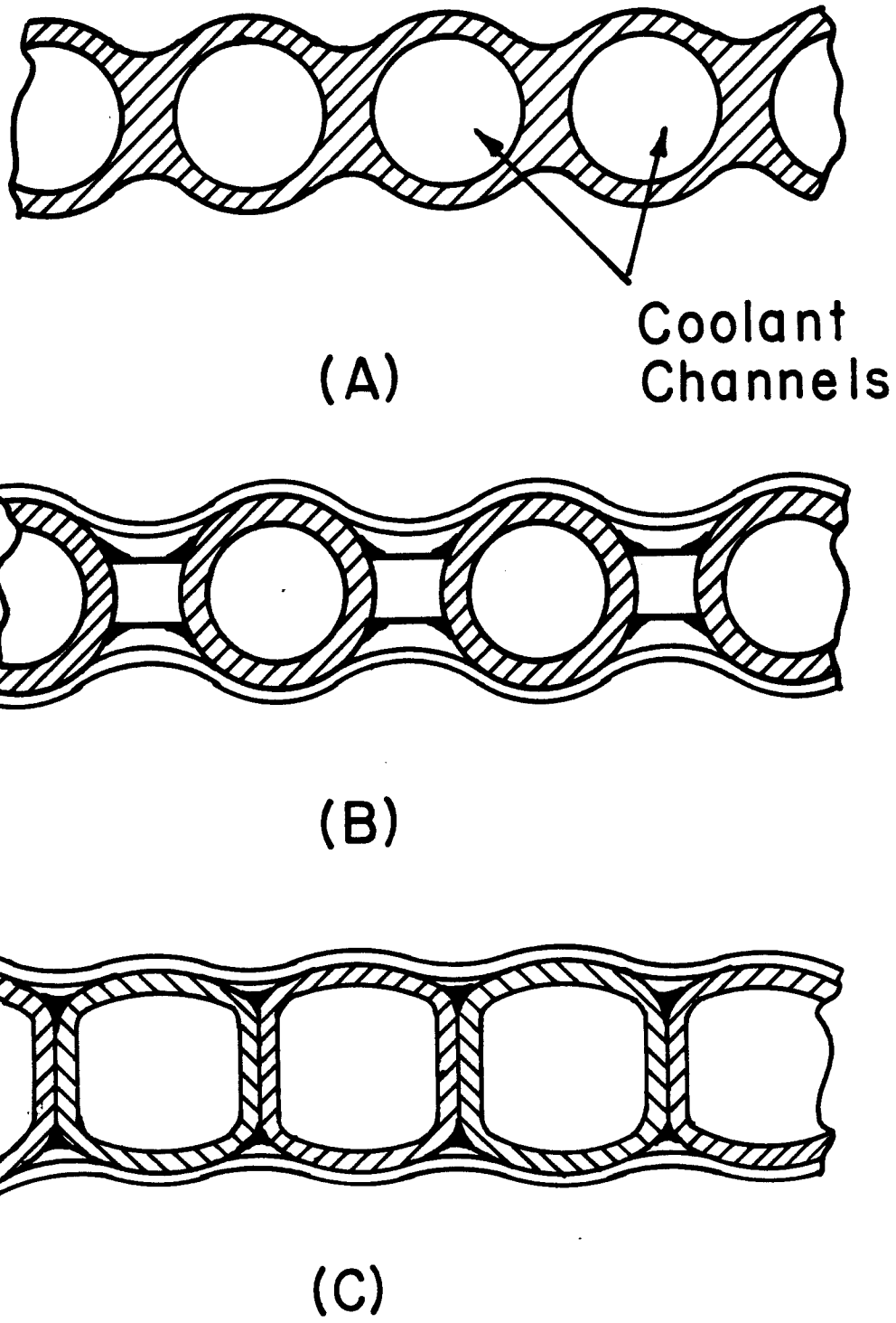

Fig. 5.2-1. Various configurations of continuous tube first walls.

The blanket and first wall in the reactor are divided into twelve equal segments, called modules, sized such that each can be extracted between TF coils without circumferential translation. Each blanket module has its own independent first wall which wraps around the plasma in the poloidal direction and shadows the blanket from any radiant energy from the plasma.

Figure 5.2-2 is a cross section of the reactor through the center of a TF coil showing the first wall following the contour of the blanket on the outboard side and the shield on the inboard side. The shape of the first wall in a blanket module can be better appreciated if it were unfolded onto a flat plane as shown in Fig. 5.2-3. To avoid the problem of accommodating varying widths as a function of the poloidal angle, the cooling tubes are oriented in the toroidal direction. Manifolds are provided in the poloidal direction on each side of the first wall module. A section of the first wall is shown in Fig. 5.2-4 indicating the inlet and outlet manifolds and the flow direction in the tubes. The first wall is shown curved toward the blanket on either side to make room for the manifolds and to allow adjacent first wall modules to butt against each other providing an uninterrupted cooled surface. Since the manifolds circumvent the chamber in the poloidal direction, they not only serve as conduits for the coolant but also provide reinforcement for the first wall module. Headers radiating outward through the blanket supply and return the helium gas to the manifolds and act as supports for the first wall. Section 5.4.1 describes the thermal hydraulics of the first wall where it is shown that two first wall modules are cooled in series. The connections between the headers of two series cooled first wall modules are made in the back of the blanket to facilitate the decoupling of the modules for maintenance purposes.

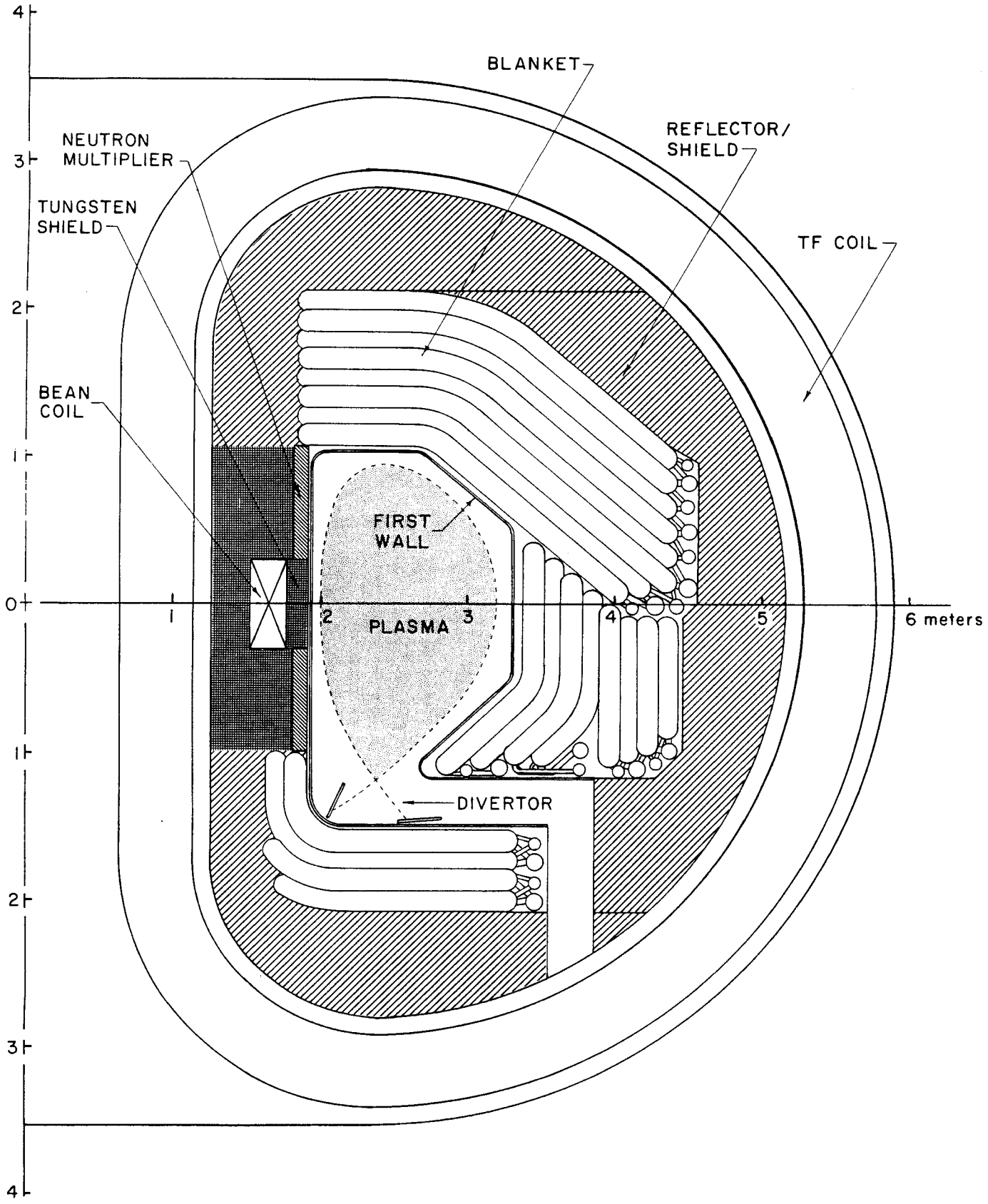

Fig. 5.2-2. Cross section of reactor through a TF coil.

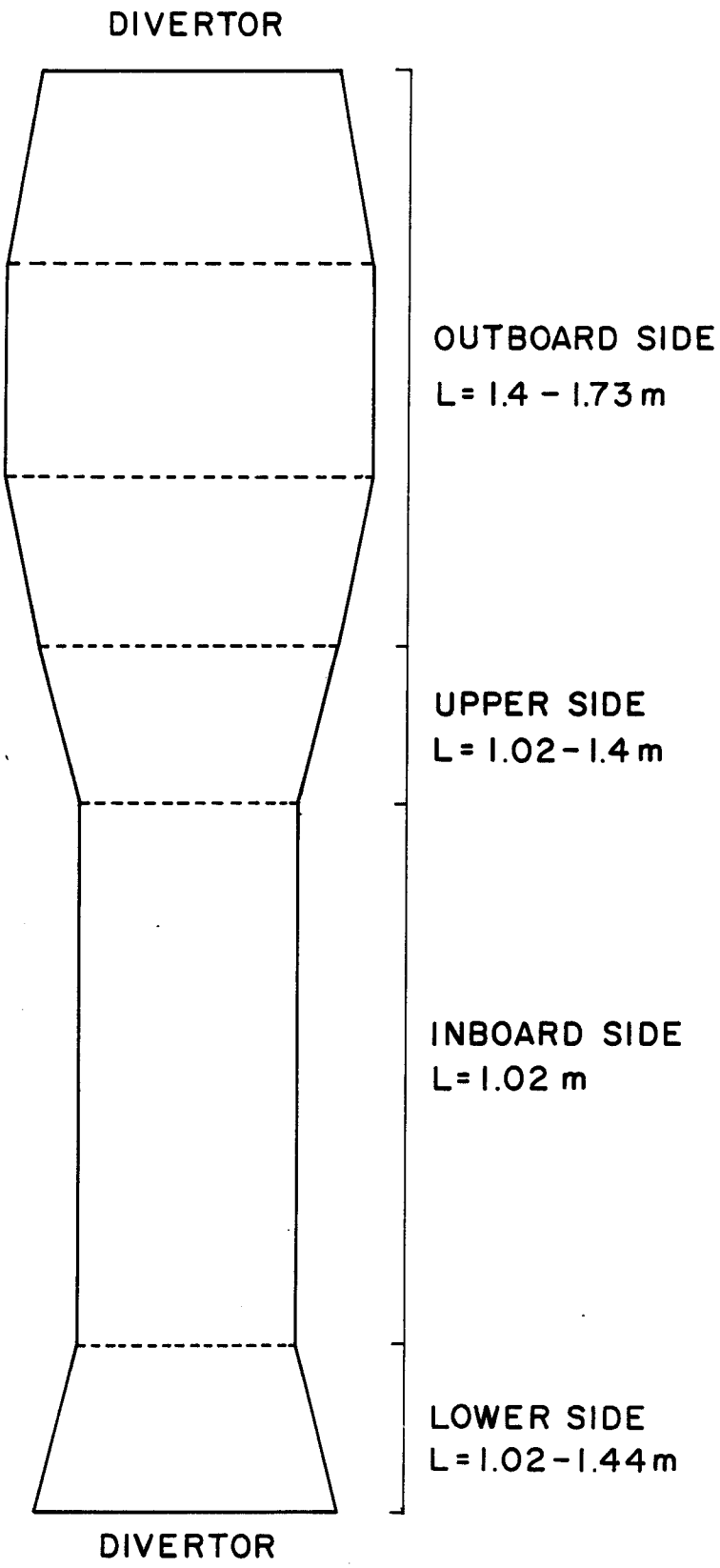

Fig. 5.2-3. First wall module unfolded onto a flat plane.

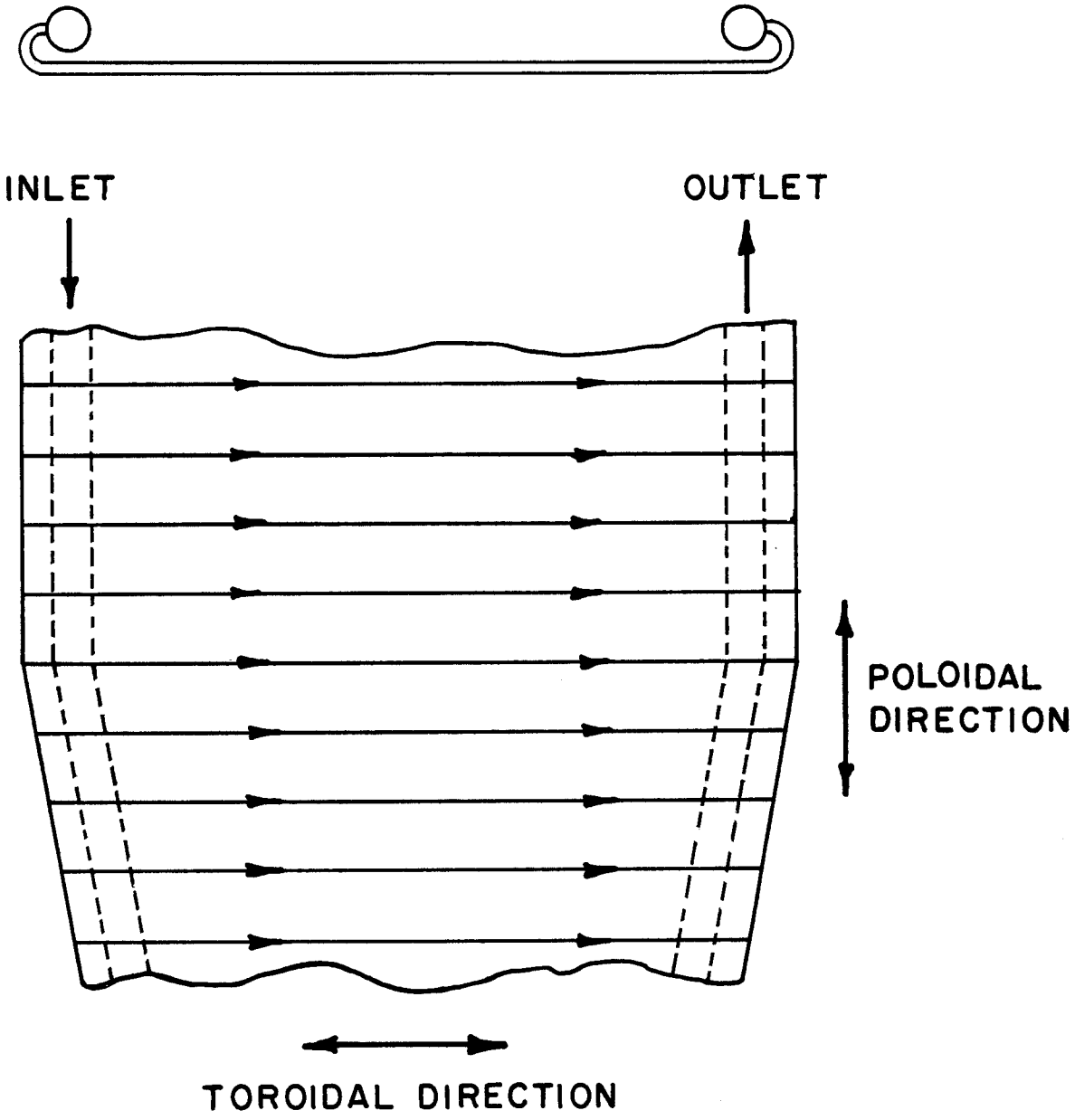

Fig. 5.2-4. First wall section showing manifolds and flow direction.

Although the first wall does not make contact with the blanket on the inside of the chamber and is independently cooled, it nevertheless is an integral part of a blanket module. When a blanket module is removed from the reactor, the first wall attached to it also comes out with it, leaving only the inboard shield in place. Thus, the first wall is serviced at the same time as a blanket, which at this high neutron wall loading will be about every two full power years.

Table 5.2-1 gives the physical parameters of the first wall.

Table 5.2-1. Physical Parameters of First Wall

Material of construction	HT-9
Coolant	Helium gas
Overall thickness (cm)	1.0
Tube ID (cm)	0.8
Tube wall thickness (cm)	0.1
Tube C - C distance (cm)	0.9
First wall total surface area (m^2)	106
First wall mass/module (tonnes)	0.30

5.2.2 Blanket

5.2.2.1 General Description

The blanket consists of 15 cm OD, ferritic stainless steel HT-9 cylinders containing static $Li_{17}Pb_{83}$, oriented poloidally as shown in Fig. 5.2-2, which is a cross section of the reactor through a TF coil. The cylinders cover the outboard side, the upper and lower side and a small fraction of the inboard side of the plasma chamber. The breeding material is cooled with 2.1 cm OD, 0.1 cm wall thickness tubes immersed in it with 80 atm helium coolant circulating through. The coolant tubes enter and exit the cylinder from one end making the manifolding relatively easy. After entering the cylinder, the coolant spirals helically around the inner cylinder wall from one end to the other, then turns around and travels back through the center of the cylinder as shown in Figs. 5.2-5 and 5.2-6. The large variation in nuclear heating from the first row to the last is controlled by providing coolant passages in parallel.

The cylinders are stacked on a triangular pitch forming eight rows as shown in Fig. 5.2-2 with an overall blanket thickness of 106 cm. They are all interconnected for easy filling and draining of the breeding material.

A blanket module consists of three cylinder assemblies, the upper, the middle and the lower, all structurally connected such as to act as a unit. The first wall is also an integral part of this unit. As can be seen in Fig. 5.2-2, this configuration includes a divertor. The upper cylinder assembly has the longest cylinders and they all have a 30° bend, with the sharpness of the bend depending on the location in the stack. Manifolds for this assembly can be seen in the back where they are readily accessible. The middle assembly has shorter cylinders. The first four rows are also bent 30° while

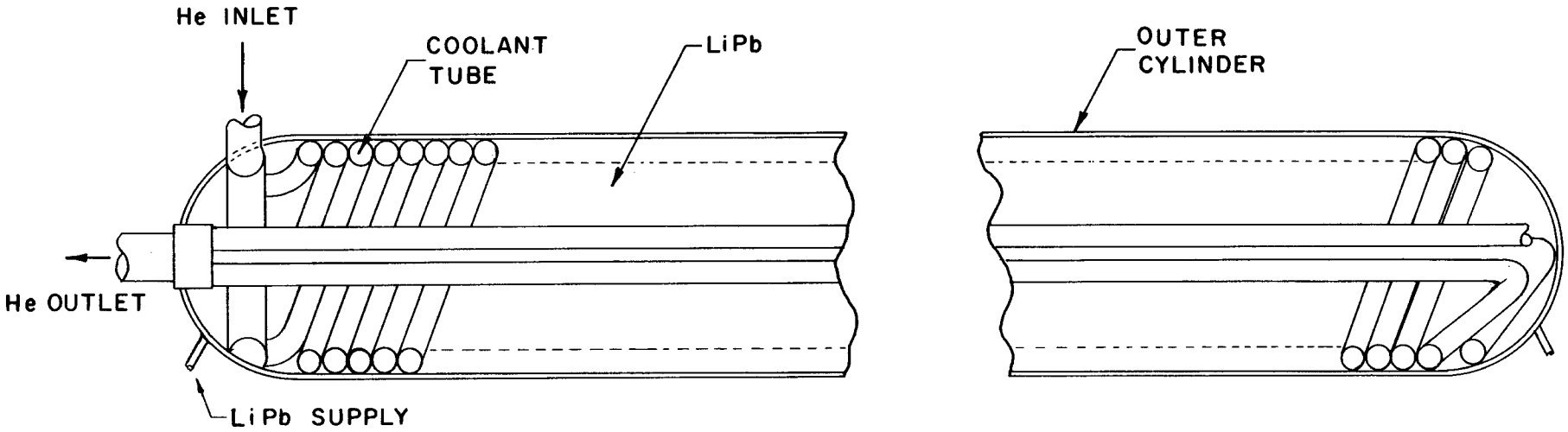

Fig. 5.2-5. Longitudinal cross section of a cylinder.

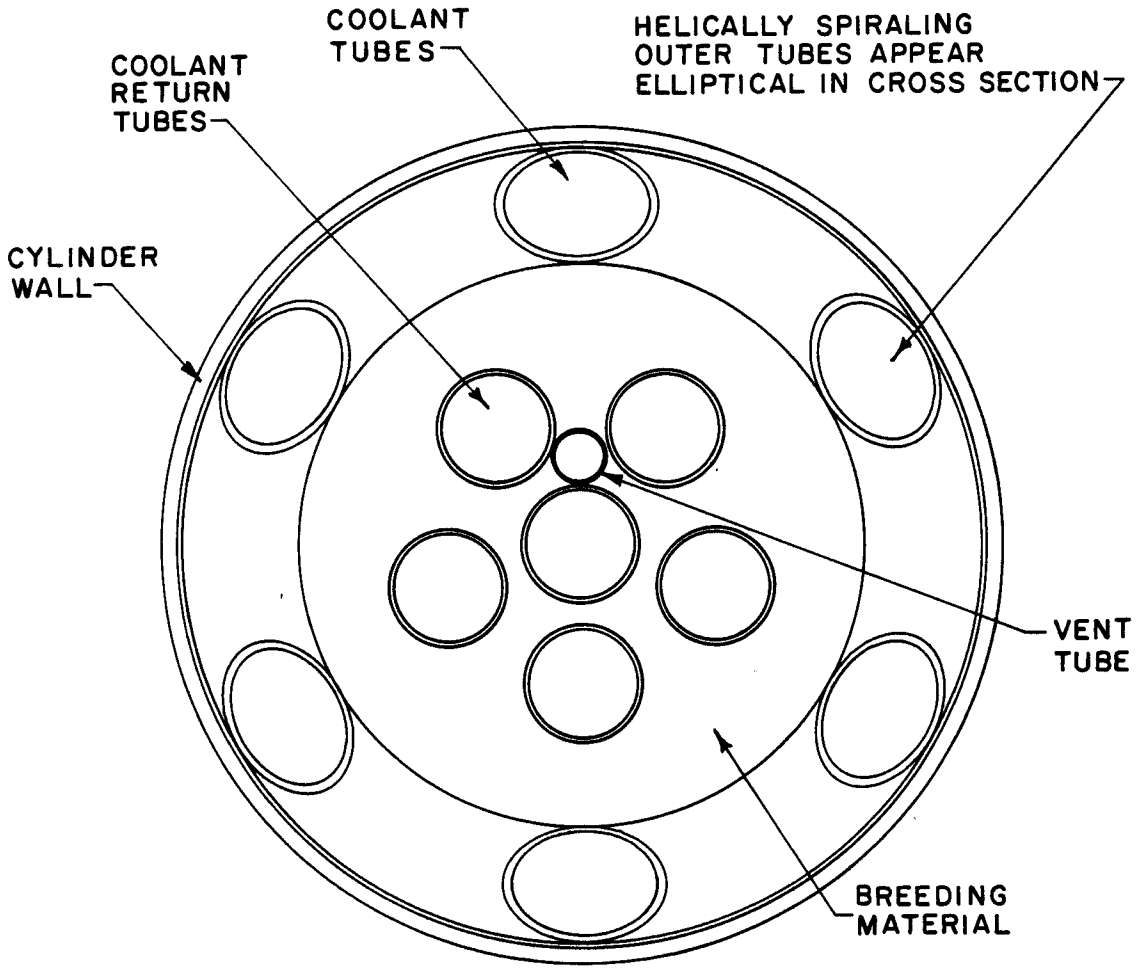

Fig. 5.2-6. Transverse cross section of a cylinder with 6 parallel cooling tubes.

the remaining are straight. Accessibility to the first several rows is not as good, but space for manifolds has been provided as can be seen in Fig. 5.2-2. The lower assembly has only four rows of cylinders and is 54 cm thick. These cylinders are bent 90° on a rather large bend radius, in order to cover the lower inner corner of the plasma chamber. In this way, we are able to provide the space for a single null divertor located at the bottom of the chamber. Manifolding for this cylinder assembly is also readily accessible.

Figure 5.2-7 is a top view of the first row of the upper cylinder assembly. It can be seen that the cylinder lengths are varied to accommodate the wedge shape of the module. Further, adjacent modules can have cylinder lengths adjusted to fill in the voids at the interface between them. Subsequent rows of cylinders are also interwoven to virtually eliminate any direct streaming through the blanket. In the last two rows, the number of cylinders is reduced by unity. This is done to decrease the circumferential space of the module at the top such that it can pass through the decreasing clearance between TF coils for maintenance. The horizontal lines at the top and bottom of the module shown in Fig. 5.2-2 indicate the interface between the parts that are removed for blanket maintenance and those that are permanent. Thus, the blanket, first wall divertor and the middle shield behind the blanket are all part of the module.

Table 5.2-2 gives the physical parameters of the blanket.

5.2.2.2 Cylinders

The blanket cylinders are 15 cm OD, 14.5 cm ID and of varying lengths. They have hemispherical heads and are, therefore, ideally suited for high pressure.

Table 5.2-2. Physical Parameters of the HWL Blanket

Cylinders	
Outer diameter (cm)	15
Inner diameter (cm)	14.5
Length (cm)	82 - 290
Type of bend	hemispherical
Coolant Tubes	
Outer diameter (cm)	2.1
Inner diameter (cm)	1.9
Distance between coils (cm)	0.1 - 15
Blanket Module	
No. of modules in reactor	12
No. of cylinders per module	202
Weight of module full of $Li_{17}Pb_{83}$ (tonnes)	49
Weight of module empty of $Li_{17}Pb_{83}$ (tonnes)	5.7

Material Fractions	1st row	8th row
$Li_{17}Pb_{83}$ (%)	51.3	75.5
HT-9 (%)	10.8	6.2
Void + He (%)	37.9	18.3

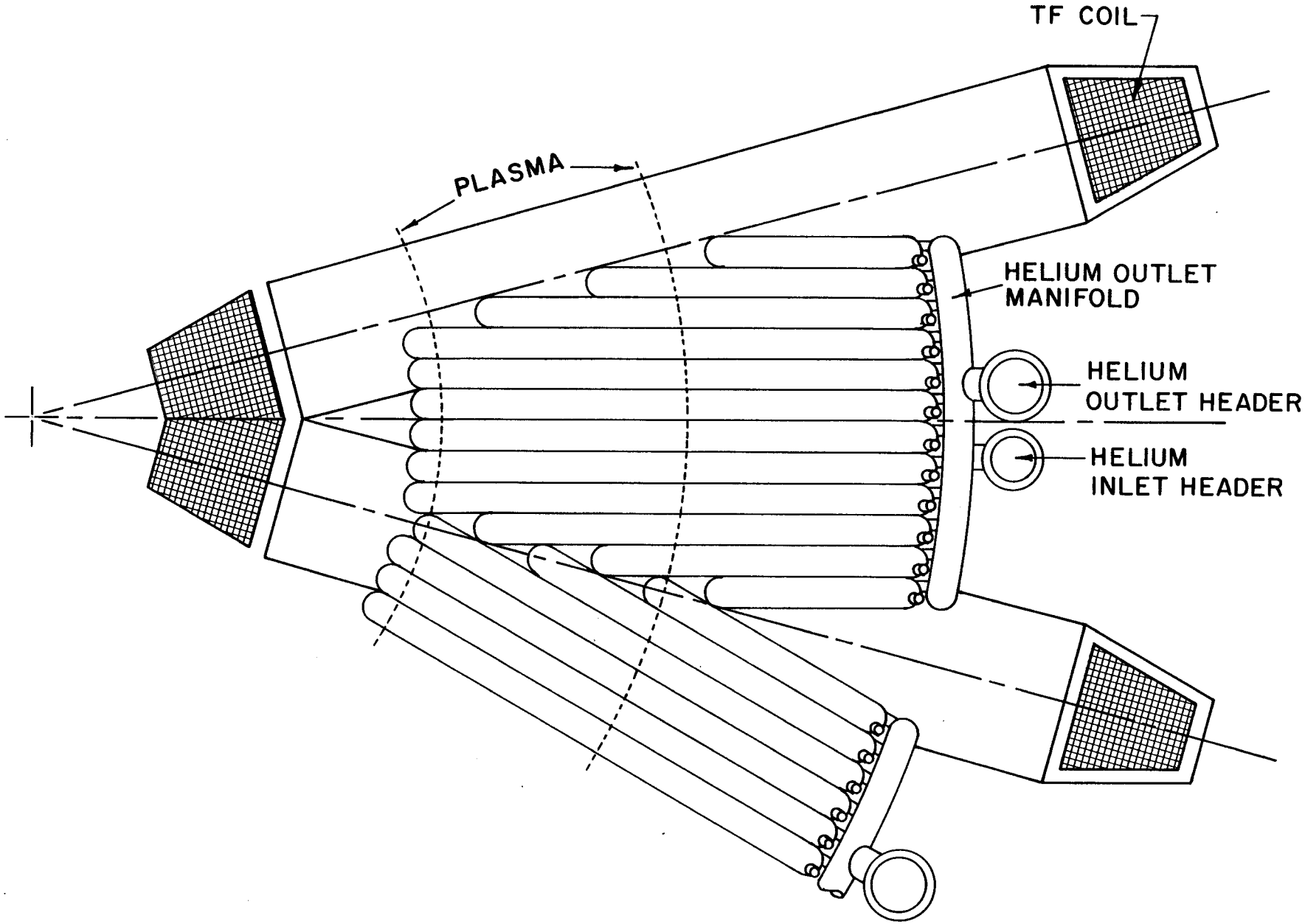

Fig. 5.2-7. Top view of the first row of cylinders in the upper cylinder blanket assembly.

If a coolant line ruptures then the cylinder gets pressurized to 80 atm or 8.1 MPa and the hoop stress in the cylinder at this point will be 239 MPa. This condition will exist for a very short period of time since a relief valve will immediately start draining the breeding material.

The average temperature of the cylinder is ~ 400°C and the yield strength of HT-9 at this temperature is 410 MPa. The hot spot on the cylinder wall is 535°C where the yield strength is 350 MPa.[7] Even if the leak is not detected in time to shut off the plasma and the relief valve fails to operate, there is no danger of material yielding at the hot spot.

5.2.2.3 Cooling Tubes

The cooling tubes are 2.1 cm OD, 1.9 cm ID and are also made of HT-9. The first row of cylinders has the highest nuclear heating and will have six tubes spiraling in parallel (see Figs. 5.2-5 and 5.2-6). The number of parallel circuits is reduced to 3 in the second row, 2 in the third row and only one in the remaining rows. Tubes are spaced 0.1 cm apart and come within 0.1 cm of the cylinder wall. In the back rows, the spacing between tubes is increased to account for the much lower nuclear heating.

At the operating helium pressure of 8.1 MPa the stress in the tubes is 81 MPa, a factor of 2 below the allowable design stress for HT-9 at 530°C.[7,8] Unlike the cylinders, the tubes will be continuously stressed and are, therefore, designed for a much higher safety margin.

Since the helium velocity in the tubes approaches 100 m/s, there is some concern about possible vibration in the return legs. It would seem that intermediate supports could be incorporated to prevent this from occurring.

In cases where there are several parallel cooling circuits such as in the first three rows of cylinders, the tubes are manifolded with a common header

at the inlet and the outlet as shown in Fig. 5.2-5. Further, at the opposite end of the cylinder where the tubes turn around for the return, provision has to be made that adequate cooling is available everywhere. This is particularly true for the first row of cylinders where the nuclear heating is high and the temperature of the coolant is close to its maximum at the turnaround point. One possible solution is to have the tubes combine their flow into a hemispherical plenum with the return tubes also connected into this plenum. This would insure that cooling will be available for the whole surface of the cylinder end.

There are several obvious advantages to this cooling tube arrangement:

1. The helical configuration allows tubes to expand when heated without high stresses.
2. The coolant pressure will expand the coils insuring contact with the cylinder wall.
3. Parallel coolant circuits, adjusting the spacing between coils and flow orificing, gives a very high degree of control on the cooling as a function of nuclear heating.
4. The coolant is manifolded on one end of the cylinder simplifying the coolant distribution within the modules.

5.2.2.4 Support Considerations

One of the attractive features of this blanket design is that it can expand freely when cycled in temperature. Any support scheme, therefore, should not restrict this capability. It would seem that banding the cylinders together would provide support but not restrict expansion.

The upper assembly is the largest of the three. Providing bands that go around the assembly and attach it to the shield seems reasonable. The bands

would be in the 3.7 m radius of the reactor region (see Fig. 5.2-2) where they would be shielded by the middle assembly and have little nuclear heating. Further, the spaces between the rows in the middle assembly at the top provide room for the bands. When assembled in the reactor, the front part of the upper blanket assembly is supported on the inboard shield. Thus when it is full of $Li_{17}Pb_{83}$ it is well supported on both ends.

Banding the middle and lower blanket assemblies is easier, because they are smaller. However, because the bands have to be exposed to high nuclear heating, they will have to be cooled. It may be possible to combine the cooled bands with the first wall supports. In any case, the bands would be helium cooled as are the first wall and the blanket. The bands only hold the cylinders in an assembly together, but the mass of the blanket is ultimately supported through the shield to the building foundation. It is interesting to note that the whole blanket filled with breeder material weighs 590 tonnes, or just under 50 tonnes per module. When emptied of breeding material, the blanket module weighs only 5.8 tonnes and is heavily counterbalanced by the shield part of the module. This means that the blanket/shield module will be quite stable during radial displacement for maintenance.

5.2.2.5 Manifolding

The coolant distribution within the cylinders was discussed in Section 5.2.2.3. Figures 5.2-2 and 5.2-7 show manifolds oriented toroidally which supply and return the helium gas to and from the cylinders. These manifolds in turn are connected to headers shown in Fig. 5.2-7 which fall between TF coils and therefore do not compromise shielding. Although Fig. 5.2-2 shows each manifold as serving two rows of cylinders, there is a fair amount of flexibility in routing the helium coolant to the different rows.

5.2.2.6 Filling and Draining the Blanket

The cylinders within an assembly in a module are interconnected on the helium manifold side in order to facilitate filling and emptying the blanket with breeding material. The normal procedure for filling the blanket is to pump it down to a roughing vacuum ($\sim 10^{-2}$ torr) and then to fill from the bottom up. Because the cylinders are interconnected, only a single breeding material supply line per assembly will be needed.

To insure that a bubble will never be trapped near the top of any cylinder, an open ended tube can be provided from the bottom reaching all the way to the top, and connected to a vent on the manifolding end of the cylinder. Such a tube can be attached to one of the helium return tubes in the center of the cylinder and can be used for the initial evacuation of the cylinders as well as for backfilling them with an inert gas as the breeding material is drained out by gravity.

In order to control the pressure in the breeding material during reactor operation, the fill lines will be connected to a free surface equipped with an automatic pressure control system. Further, a relief valve will be provided for each blanket assembly with a drain into the dump tank. This relief valve will open in the event the pressure in the blanket assembly exceeds the control pressure, such as in the case of a helium coolant tube rupture.

5.2.2.7 Fabrication

Fabrication of the blanket cylinders would have been straightforward had it not been for the need to have bends in them to accommodate the shape of the reaction chamber. To fabricate the straight cylinders, the coiled coolant and return tubes are attached to one hemispherical head, then the assembly is inserted into the open end of a cylinder and finally the hemispherical head

welded to the cylinder. It should be made clear at the outset that fabricating the bent cylinder itself is trivial. The complication comes from inserting the coiled tubes with the integral return tubes into the bent cylinders.

Two methods have been proposed for accomplishing this task, both of which start out with a bent cylinder and both will require some development. In the first method, the bent cylinder is cut circumferentially through the elbow, then reassembled with the prebent return tubes in place. Welding the cylinder halves will be easy because the return tubes will remain in the center of the cylinder. The next step is to insert the coiled outer tubes into the cylinder. Because they are coiled as in a spring, they can be pushed and pulled around the bend until they reach from one end of the cylinder to the other. In the final step, the cooling tubes are connected together and the hemispherical ends welded onto the cylinder.

The second method depends on the development of a way for welding portions of the cylinder with the coiled tubes in close proximity. This effectively means that the elbow can be cut out, slit lengthwise and then reassembled like a clam around the prebent coiled tubes and finally welded in place. The rest of the fabrication would be similar to a straight cylinder.

One of the advantages of this blanket concept is that each cylinder can be thoroughly tested and inspected prior to its inclusion into a module assembly. The tests would include radiographic and other inspections of the welds, and hydrostatic testing of both cooling tubes and cylinders. Finally, pressurizing the tubes with helium gas while evacuating the cylinders and thermally cycling them will further insure their reliability.

References for Sections 5.1 and 5.2

1. B. Badger et al., "WITAMIR, A Tandem Mirror Reactor Study," UWFDM-400, Fusion Engineering Program, Nuclear Engineering Department, University of Wisconsin, Madison, September 1980.

2. B. Badger, F. Arendt et al., "TASKA, A Tandem Mirror Fusion Engineering Facility," UWFDM-500, KfK-3311, Fusion Engineering Program, Nuclear Engineering Department, University of Wisconsin, Madison, and Kernforschungszentrum, Karlsruhe, FRG, March 1982.

3. "MARS - Tandem Mirror Reactor Study," coordinated by LLNL, in publication.

4. M. Abdou et al., "Blanket Comparison and Selection Study," Interim Report ANL/FPP-83-1, Vol. I, September 1983.

5. BCSS Review Committee Report on the March 19, 1984 three-quarter term review.

6. Dale L. Smith, "BSCC Project Meeting - Liquid Metal Blanket Concepts," Argonne National Laboratory, September 13-14, 1983.

7. J.M. Rawls et al., "Assessment of Martensitic Steels as Structural Materials in Magnetic Fusion Devices," GA-A15749, General Atomic Co., January 1980.

8. Dale L. Smith, "BSCC Project Meeting - Materials Assessment," Argonne National Laboratory, September 13-14, 1983.

5.3 Neutronics Analysis

5.3.1 Introduction

There has been a growing interest recently in not breeding on the inboard side of tokamaks. The impact on the overall tritium breeding ratio (TBR) has been investigated for different designs with emphasis on solid breeders.[1-3] There is a larger incentive for not breeding on the inboard side of a high wall loading (HWL) tokamak such as the design under consideration in this study. Achieving a high fusion power density in such a reactor requires large magnetic fields on the plasma axis. It is therefore essential to reduce the space between the plasma and the inboard leg of the TF coil. A breeding blanket and a magnet shield are usually used in this space. Since the breeding blanket is not an effective neutron shield, it is preferable to replace it by a more effective shield that reduces the space required for adequate magnet protection from the high neutron wall loading environment. Furthermore, the reactor compactness makes it difficult to maintain or replace an inboard blanket.

The primary goal of the neutronics analysis presented here is to determine whether an adequate overall tritium breeding ratio can be obtained in the HWL blanket design. The impact of the material used on the inboard side on tritium breeding in the outboard blanket is assessed. One-dimensional analysis has been performed to determine the local tritium breeding ratio and blanket energy multiplication. Because of the limited breeding blanket coverage in the HWL design, dictated by the requirement that the LiPb in the blanket cylinders be drainable, a relatively thick blanket is used to maximize the local tritium breeding ratio. Detailed three-dimensional neutronics calculations have been performed to determine the overall tritium breeding

with different materials on the inboard side. An overall TBR $\gtrsim 1.05$ is required in the three-dimensional calculations to allow for tritium losses and radioactive decay and supplying fuel for startup of other fusion reactors. The neutronics characteristics for the final HWL blanket design have been determined from the three-dimensional calculations.

5.3.2 Neutron Wall Loading Distribution

The neutron wall loading in a tokamak reactor has a poloidal variation that depends on the plasma shape, the neutron source distribution in the plasma and the first wall shape. The poloidal neutron wall loading distribution has an important impact on the reactor thermal-hydraulics design and magnet shield design. The NEWLIT code described in Section 8 was used to calculate the poloidal variation of the neutron wall loading in the HWL reactor. The results are given in Fig. 5.3-1. The wall loading distribution in each segment of the first wall is indicated. The dashed line represents the average wall loading which was determined to be 8.68 MW/m^2. The peak reactor wall loading of 12 MW/m^2 occurs at the reactor midplane on the outboard side. The peak wall loading on the inboard side occurs at the midplane indicating that the hot spot in the inboard leg of the TF coil is at the reactor midplane.

5.3.3 Impact of Inboard Material on Tritium Breeding

Proper choice of the material used on the inboard side is essential. Materials that provide large neutron reflection are required to enhance tritium breeding in the outboard breeding blanket. Calculations were performed to compare the ability of the different materials to reflect neutrons. In these calculations different shielding materials and neutron multipliers were considered. A realistic composition that allows for

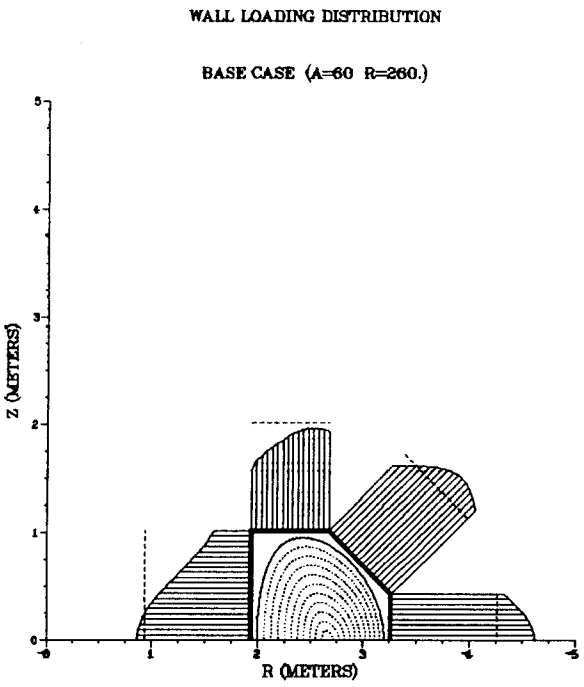

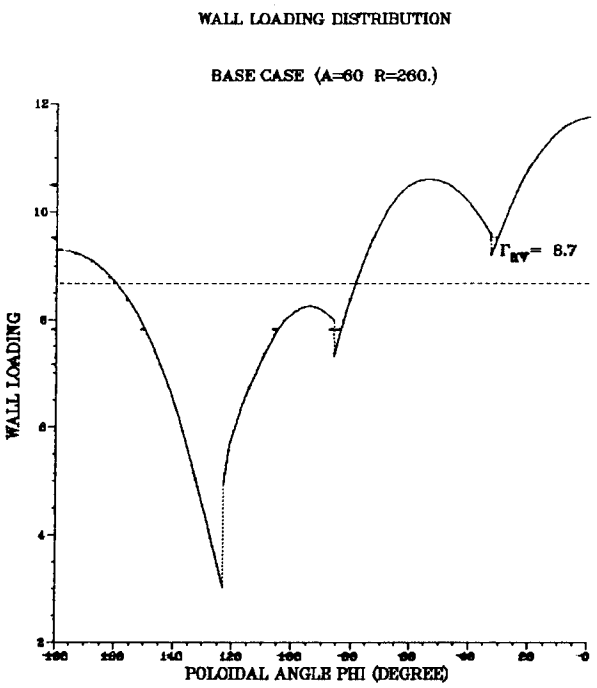

Fig. 5.3-1 Poloidal variation of the neutron wall loading in the HWL reactor.

structural material and cooling was used. The albedo, which is the measure of the number of neutrons, regardless of their energy, reflected from the inboard material per 14.1 MeV incident neutron was calculated for 40 cm thick slabs. The calculated values for the 14 MeV albedo are given in Table 5.3-1. Similar calculations were performed by Micklich and Jassby.[4] However, no allowance was made for the required structural material and coolant.

While the albedo values indicate the ability of the material to reflect the source 14 MeV neutrons, many secondary neutrons originating in the outboard blanket will be incident on the inboard material. Hence, the 14 MeV albedo is not an accurate measure of the impact of the inboard material on tritium breeding. This can be properly assessed by performing a neutron transport calculation in which both the inboard shield and outboard blanket are included.

We performed a one-dimensional toroidal cylindrical geometry calculation using the model shown in Fig. 5.3-2. In this model, the reactor parameters given in Chapter 2 were used. A representative 80 cm thick outboard blanket was used. The calculations have been performed for two outboard blanket designs: a natural liquid lithium blanket and a $Li_{17}Pb_{83}$ blanket with 90% ^{6}Li enrichment. A 30 cm thick stainless steel reflector is included behind the blanket to properly account for the boundary condition at the outer edge of the blanket. The calculations were performed using the discrete ordinates code ONEDANT[5] with cross section data based on the ENDF/B-V evaluation. The P_3-S_8 approximation was used. Notice that the top and bottom breeding blankets are not included in this one-dimensional model. The breeding blanket coverage fraction in the model is only 63%.

Table 5.3-1. Impact of Inboard Material on TBR

Inboard Material	TBR (63% Coverage)/TBR (Full Coverage) Outboard Li Blanket	Outboard $Li_{17}Pb_{83}$ Blanket	14 MeV Albedo
Be	0.840	0.733	1.77
Pb	0.830	0.719	1.60
C	0.726	0.636	0.69
SS	0.734	0.621	0.75
Cu	0.720	0.596	0.79
W	0.716	0.572	0.96
H_2O	0.653	0.550	0.39
TiH_2	0.626	0.494	0.40
B_4C	0.608	0.468	0.47

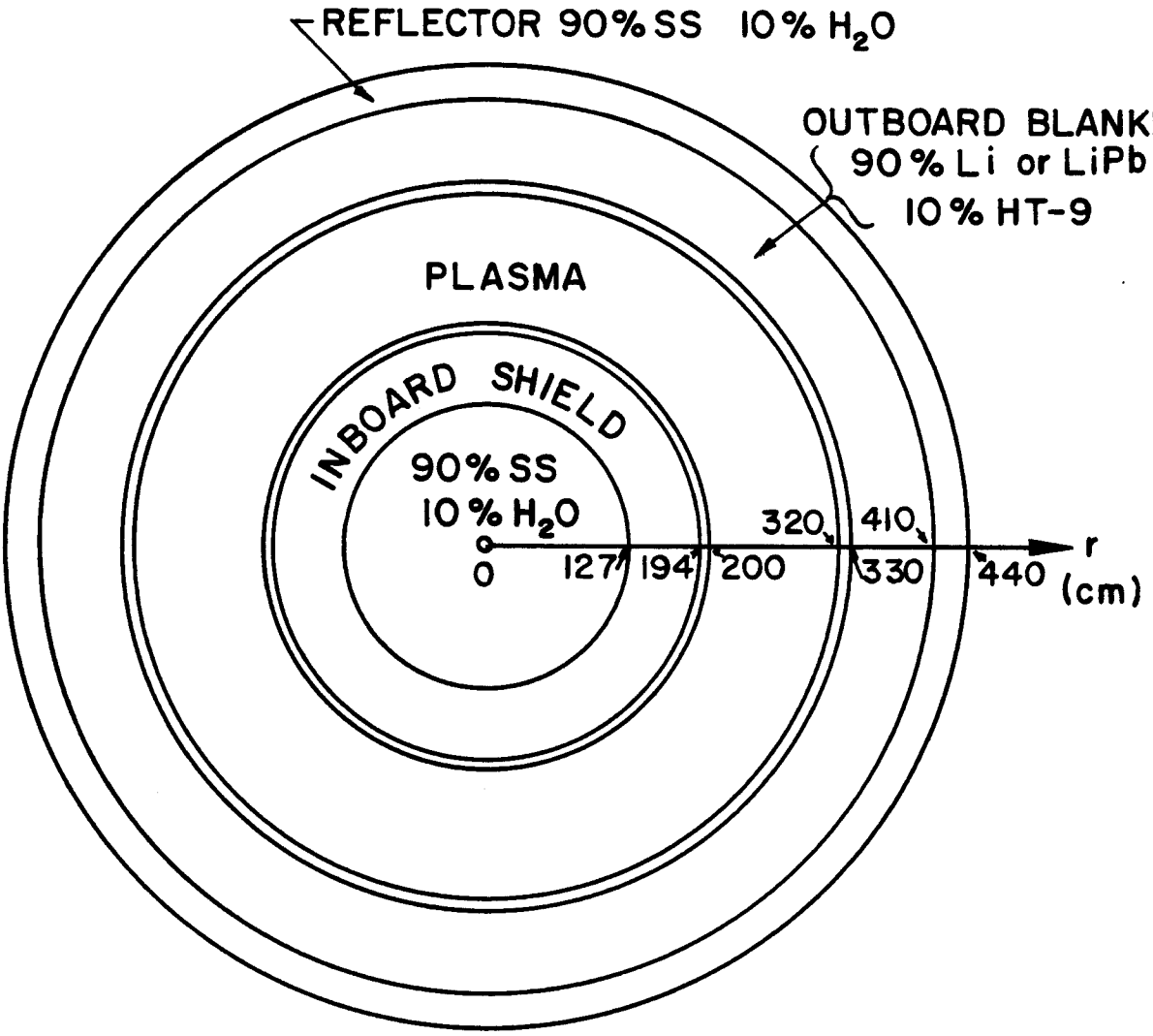

ONE DIMENSIONAL TOROIDAL CYLINDRICAL MODEL

Fig. 5.3-2 The one-dimensional toroidal cylindrical model used to investigate the impact of inboard material on TBR.

Table 5.3-1 gives the ratio of the TBR obtained with the different inboard materials to the TBR obtained with full breeding blanket coverage. Again, realistic inboard material compositions that allow for the required coolant and structure were used. The results are given for both the Li and LiPb outboard blanket cases. Note that a ratio > 0.63 implies that replacing the inboard breeder by the given material yields more tritium breeding in the outboard blanket. More inboard materials enhance outboard breeding when they replace Li than LiPb. The reason is that Li is a strong neutron absorber while LiPb is a good neutron multiplier in addition to being a strong neutron absorber in the low energy region.

Comparing these results with the 14 MeV albedo values, the inadequacy of the 14 MeV albedo for predicting the impact of the inboard material choice on tritium breeding is clear. For example, while tungsten has the largest 14 MeV albedo among inboard shields other than neutron multipliers, it yields a TBR lower than that obtained using most of the other materials. This is due to its large neutron absorption cross section in the resonance and lower energy ranges. It is clear from the results of Table 5.3-1 that the neutron multipliers (Be and Pb) used on the inboard side give the best overall TBR. The strong neutron absorber B_4C yields the least overall TBR. In general, the ranking of the different TBRs is the same for both Li and LiPb blankets. The only exception is that while stainless steel is slightly better than graphite in the Li outboard blanket case, graphite is better than stainless steel in the LiPb outboard blanket case. This is due to the superior moderating properties of graphite that yield a large soft neutron spectrum reflecting back to the outboard blanket enhancing tritium breeding in ^6Li which dominates the TBR for LiPb.

Fig. 5.3-3 is a bar chart that shows the overall TBR obtained using the model of Fig. 5.3-2 with different inboard materials. It is clear that while the overall TBR with full breeding blanket coverage is larger for LiPb than for Li, the overall TBR is more sensitive to the breeding blanket coverage fraction and inboard material choice when LiPb is used. This is attributed to the large neutron multiplication in the LiPb outboard blanket that results in larger reflection into the inboard shield than for the Li blanket case. The 14 MeV albedo values for the Li and LiPb blankets were calculated to be 0.85 and 1.14, respectively.

The results of this section will be used together with the local TBR obtained from the one-dimensional calculations for the HWL blanket to make an estimate for the overall TBR as will be discussed in the following section. However, it needs to be emphasized that the choice of the inboard material is a tradeoff between minimizing the inboard shield thickness and enhancing the TBR in the outboard blanket.

5.3.4 One-Dimensional Analysis

The one-dimensional calculations for the HWL blanket were performed using the ONEDANT[5] code with 30 neutron-12 gamma energy group cross section data based on the ENDF/B-V evaluation. The P_3S_8 approximation was used. A poloidal cylindrical geometry model was used implying full breeding blanket coverage. Therefore, the results are indicative of the local neutronics parameters. The blanket consists of several rows of cylinders 15 cm in diameter. These cylinders are made of the ferritic steel alloy HT-9 and contain a stationary $Li_{17}Pb_{83}$ breeder enriched to 90% ^6Li and cooled by helium gas. The first wall is 1 cm thick and is made of HT-9 and cooled by helium gas. The structure content in the first wall is 30%. Detailed descriptions of the first wall and blanket design are given in Section 5.2.

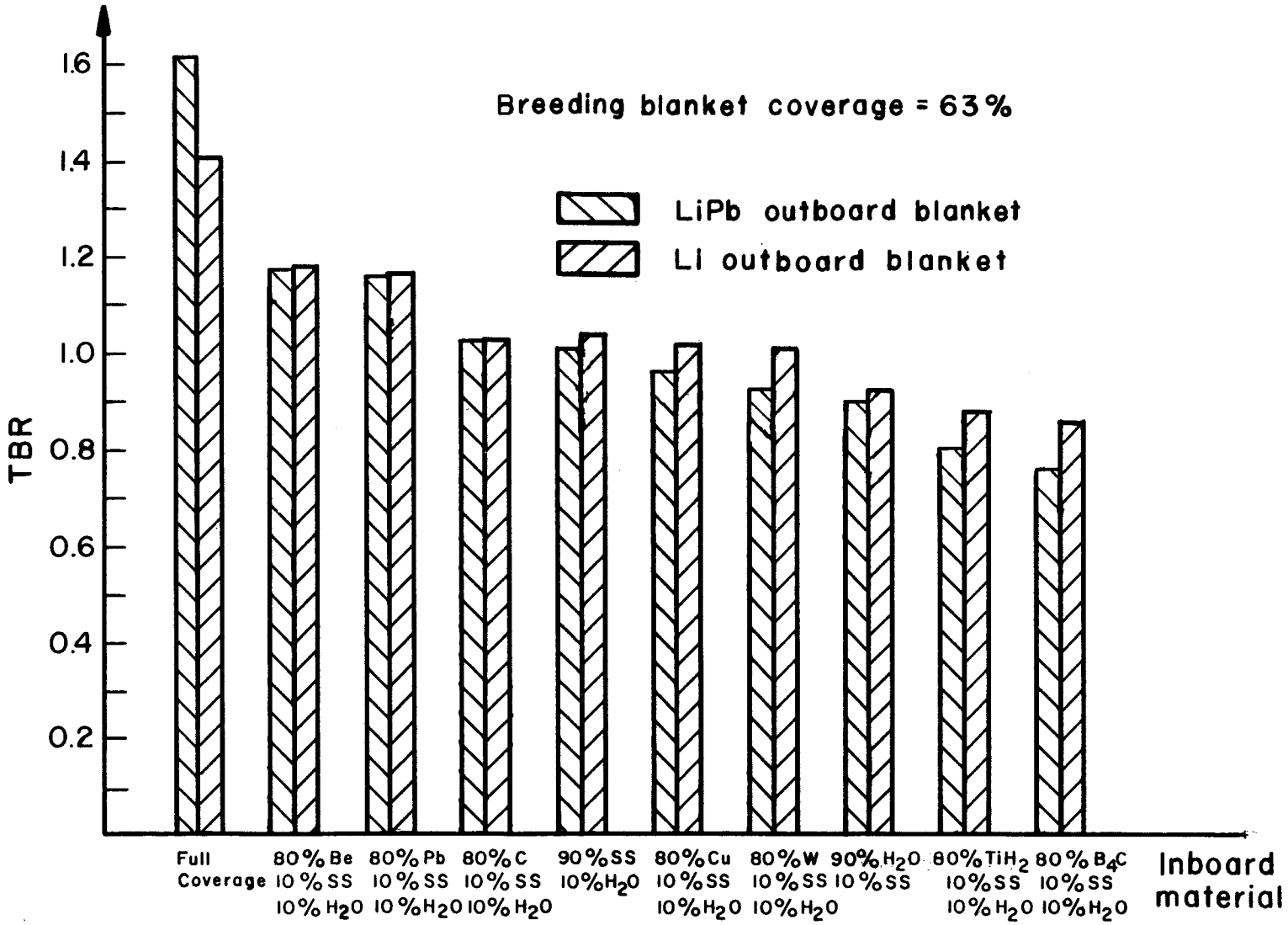

Fig. 5.3-3 The overall TBR using different inboard materials for Li and LiPb outboard blankets.

The geometrical model used in the calculations is shown schematically in Fig. 5.3-4. A 10 cm scrapeoff zone is considered with a first wall radius of 70 cm. The 6 cm space between the first wall and the blanket is considered to allow for accommodating the first wall coolant manifolds. A 60 cm thick water cooled Fe 1422 reflector/shield is used behind the blanket. The volume fractions of the constituents of the different cylinders were determined from a thermal-hydraulics analysis. The structure content as well as the He coolant content decrease as one moves away from the plasma deep in the blanket due to the degradation in nuclear heating.

Several one-dimensional calculations have been performed using different numbers of cylinder rows. Both the local TBR and energy multiplication (M), defined as the ratio of the nuclear energy deposited in the first wall, blanket and reflector to the fusion neutron energy incident on the first wall, were calculated. The results are shown simultaneously in the tritium breeding-energy multiplication (T-M) plot[6] in Fig. 5.3-5. Increasing the blanket thickness T increases while M decreases. The decrease in M is due to the fact that a neutron absorbed in ^{6}Li releases ~ 4.8 MeV, while ~ 8 MeV is released if it is parasitically absorbed in the reflector structure. The primary goal here is to maximize the local TBR because of the limited breeding blanket coverage fraction in the HWL reactor design. A local TBR of 1.5 is obtained using a 106 cm thick blanket consisting of eight rows of cylinders. Adding another row of cylinders will insignificantly increase the local TBR while increasing the reactor direct cost as larger TF coils are required to provide enough space between the outboard legs of the coils that allows for removing the blanket modules.

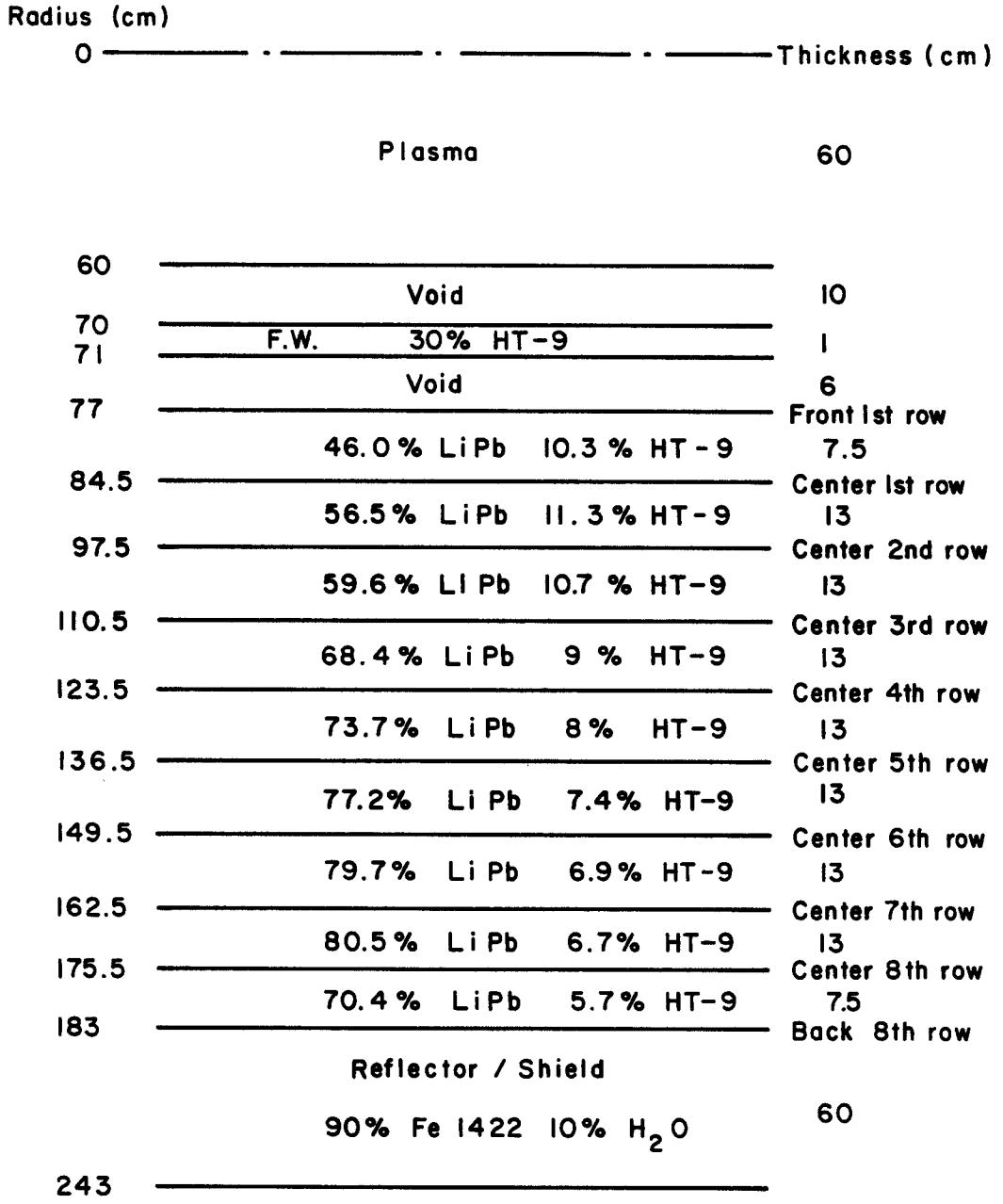

Fig. 5.3-4 The geometrical model used in the one-dimensional calculations.

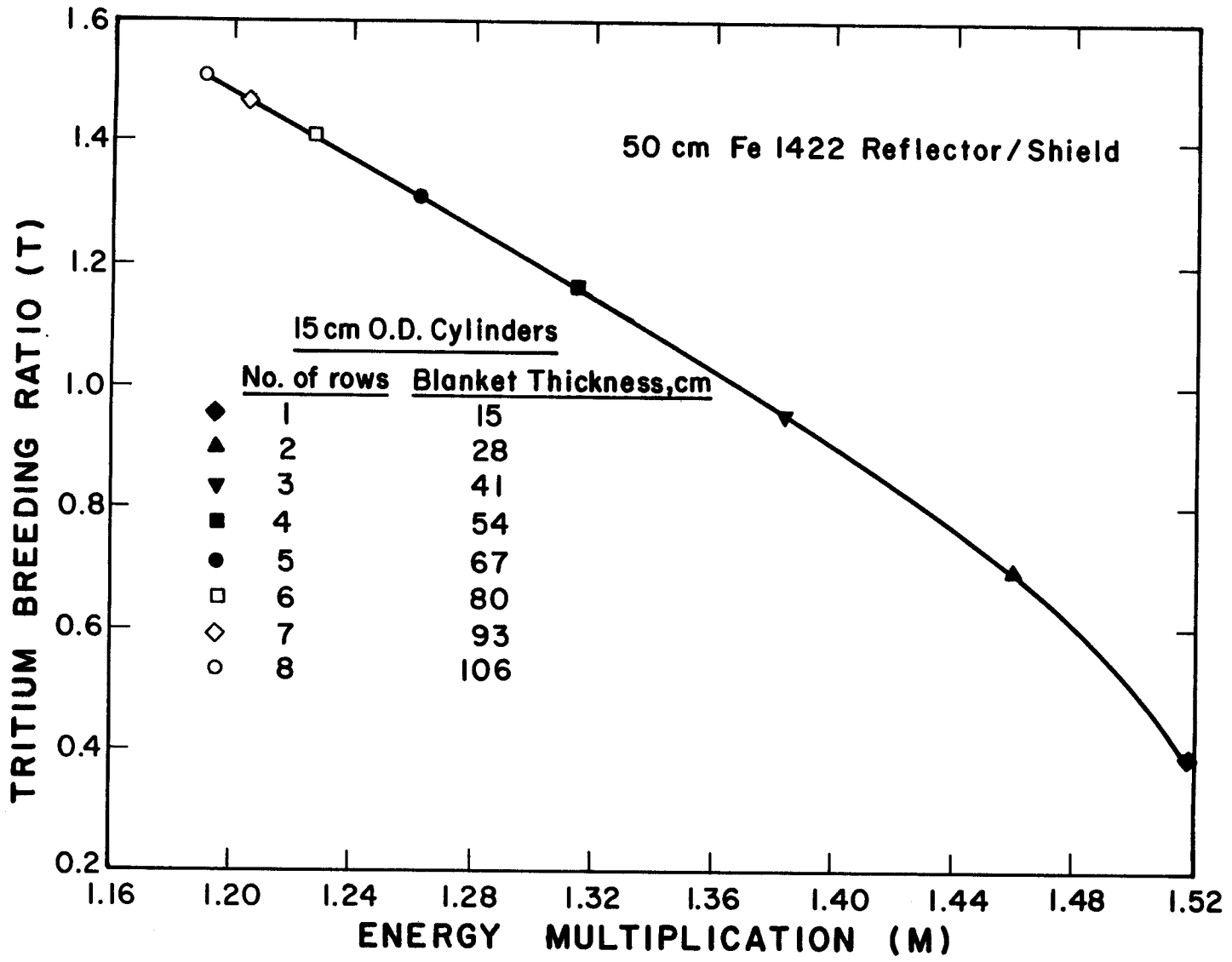

Fig. 5.3-5 The T-M plot for the HWL blanket with the effect of number of cylinder rows.

The option of using a graphite reflector to enhance the TBR was considered. The results are shown in Fig. 5.3-6 for a preliminary design in which 17.6 cm diameter cylinders were used. It is clear that replacing the steel reflector by graphite increases T and reduces M. The effect is more pronounced when a thin blanket is used. The TBR enhancement is very small when a thick blanket is used as most of the breeding occurs in the front rows of cylinders. Hence, using a graphite reflector in the HWL reactor design is not justifiable.

Figure 5.3-7 shows the radial variation of power density in the first wall, blanket, and reflector. The contributions from neutron and gamma heating are also shown. The results are normalized to a unit neutron wall loading. Based on a peak neutron wall loading of 12 MW/m^2 at the reactor midplane on the outboard side, a peak power density of 72 W/cm^3 is obtained in the first wall. The peak power density in the blanket structure is 64 W/cm^3 and the peak power density in LiPb is 93 W/cm^3. The peak blanket power density is 87 W/cm^3 of the non-void material (HT-9 + LiPb). The peaking at the back of the blanket is attributed to the absorption in lead of the gammas generated in the metallic reflector. It is strong gamma absorption in lead that results in shifting the peak power density in the reflector away from the interface with the blanket. Using the poloidal variation of wall loading given in Fig. 5.3-1 together with the results of Fig. 5.3-7, we calculated the average power density in the front row of cylinders of the outboard blanket to be 47 W/cm^3. The average power density in the front row of cylinders in the top blanket is 24 W/m^3. These results represent a useful input for the thermal analysis discussed in Section 5.4.

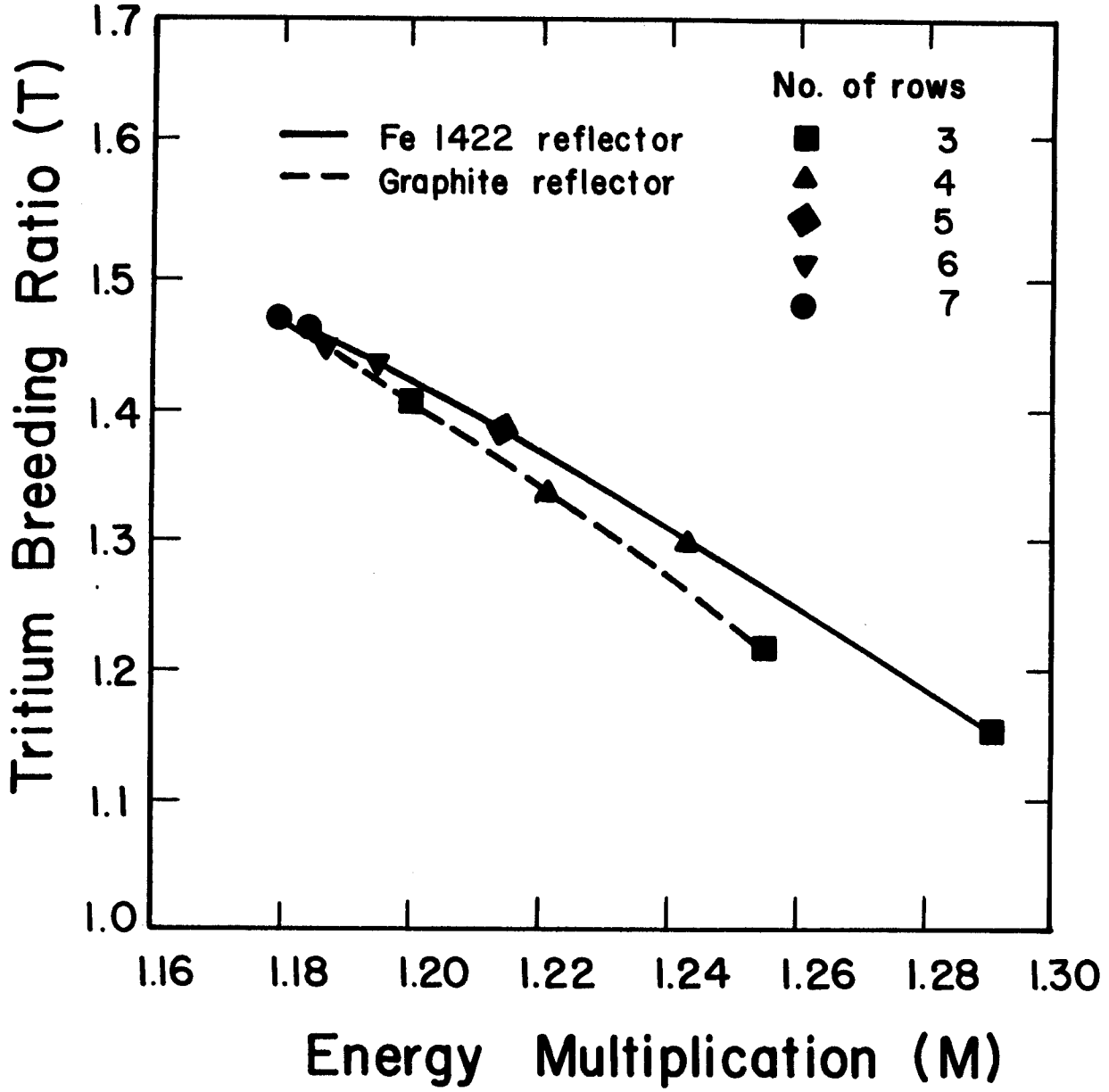

Fig. 5.3-6 Effect of using graphite reflector on tritium breeding and energy multiplication.

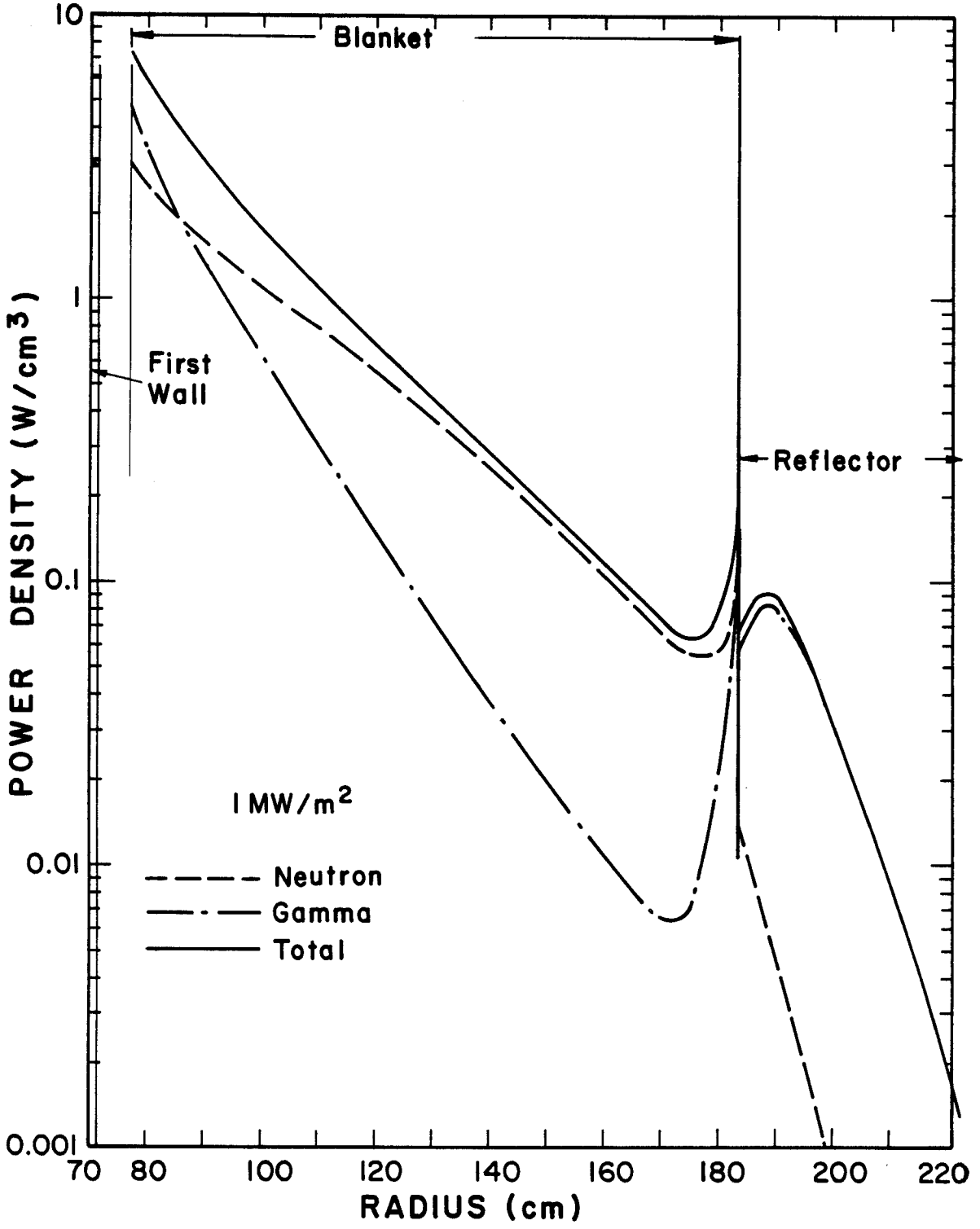

Fig. 5.3-7 Radial variation of power density in the HWL reactor.

The results of Table 5.3-1, indicating the effect on tritium breeding of using different materials in the portions not covered by breeding blanket, were utilized together with the one-dimensional local TBR results to give a preliminary estimate for the overall TBR in the HWL reactor. The coverage fractions for the different reactor segments are given in Table 5.3-2. The coverage fraction corresponds to the solid angle fraction subtended by the particular segment as seen by the source neutrons in the plasma. For a first order approximation, the fraction of the first wall area in front of each segment was used to calculate the coverage fraction. Notice that the coverage fraction for the bottom blanket segment was considered to be the same as that for the top blanket segment since the solid angles subtended by both segments are identical even though the lower blanket has a larger first wall area due to the divertor penetration.

The impact on the overall TBR of using a different number of breeding blanket cylinder rows in the different segments is given in Table 5.3-3. The impact of using different materials in the non-breeding blanket zones in the HWL reactor was investigated. However, in order to not jeopardize the magnet shielding, the optimum shield composition, determined from the magnet shield optimization presented in Chapter 7, was used in the bean coil zone where the peak radiation effects occur in the superconducting TF coil. A tungsten shield consisting of 80% W, 10% Fe 1422, and 10% H_2O is used between the bean coil and the first wall in this zone. Because of its lesser impact on reducing the TBR, stainless steel (90% Fe 1422 and 10% H_2O) is used behind the first wall in the other non-breeding zones. The possibility of enhancing the overall TBR by using a layer of a neutron multiplier behind the first wall in the upper and lower inboard zones was considered.

Table 5.3-2. Coverage Fractions for the Different Reactor Segments

Reactor Segment	Coverage Fraction
Upper inboard segment	9.2%
Bean coil zone	7%
Lower inboard segment	9.2%
Top blanket	11.3%
Bottom blanket	11.3%
Outboard blanket	49.8%
Space between blanket modules	2.2%

Table 5.3-3. TBR Versus Number of Blanket Cylinder Rows

No. of Rows	TBR
1	0.38
2	0.70
3	0.95
4	1.16
5	1.31
6	1.41
7	1.47
8	1.50

Table 5.3-4 summarizes the overall TBR estimate for the different options. In Case 1, no tritium breeding blanket is utilized in the bottom zone yielding a low value for the overall TBR. Cases 2, 3 and 4 show the effect of utilizing the bottom zone for breeding with different numbers of cylinder rows. According to this one-dimensional estimate, Case 4 gives an overall TBR greater than 1 by a very small margin. Case 5 shows that the overall TBR can be made greater than the required value of 1.05 by using a layer of a neutron multiplier (80% Be, 10% Fe 1422 and 10% H_2O) behind the first wall in the upper and lower inboard zones. Using lead instead of beryllium yields a slightly lower TBR as given for Case 6. Cases 4, 5 and 6 are considered further in this study. The final design presented in Section 5.2.2 indicates that L-shaped cylinders are used in the bottom blanket zone with four rows in the horizontal section and only two rows in the vertical section as required for adequate magnet protection. This design is properly represented in Cases 4, 5 and 6 where three rows of cylinders are assumed to be used in the bottom blanket zone. The effect of using a front neutron multiplier layer in the upper and lower inboard zones on the TF coil radiation effects will be investigated in Chapter 7.

Because of the approximations used in estimating the overall TBR given in Table 5.3-4, detailed three-dimensional neutronics calculations for Cases 4, 5 and 6 are presented in the following section.

5.3.5 Three-Dimensional Analysis

The three-dimensional calculations have been performed using the continuous energy coupled neutron-gamma Monte Carlo code MCNP[7] and cross section data based on the ENDF/B-V evaluation. Because of symmetry only 1/24 of the reactor was modeled with two reflecting surfaces surrounding it. The

Table 5.3-4 Overall TBR Estimate

	Upper Inboard Segment	Bean Coil Zone	Lower Inboard Segment	Top Blanket	Bottom Blanket	Outboard Blanket	Space Between Modules	Overall TBR
Case 1	SS	W	SS	7 rows	SS	7 rows	SS	0.901
Case 2	SS	W	SS	7 rows	1 row	7 rows	SS	0.939
Case 3	SS	W	SS	7 rows	2 rows	7 rows	SS	0.974
Case 4	SS	W	SS	7 rows	3 rows	7 rows	SS	1.002
Case 5	Be	W	Be	7 rows	3 rows	7 rows	SS	1.129
Case 6	Pb	W	Pb	7 rows	3 rows	7 rows	SS	1.089

model includes one-half of one of the twelve blanket modules. The vertical cross section of the geometrical model used in the calculations is given in Fig. 5.3-8. A horizontal cross section at the reactor midplane is shown in Fig. 5.3-9. Horizontal cross sections at locations Z = 150, 90, -130 and -180 cm are given in Figs. 5.3-10, 11, 12 and 13, respectively. An average breeding blanket composition of 69.3% LiPb, 22.2% void and 8.5% HT-9 was used in the breeding blanket zones. The 1 cm thick first wall contains 30% HT-9. The inboard shield consists of 80% W (0.95 density factor), 10% Fe 1422 and 10% H_2O. The normal bean coil is assumed to have 63% Cu, 25% MgO and 12% H_2O. The reflector/shield used behind the breeding blanket consists of 90% Fe 1422 and 10% H_2O. Three different materials are considered in the 10 cm thick layer behind the first wall in the upper and lower inboard zones. In the first option, the same composition as the reflector/shield is used. In the second option, 80% Be, 10% Fe 1422 and 10% H_2O is used. In the third option the beryllium is replaced by lead.

The neutron source was sampled from a D-shaped plasma zone whose boundary is given by the parametric equations

$$Z = a_0 \kappa \sin t \tag{1}$$

and

$$R = R_0 + a_0 \cos(t + 0.3 \sin t) \ . \tag{2}$$

The parameter t varies from 0 to π. The plasma major radius R_0, the plasma minor radius a_0, and the elongation κ were taken to be 2.6 m, 0.6 m and 1.6, respectively. At the midplane the scrapeoff zones are 6 cm and 10 cm thick on

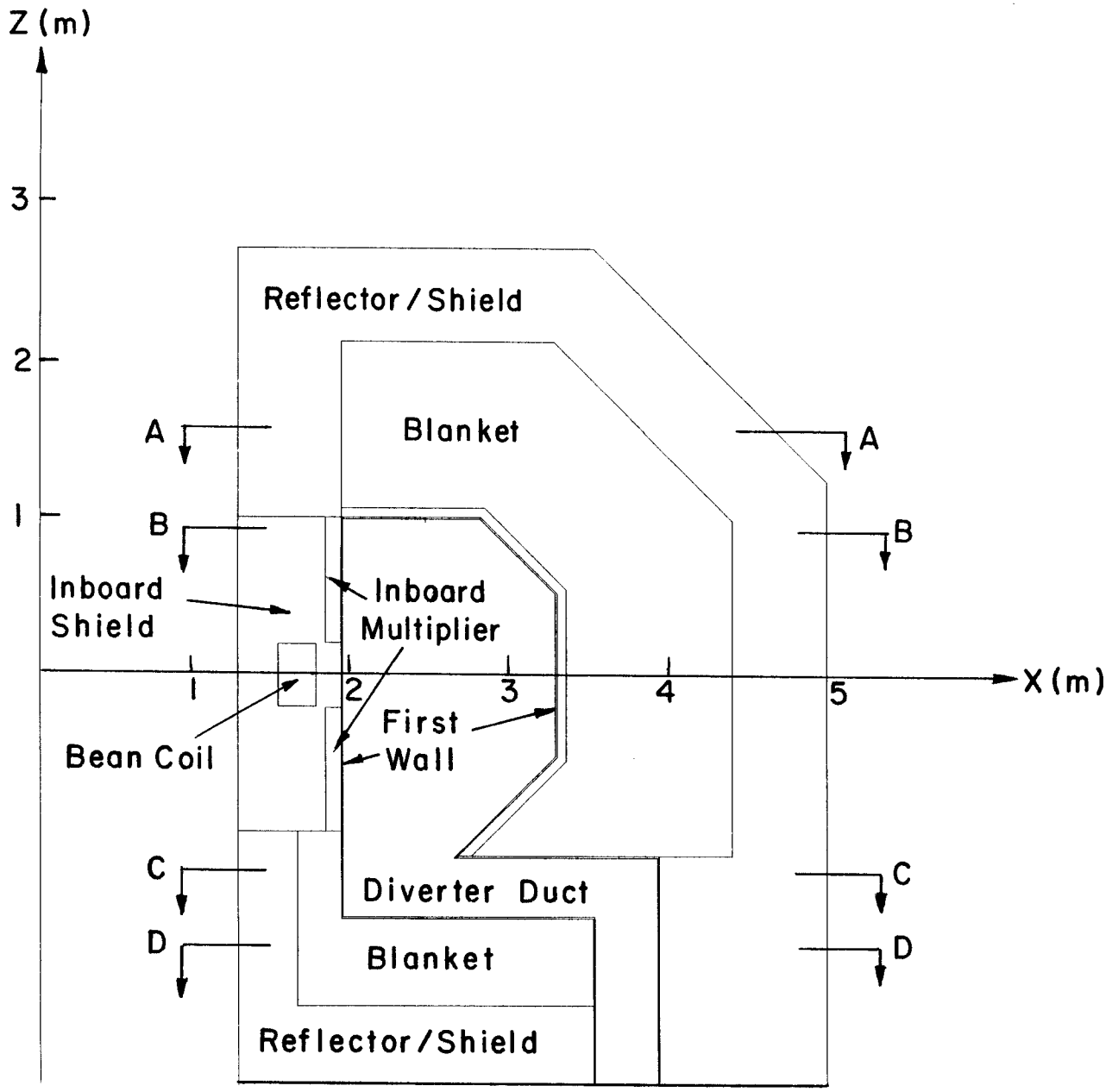

Fig. 5.3-8 Vertical cross section of the HWL geometrical model used in the three-dimensional calculations.

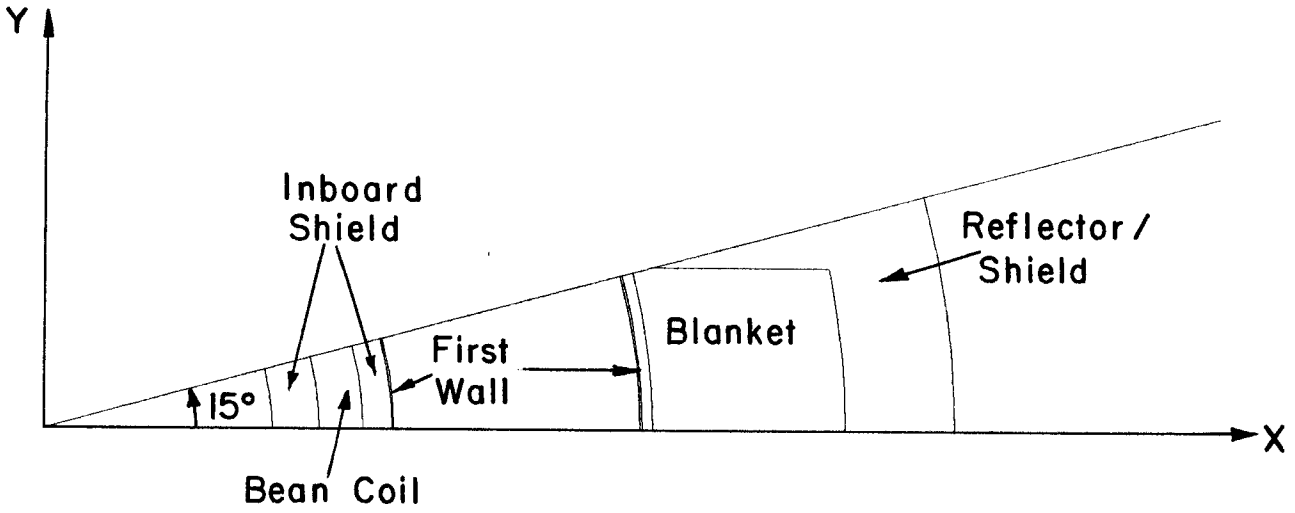

Fig. 5.3-9 Horizontal cross section at the reactor midplane.

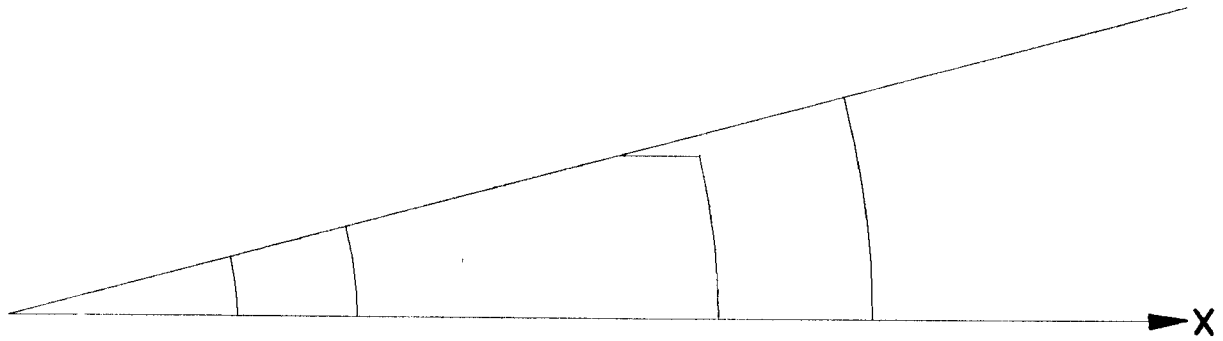

Fig. 5.3-10 Section A-A of the geometrical model.

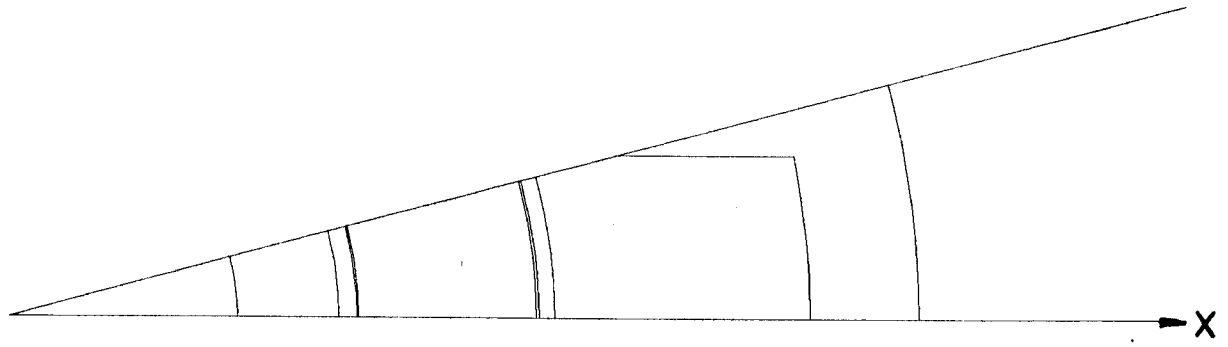

Fig. 5.3-11 Section B-B of the geometrical model.

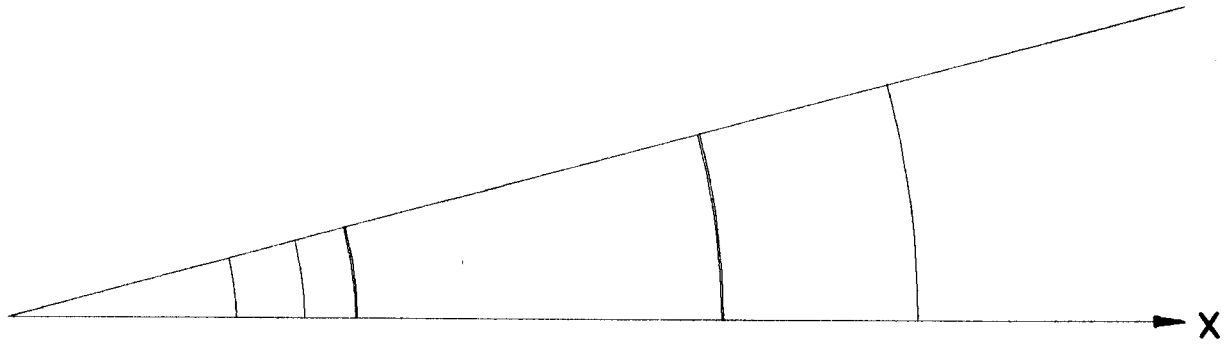

Fig. 5.3-12 Section C-C of the geometrical model.

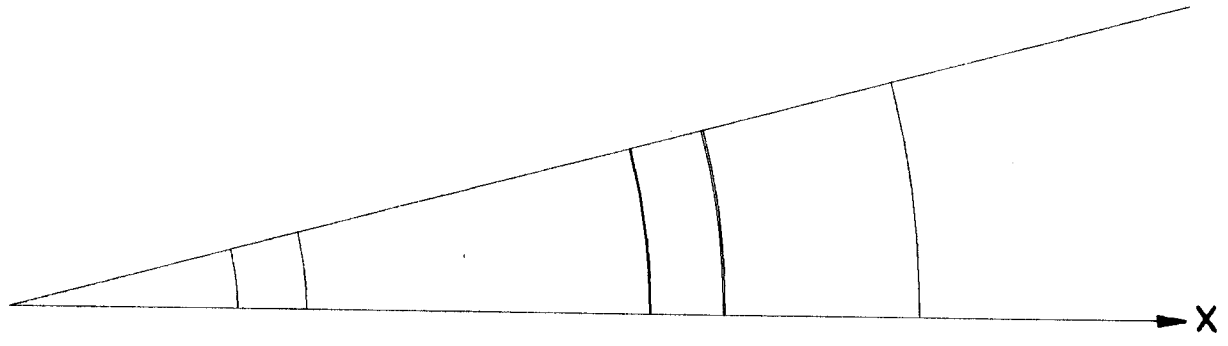

Fig. 5.3-13 Section D-D of the geometrical model.

the inboard and outboard sides, respectively. The location of the neutron source was determined by sampling from the spatial source distribution

$$S(r,z) = S_o[1 - (r/r_m)^2]^2 \qquad (3)$$

where r is the distance between the source point and the magnetic axis (R = 2.7 m and Z = 0) and r_m is the distance measured from the magnetic axis to the plasma boundary passing through the source point.

Five thousand histories were used in the Monte Carlo calculations yielding statistical uncertainties less than 1% in the calculated overall TBR and energy multiplication. The overall TBR and energy multiplication for the three design options are given in Table 5.3-5. It is interesting to note that the results for the TBR agree to within ~ 4% with the preliminary estimate based on the one-dimensional analysis. It is clear that the first design option does not meet the requirement of a TBR $\tilde{>}$ 1.05 and a neutron multiplier should be used on the inboard side above and below the bean coil. Both design options with Be and Pb are considered in the HWL design. The main concerns with using beryllium are the irradiation swelling and the resource limitations. On the other hand, the volume change of lead upon phase change should be taken into consideration.

Table 5.3-6 gives the tritium production in the different blanket zones. The contributions from the $^6Li(n,\alpha)t$ and $^7Li(n,n'\alpha)t$ reactions are also given. The results are provided for both design options. About 19% of the tritium breeding occurs in the bottom blanket. Almost all the tritium is produced in the $^6Li(n,\alpha)t$ reaction.

Table 5.3-5. Overall TBR and Energy Multiplication for the Three Design Options

Front Layer of Upper and Lower Inboard Zones	TBR	M
SS	1.012 (± 0.9%)	1.308 (± 0.6%)
Be	1.085 (± 0.9%)	1.336 (± 0.6%)
Pb	1.066 (± 0.9%)	1.307 (± 0.6%)

Table 5.3-6. Tritium Production (Tritons/Fusion) in the Different Blanket Zones

Front Layer of Upper and Lower Inboard Zones	Be	Pb
Top and Outboard Blanket		
T_6	0.882 [0.012][a]	0.865 [0.011]
T_7	1.62(-3)[b] [0.019]	1.59(-3) [0.019]
Total	0.884 [0.011]	0.867 [0.010]
Bottom Blanket		
T_6	0.201 [0.026]	0.199 [0.026]
T_7	2.98(-4) [0.053]	2.96(-4) [0.053]
Total	0.201 [0.025]	0.199 [0.025]
System Total		
T_6	1.083 [0.01]	1.064 [0.009]
T_7	0.002 [0.017]	0.002 [0.017]
Total	1.085 [0.009]	1.066 [0.009]

a) Fractional Standard Deviation

b) Reads 1.62×10^{-3}

The nuclear heating results for the two design options are given in Tables 5.3-7 and 5.3-8. About 55% of the total nuclear heating comes from gamma heating. This is a direct consequence of using a metallic reflector. Based on a reactor fusion power of 1025 MW, we calculated the thermal power resulting from nuclear heating in the different reactor zones. The results are given in Table 5.3-9 for the two design options. About 33% of the total nuclear heating is deposited in the water cooled zones. Assuming that the energy carried by the α particles emitted in the fusion reaction will be recovered by the cooling systems of the divertor plates and first wall, the total reactor thermal power is 1300.76 MW for the Be case and 1276.71 MW for the Pb case. Assuming a 70% divertor efficiency and that the divertor is water cooled we determined that ~ 38% of the total reactor thermal power will be carried by the water coolant. This power can be used as a part of the power cycle. These results are useful for designing the power cycle and determining the thermal efficiency.

5.3.5 Summary

The poloidal variation of the neutron wall loading in the HWL design was determined. The average wall loading is 8.68 MW/m^2 and the peak value occurring at the reactor midplane on the outboard side is 12 MW/m^2. The impact on the overall TBR of using different inboard materials was investigated. Using neutron multipliers gives the largest overall TBR. One-dimensional calculations were performed to determine the effect of the number of blanket cylinder rows on the local TBR and energy multiplication. A 1.06 m thick blanket consisting of eight rows of cylinders yields a local TBR of 1.5 and an energy multiplication of 1.19.

Table 5.3-7. Nuclear Heating (MeV/Fusion) with Beryllium on the Inboard Side

	Neutron	Gamma	Total
First Wall			
Top and outboard	0.073	0.096	0.169
Inboard and bottom	0.041	0.073	0.114
Divertor duct	0.005	0.019	0.024
Total	0.119	0.188	0.307
Blanket			
Top and outboard	5.896	4.259	10.155
Bottom	1.290	0.891	2.181
Total	7.186	5.150	12.336
Reflector/Shield			
Inboard multiplier	0.851	0.313	1.164
Inboard shield	0.158	2.609	2.767
Top and outboard	0.152	1.450	1.602
Bottom	0.040	0.546	0.586
Total	1.201	4.918	6.119
Normal Bean Coil	0.011	0.062	0.073
Total System	8.517	10.318	18.835

Table 5.3-8. Nuclear Heating (MeV/Fusion) with Lead on the Inboard Side

	Neutron	Gamma	Total
First Wall			
Top and outboard	0.073	0.085	0.158
Inboard and bottom	0.041	0.052	0.093
Divertor duct	0.005	0.020	0.025
Total	0.119	0.157	0.276
Blanket			
Top and outboard	5.842	4.126	9.968
Bottom	1.288	0.867	2.155
Total	7.130	4.993	12.123
Reflector/Shield			
Inboard multiplier	0.315	0.777	1.092
Inboard shield	0.167	2.380	2.547
Top and outboard	0.157	1.558	1.715
Bottom	0.042	0.550	0.592
Total	0.681	5.265	5.946
Normal Bean Coil	0.011	0.066	0.077
Total System	7.941	10.481	18.422

Table 5.3-9. Thermal Power (MW) Resulting from Nuclear Heating in the Different Zones

Front Layer of Upper and Lower Inboard Zones	Be	Pb
First wall	17.88	16.08
Blanket	718.43	706.02
Total in helium cooled zones	736.31	722.10
Reflector/Shield	356.37	346.29
Normal bean coil	4.25	4.48
Total in water cooled zones	360.62	350.77
Total System	1096.93	1072.87

The peak power densities in the first wall and blanket are 72 and 87 W/cm^3, respectively. The average power densities in the front row of cylinders of the top and outboard blankets are 24 and 47 W/cm^3, respectively. The overall TBR in the HWL reactor was estimated based on the one-dimensional results using different inboard materials and different bottom blanket thicknesses. An overall TBR > 1.05 was obtained when a 10 cm layer of a neutron multiplier is used on the inboard side above and below the bean coil.

These results were confirmed by the detailed three-dimensional calculations where the overall TBR was found to be 1.085 and 1.066 for the beryllium and lead cases, respectively. The energy multiplication values are 1.336 and 1.307 for the Be and Pb cases, respectively. Based on a reactor fusion power of 1025 MW, the total reactor thermal power was found to be ~ 1300 MW. About 38% of this power is carried by the water coolant of the reflector/shield and the divertor plates and can be considered as a part of the power cycle. We conclude from the neutronics analysis that the HWL blanket design is capable of achieving an overall TBR > 1.05.

References for Section 5.3

1. J. Jung and M. Abdou, Nucl. Tech./Fusion, 4, 361 (1983).

2. Y. Gohar, Trans. Am. Nucl. Soc., 44, 140 (1983).

3. M. Abdou et al., "Blanket Comparison and Selection Study", ANL/FPP-83-1, Argonne National Lab. (1983).

4. B. Micklich and D. Jassby, Trans. Am. Nucl. Soc., 44 144 (1983).

5. R. O'Dell et al., "User's Manual for ONEDANT: A Code Package for One-Dimensional, Diffusion-Accelerated, Neutral Particle Transport", LA-9184-M, Los Alamos National Lab. (Feb. 1982).

6. M. Sawan and J. Huang, "The Tritium Breeding-Energy Multiplication (T-M) Plot for Fusion Blanket Design", Trans. Am. Nucl. Soc., 44, 146 (1983).

7. "MCNP - A General Monte Carlo Code for Neutron and Photon Transport", LA-7396-M, Los Alamos National Lab. (1981).

5.4 Thermal-Hydraulic Analysis

Given this unique design for the blanket and first wall assembly one must next verify that the temperatures within these components do not exceed design limits. In the next two sections we briefly outline the thermal analysis of the first wall and blanket.

5.4.1 First Wall Thermal Hydraulics

The first wall in the HWL reactor is a membrane-type HT-9 structure with built-in coolant channels. Typical membrane wall designs are shown in Fig. 5.4-1. A design similar to that shown in Fig. 5.4-1(b) has been developed and successfully used by Babcock and Wilcox in their modern high pressure fossil boilers.[1] Membrane walls can be easily manufactured; they have proven to be reliable, leak-free, and simple to install. The design shown in Fig. 5.4-1(a) has been selected because of its simplicity.

High pressure helium is used to cool the first wall entering at 80 atm and 275°C, and leaving at 77.5 atm and 400°C. The inlet conditions are selected to match those for the blanket coolant while the exit coolant temperature is selected so that the maximum wall temperature at the "hot spot" is limited to about 500°C. This temperature is well below the point when the yield stress for HT-9 begins to drop perceptibly with increasing temperature. Table 5.4-1 lists the main thermal hydraulic parameters for the first wall.

Figure 5.4-2 is a schematic diagram of the "unfolded" first wall in one of the twelve blanket modules of the HWL reactor. Each module contains 754 coolant channels with an inside diameter of 0.8 cm and a flow length in the poloidal direction varying between 1.02 m and 1.73 m for the inboard and outboard vertical regions, respectively. Since all the coolant channels in a given module are fed by and discharged into common headers, it is necessary to

Table 5.4-1. First Wall Thermal Hydraulic Parameters

Volumetric Heating Power, MWt	17.4
Surface Heating Rate, MWt	61.5*
Total Power Removed by FW Coolant, MWt	78.9
Heat Generation Rate, W/cc	52.0
Average Plasma-Side Surface Heat Flux, W/cm^2	55.0
Coolant Helium	
Coolant Inlet Temperature, °C	275
Coolant Exit Temperature, °C	400
Coolant Inlet Pressure, atm	80.0
Coolant Exit Pressure, atm	77.5
Coolant Flow Rate, kg/hr	4.38×10^5
Pumping Power, MWe	7.03**
Maximum Coolant Velocity, m/s	110.8
Maximum Wall Temperature, °C	506

*Based on a divertor efficiency of 70%.

**Based on a compressor efficiency of 70%.

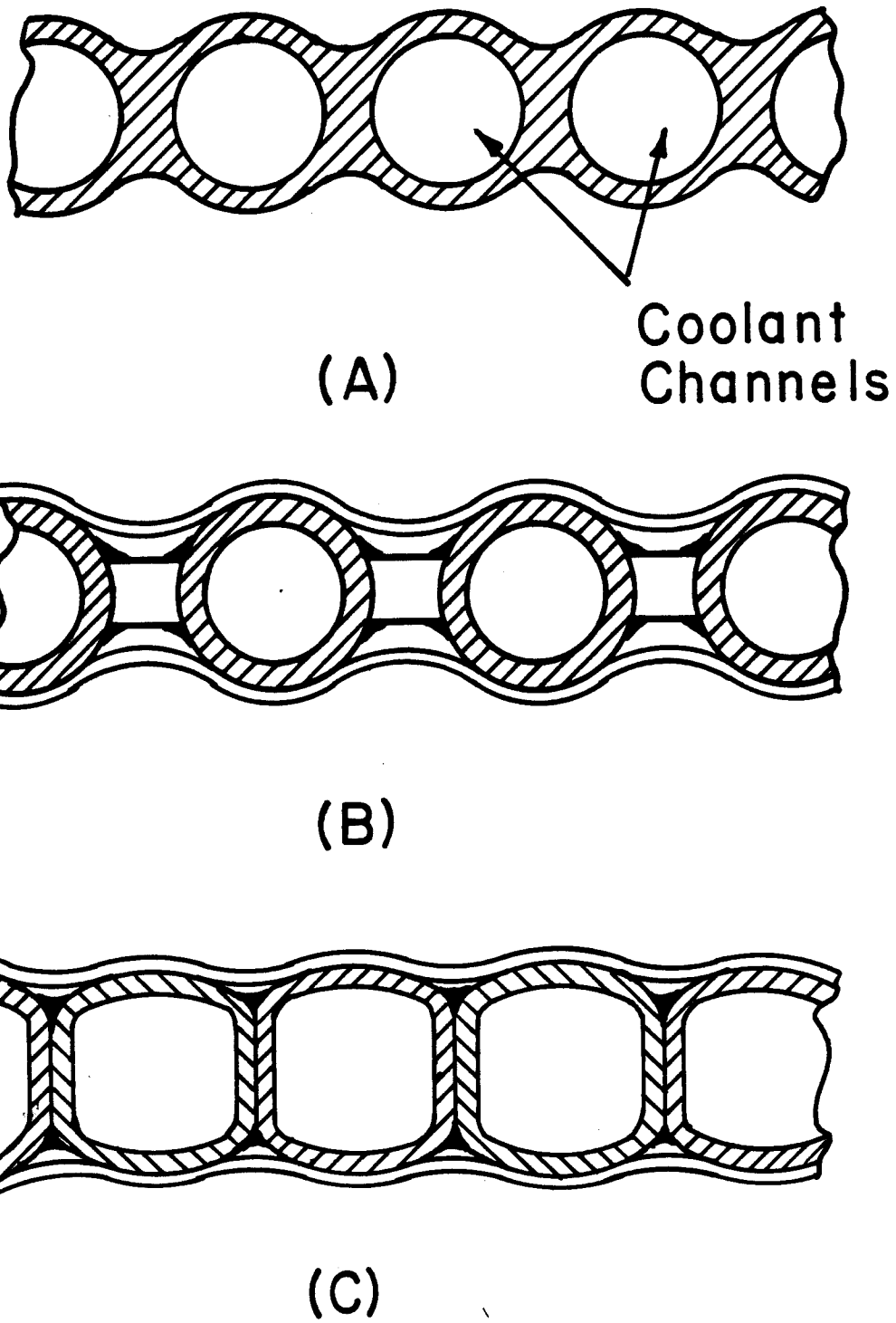

Fig. 5.4-1. Typical membrane wall designs for first wall construction.

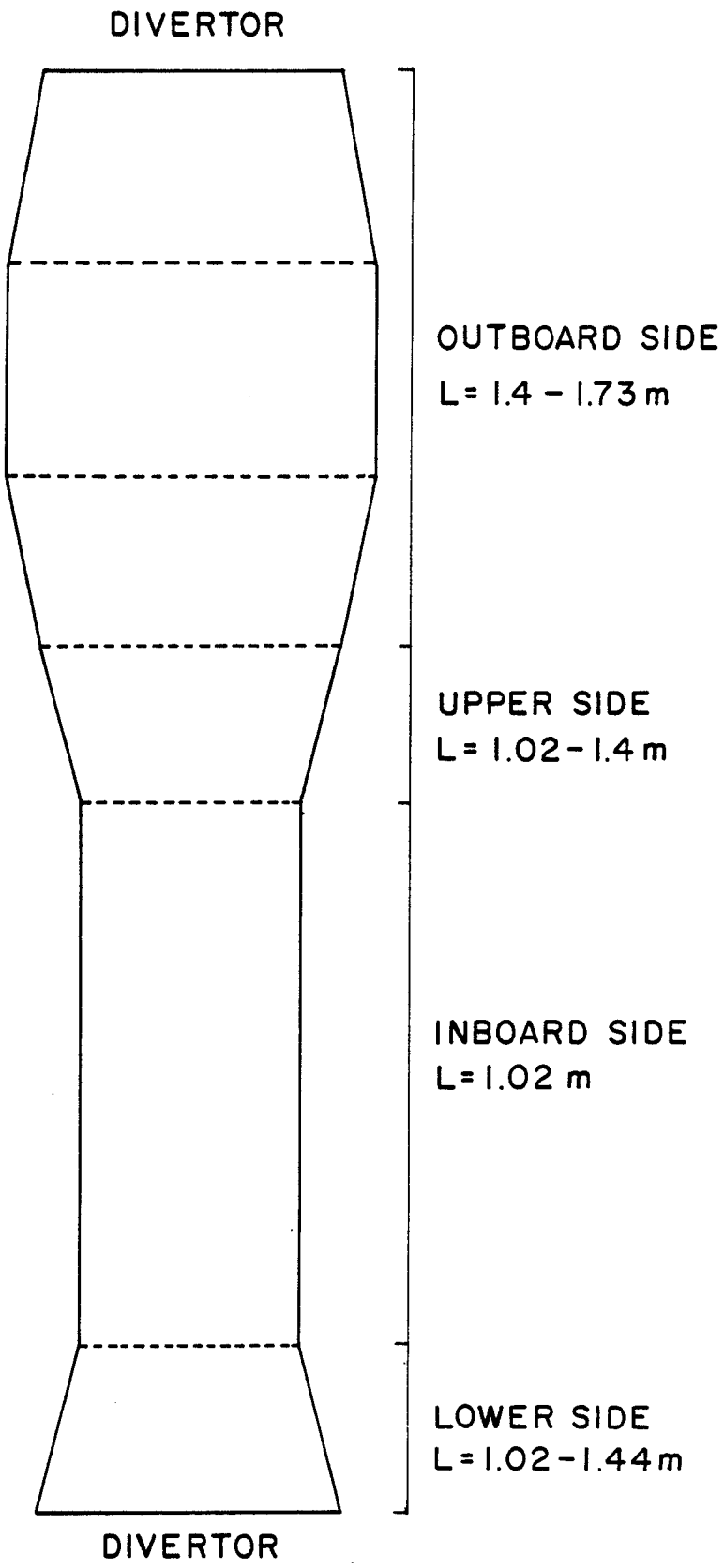

Fig. 5.4-2. Schematic diagram of an "unfolded" first wall segment.

use "orificing" at the channels' inlet, except for the longest channels in the outboard vertical region. Orificing allows the flow rate to be tailored to nearly match the power removed in each channel which is proportional to the channel length (see Fig. 5.4-3).

The coolant supply and discharge headers for the twelve wall segments are arranged so that six similar units are formed. Each unit consists of two segments connected in series; these are hereafter referred to as the "cold" and "hot" segments respectively. The helium coolant enters the supply header of the cold segment at 80 atm and 275°C. The discharge header of the cold segment is connected to the supply header of the hot segment. The helium coolant leaves the discharge header of the hot segment at 400°C and 77.5 atm and is combined with that from the other six hot segment discharge headers before being supplied to the power cycle. This arrangement allows the coolant velocity in the channels to be increased to about 100 m/s as recommended for high heat flux gas-cooled systems[2] so that reasonably high heat transfer coefficients can be obtained (see Figs. 5.4-3 and 5.4-4). The maximum coolant velocity in the hot segments varies between 90.2 m/s at the exit of inboard vertical region channels to 110.8 m/s at the exit of the outboard vertical region channels (see Fig. 5.4-3). The corresponding heat transfer coefficients are 0.722 and 0.873 W/cm^2 °K, respectively; these values are calculated using the Dittus-Boelter correlation.[3]

A two-dimensional finite-element computer code, FEM2D, has been used to determine the wall temperature distribution.[4] Because of symmetry, only one half of a channel wall has been considered; a total of 26 nodes and 24 elements has been used (see Fig. 5.4-5). Axial conduction in the flow direction and heat losses (or gains) from the outside tube surface on the blanket side

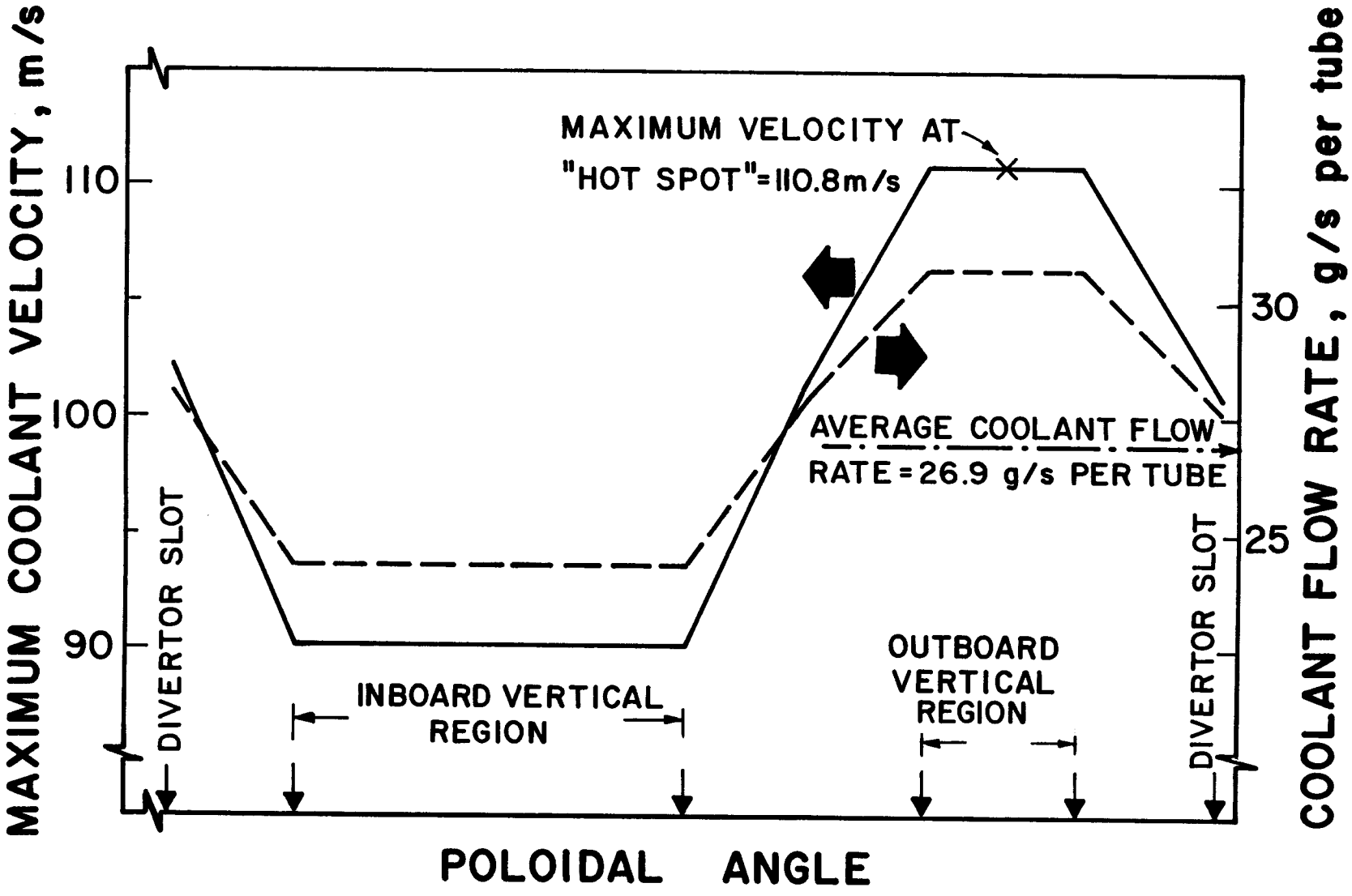

Fig. 5.4-3. Coolant flow rate and maximum coolant velocity for the different first wall channels.

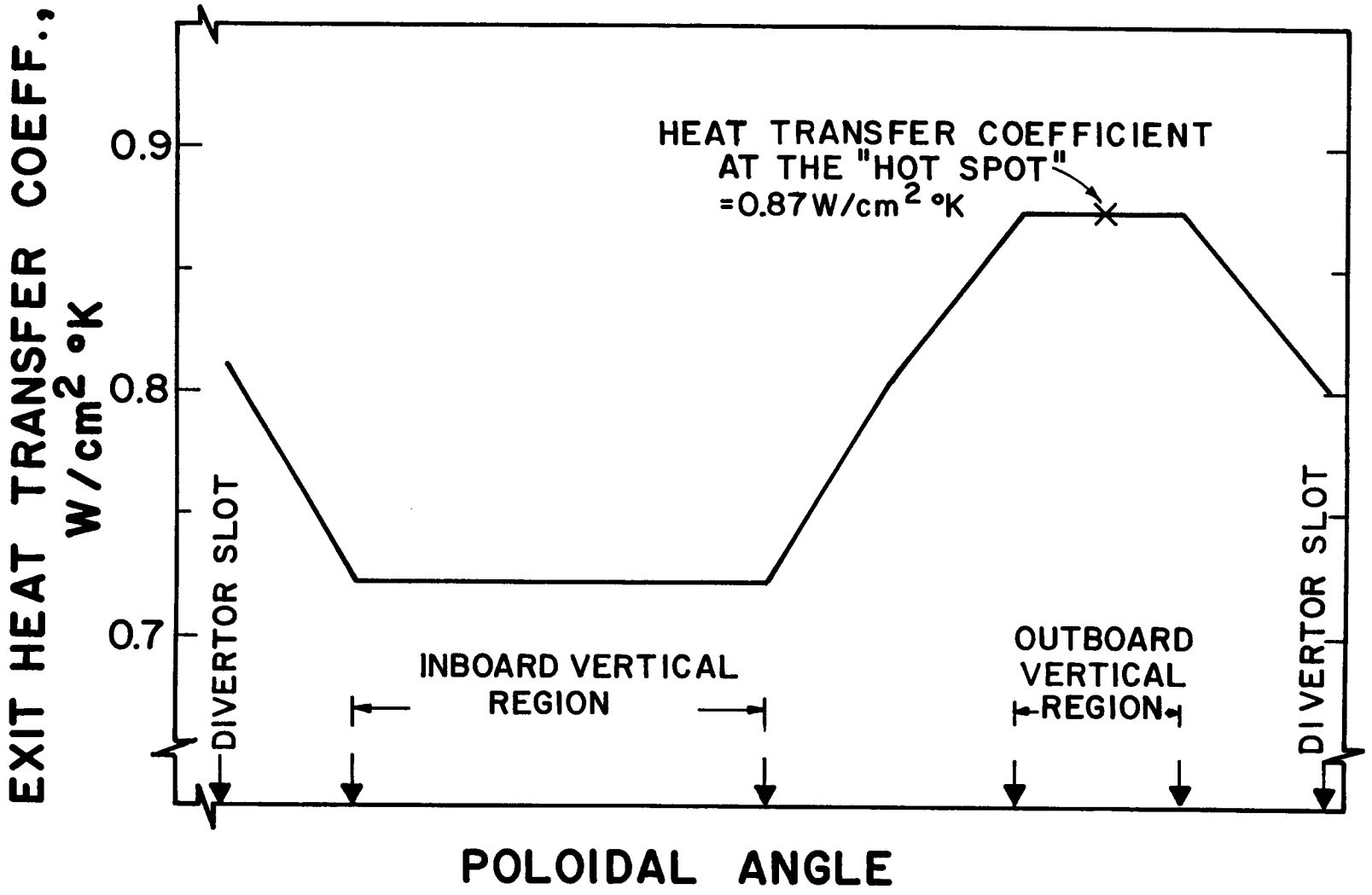

Fig. 5.4-4. Variation of the convective heat transfer coefficient at the exit of the different first wall coolant channels.

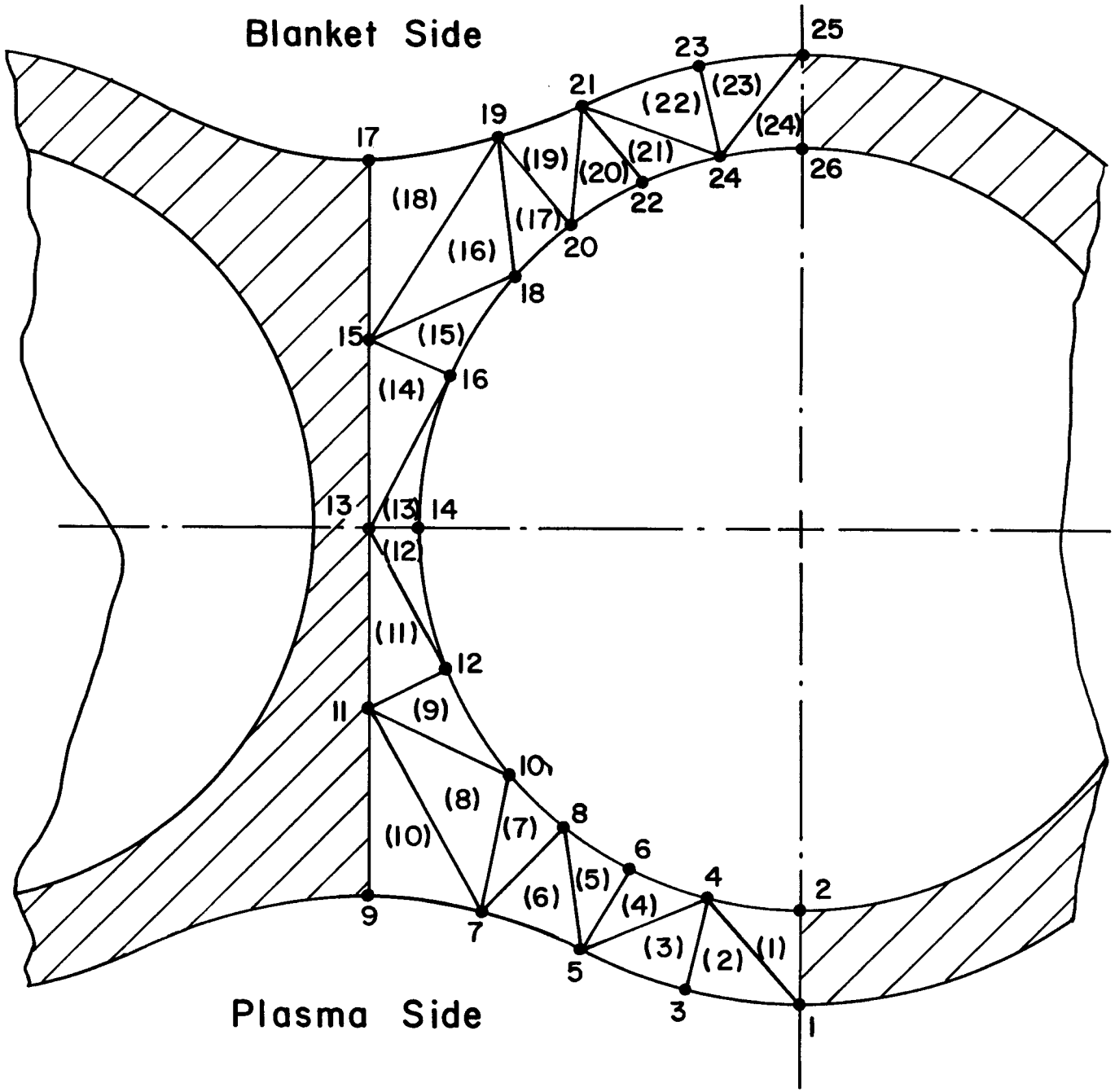

Fig. 5.4-5. Schematic diagram of the finite element mesh used to determine the first wall temperature distribution.

have been ignored. The analysis has been performed parametrically for different values of the plasma-side surface heat flux, and coolant heat transfer coefficient. A uniform value of the volumetric heat generation rate, $q''' = 52$ W/cc, has been used. For all the cases examined, the maximum wall temperature occurs at node #1 (see Fig. 5.4-5).

The results are shown in Fig. 5.4-6 where the maximum temperature difference, i.e. the difference between the wall temperature at node #1 and the local coolant temperature, is plotted for different values of the surface heat flux and local heat transfer coefficient. These results are independent of the local coolant temperature since a constant wall thermal conductivity is used.

For each coolant channel in the hot segment, upon knowledge of the total power removed and coolant flow rate (Fig. 5.4-3), an energy balance is used to determine the coolant exit temperature. Variation of the coolant exit temperature with poloidal angle is shown in Fig. 5.4-7. These results, together with the local heat transfer coefficient values shown in Fig. 5.4-4 and the parametric results in Fig. 5.4-6, are used to determine variation of the maximum wall temperature with poloidal angle at the coolant channels' exit (Fig. 5.4-7). These results show that the hottest point in the first wall will be at the exit section of the coolant channels in the outboard vertical region of each of the six hot segments. The maximum "hot spot" temperature is 506°C which is consistent with the limits stated earlier.

Figure 5.4-8 shows the temperature distribution in the first wall at the hot spot. The front surface of the wall which is subjected to the radiation heat flux from the plasma is considerably hotter than the blanket-side wall temperatures. An estimate of the thermal stresses resulting from both the

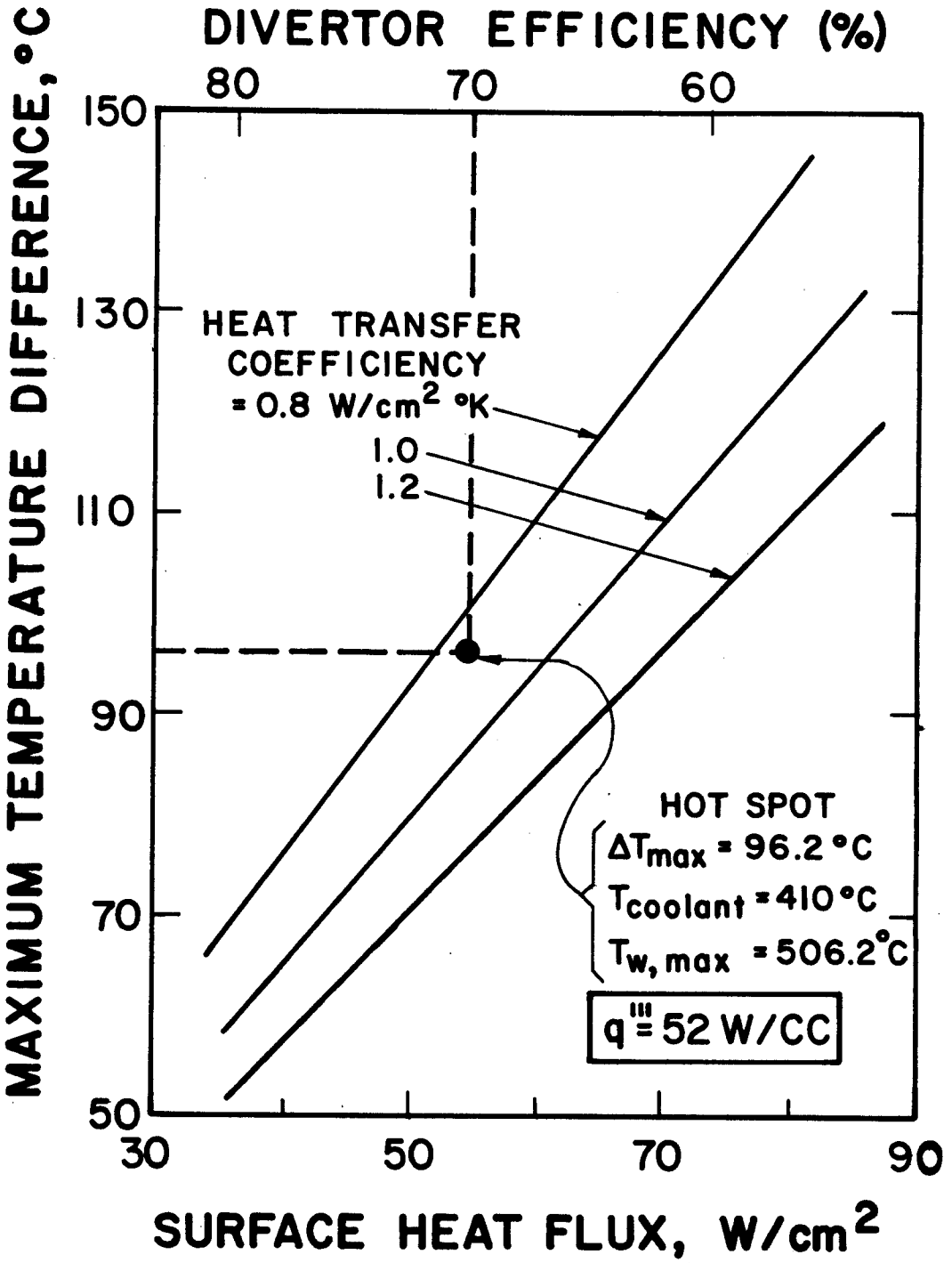

Fig. 5.4-6. Parametric results showing variation of the maximum first wall temperature rise with the surface heat flux and local heat transfer coefficient (the maximum temperature rise is defined as the difference between the maximum wall temperature and the local coolant bulk temperature).

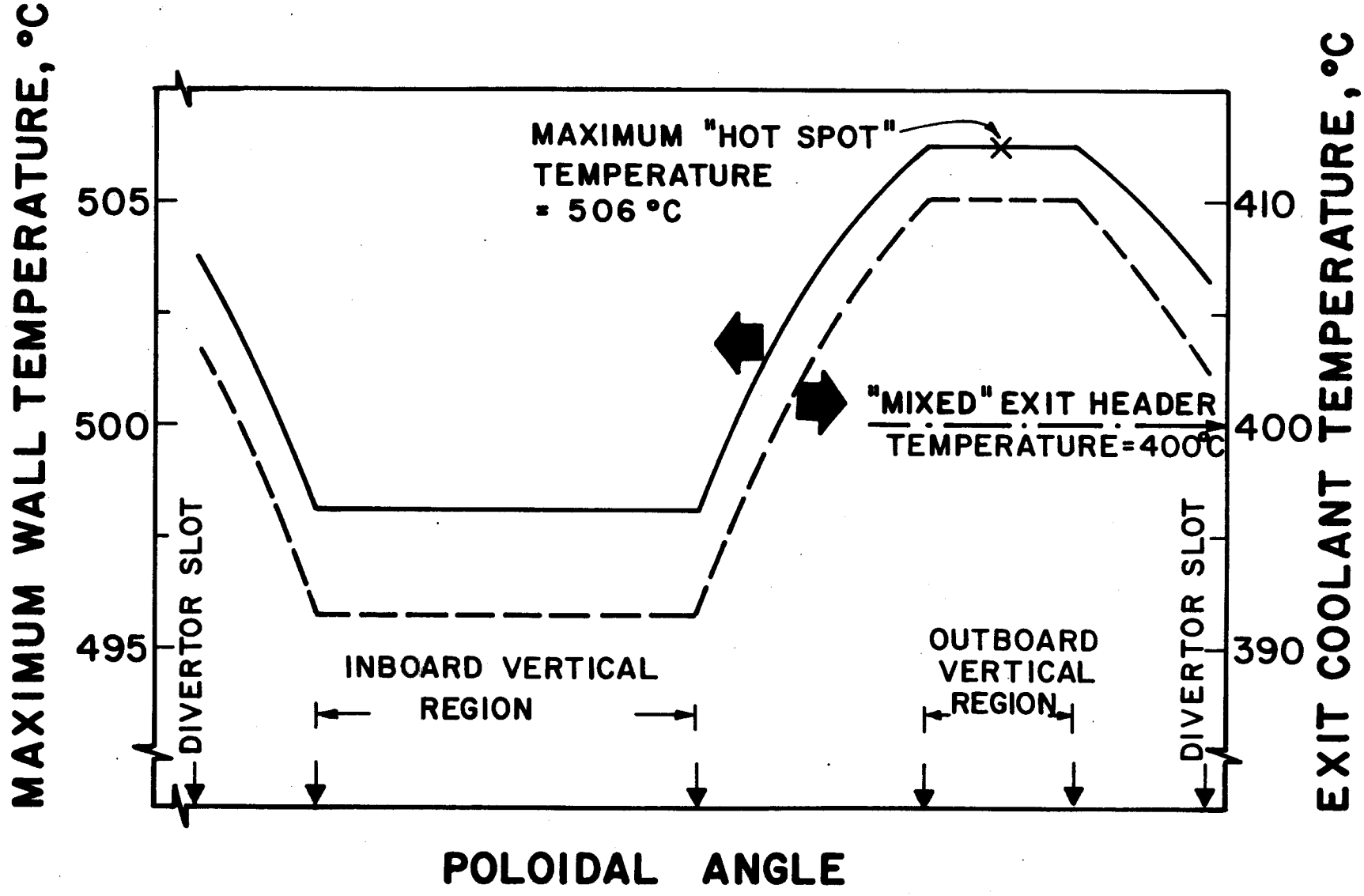

Fig. 5.4-7. Coolant exit temperature and maximum wall temperature for the different first wall coolant channels.

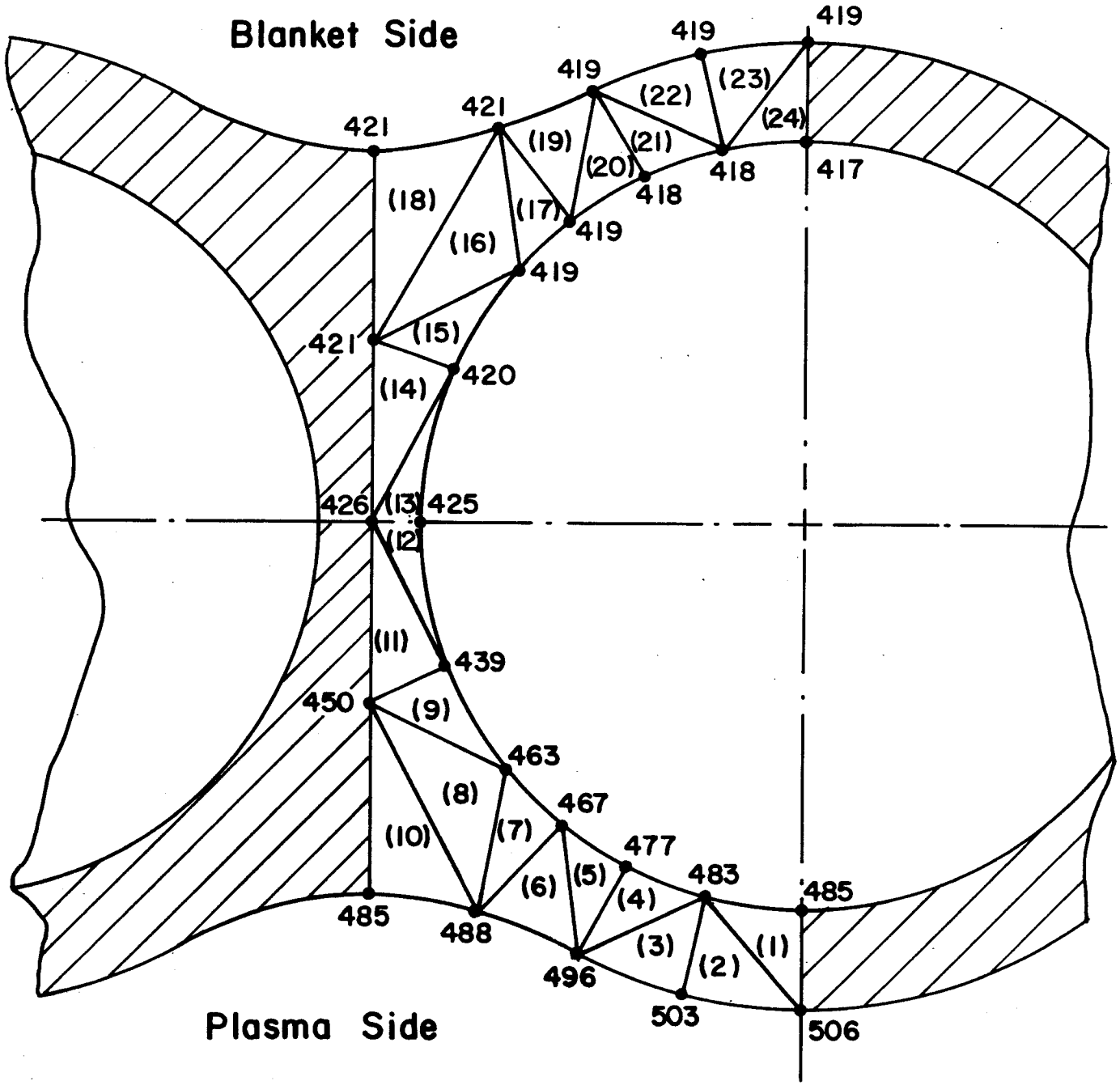

Fig. 5.4-8. First wall temperature distribution at the hot spot (located at the coolant exit section in the outboard vertical region).

radial and tangential temperature gradients shows that the stresses in the first wall will be considerably lower than the design limits.

References for Section 5.4.1

1. D.E. James and M.W. Peterson, "Suspension Type Gasifiers," Proc. of AIChE 68th Annual Mtg., Los Angeles (Nov. 1975).

2. M. Abdou et al., "Blanket Comparison and Selection Study," ANL/FPP-83-1, Argonne National Laboratory (Oct. 1983).

3. M.M. El-Wakil, Nuclear Heat Transport, pp. 243, et seq., Int. Textbook Company (1971).

4. G.E. Myers, "FEM2D - A Two-Dimensional Finite-Element Computer Program," Mechanical Engineering Department, University of Wisconsin Report (1978).

5.4.2 Blanket Thermal-Hydraulics Analysis

The major consideration one must keep in mind when evaluating a blanket design is to verify that one has minimized the work input requirements (e.g. the pumping power) while insuring that the structural design limits are maintained. The blanket module in this design employs a helium gas coolant circulating in a helical pattern around the inner surface of a closed cylinder of stagnant lithium-lead breeder. We first would like to demonstrate that the current blanket design satisfies the structural design limits and then briefly discuss the pumping power requirements.

In order to determine if the structural design limits are satisfied one must identify the region of peak energy deposition and the corresponding peak temperature. In the current tokamak design the complex geometrical arrangement of the plasma, first wall, blanket and shield causes the wall loading due to neutrons and alpha particles to have a large degree of spatial variation (see Fig. 5.3-1 in Section 5.3). In addition, the peak structural temperature will be influenced by the helium gas flow path relative to the energy wall loading near its peak value ($\sim 12\ MW/m^2$). Now to evaluate the location of the peak structural temperature (i.e., an approximate "hot spot" analysis) we have divided the analysis into three parts:

a) determination of the blanket cylinder experiencing the peak energy wall loading;

b) determination of the maximum coolant temperature near the cylinder structural wall; and

c) determination of the maximum structure temperature at this location due to the local heat flux from the structural wall.

Based on the detailed plasma and neutronic analyses, the peak wall loading would occur on the outboard side of the plasma chamber. Therefore, the first vertical ("boomerang" shaped) blanket cylinder receives the largest energy flux (Fig. 5.4-9) with an average value of 11 MW/m^2. The key energy deposition parameters for this maximum power cylinder are given in Table 5.4-2.

To determine the maximum structural temperature in this "worst case" cylinder one must determine the bulk coolant temperature profile within the cylinder. Because the helium gas circulates in a helical motion in the coolant tubes, which are in contact with the structural wall (Fig. 5.4-10), it is the coolant bulk temperature which will determine the temperature level at the "hot spot" location of the cylinder. We write a steady state, one-dimensional energy balance for the helium coolant and the lithium-lead cylinder along its length neglecting axial conduction and natural convection effects due to MHD suppression. This lumped parameter approach is conservative in that it will predict slightly higher axial temperature gradients in the coolant and breeder. The resultant energy equations are (Fig. 5.4-11)

$$\dot{m}_H c_H \frac{dT_{co}}{dx} = h_o P_o (T_f - T_{co}) \tag{1}$$

for the gas coolant flow into the cylinder,

$$-\dot{m}_H c_H \frac{dT_{ci}}{dx} = h_i P_i (T_f - T_{ci}) \tag{2}$$

for the gas coolant flow out of the cylinder, and

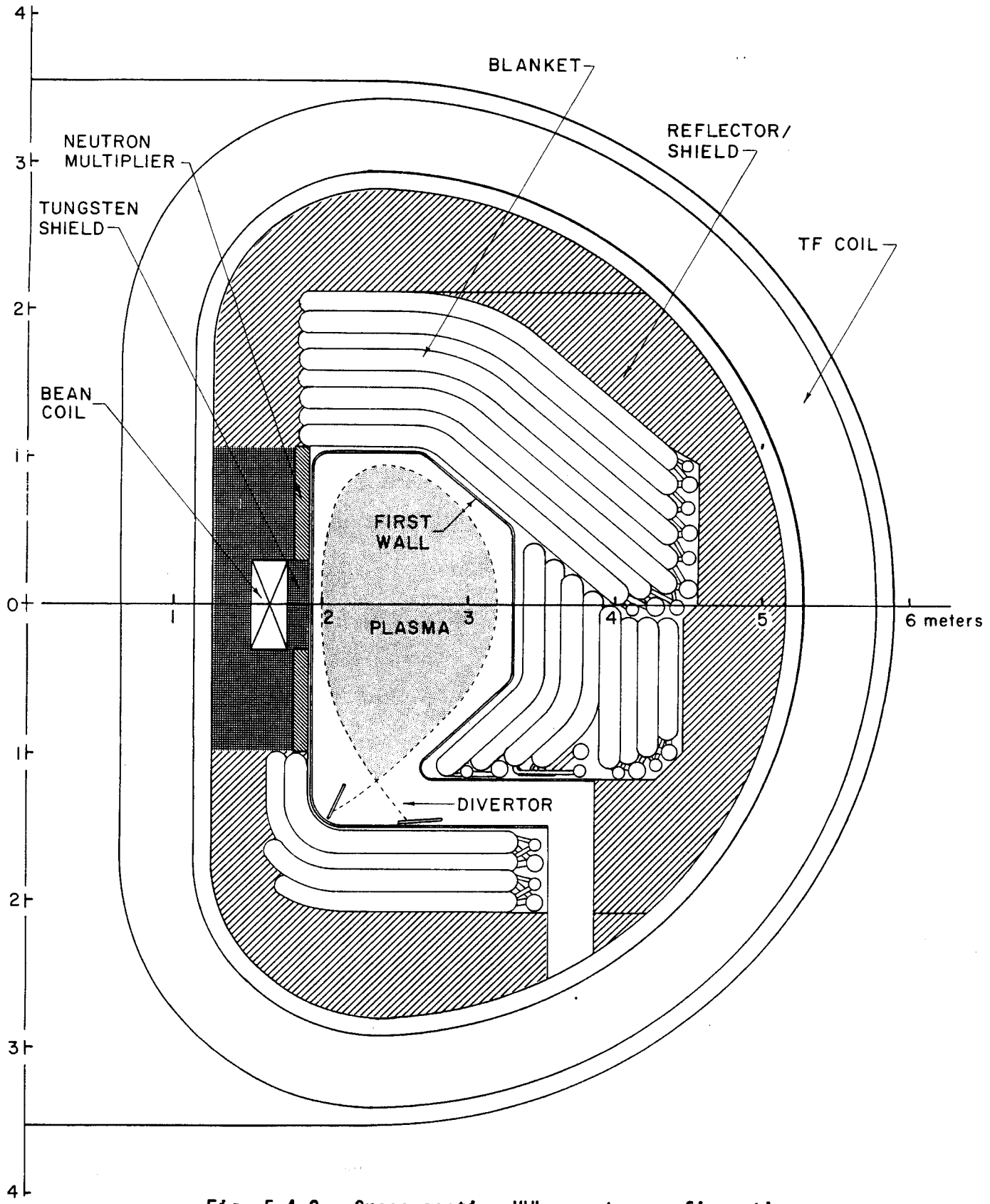

Fig. 5.4-9. Cross section HWL reactor configuration.

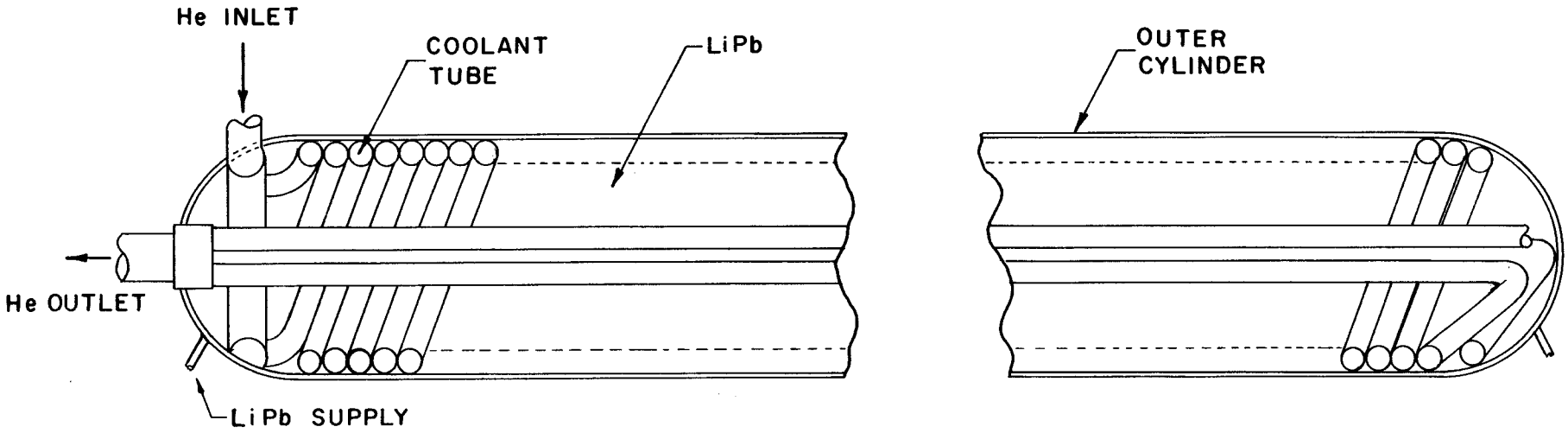

Fig. 5.4-10. Blanket cylinder cross section.

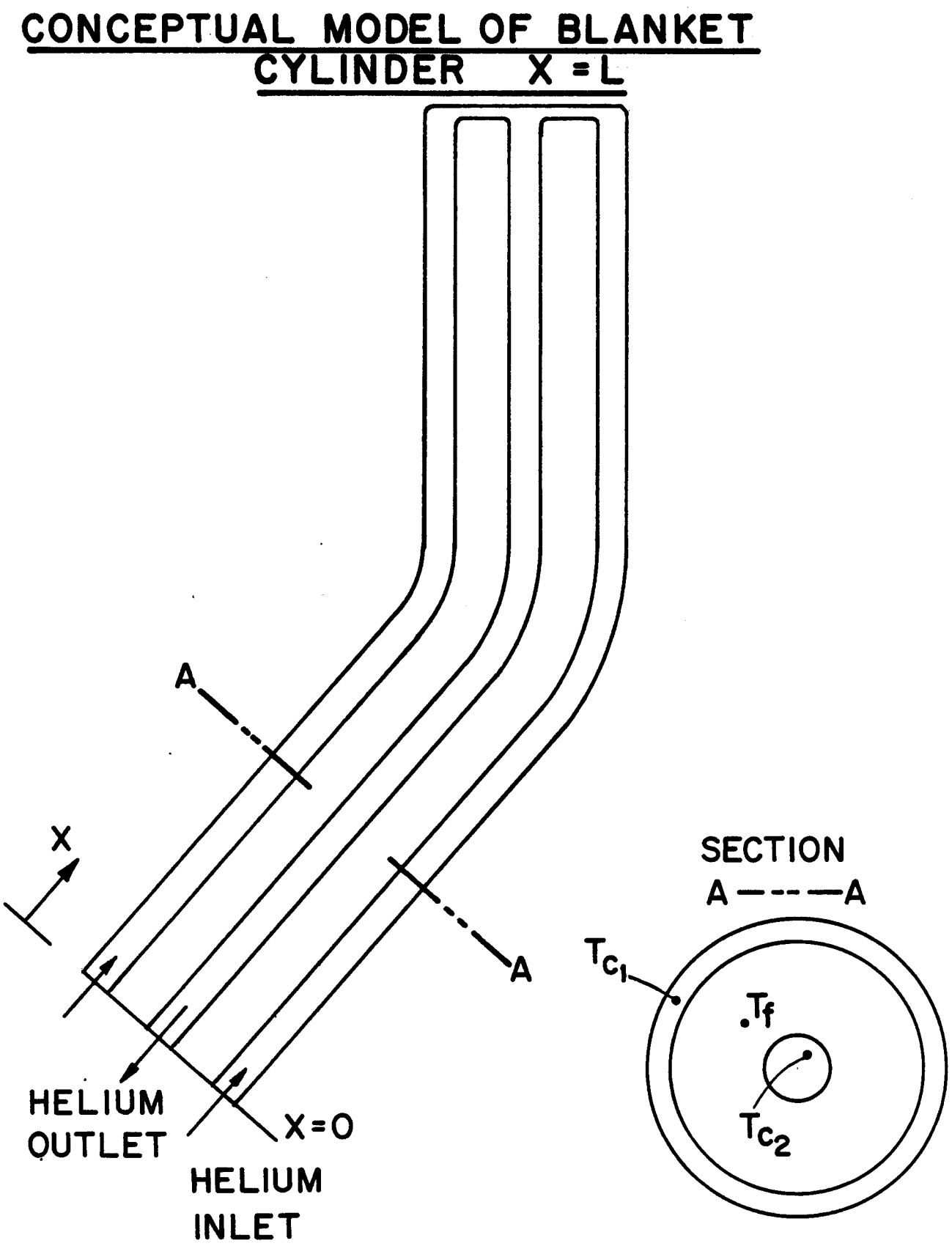

Fig. 5.4-11. Conceptual model of blanket cylinder.

Table 5.4-2. Blanket Energy Deposition Parameters for Maximum Power Cylinder

Peak power density	87 w/cc
Average power density	47 w/cc
Average linear power	5.56 kw/cm
Total power	0.97 MW

Table 5.4-3. Blanket Coolant Flow Parameters

Inlet bulk helium temperature	275°C
Inlet helium pressure	80 atm
Inlet helium velocity	68 m/s
Maximum helium velocity	96 m/s
Maximum mach no.	0.06
Outlet bulk helium temperature	500°C
Outer heated perimeter (P_o)	115 cm
Inner heated perimeter (P_i)	39 cm

Table 5.4-4. Estimated "Hot Spot" Temperatures

Maximum bulk helium temperature	525°C
Maximum structural surface temperature	535°C

$$\dot{m}_H c_H \left(\frac{dT_{co}}{dx} - \frac{dT_{ci}}{dx}\right) = q' \tag{3}$$

for the lithium-lead cylinder; where $\dot{m}_H$ is the helium mass flow rate, c_H is the helium specific heat, P is the heated perimeter of the inner, i, and outer, o, tubes; h is the total heat transfer coefficient, T is the temperature of the breeder, f, and the coolant, c; and q' is the average linear power. Now the steady-state boundary conditions are

$$x = 0,\ T_{co} = T_{inlet} = 275°C \tag{4}$$

$$x = L,\ T_{co} = T_{ci}|_L\ . \tag{5}$$

The solution to this set of simultaneous coupled ordinary differential equations is

$$T_{co}(x) = T_{inlet} + \frac{q'}{\dot{m}_H c_H \left(1 + \frac{h_i P_i}{h_o P_o}\right)} \left[\left(x + \frac{h_i P_i L}{\dot{m}_H c_H}\right) x - \frac{h_i P_i x^2}{2\dot{m}_H c_H}\right] \tag{6}$$

$$T_{ci}(x) = T_{co}(x) - \frac{q'}{\dot{m}_H c_H}(x - L) \tag{7}$$

and

$$T_f(x) = T_{co}(x) + \frac{q'}{(h_o P_o + h_i P_i)} \left[1 - \frac{h_i P_i}{\dot{m}_H c_H}(x - L)\right]\ . \tag{8}$$

One should notice that the temperature distributions of the fluids are approximately linear (Fig. 5.4-12) with a slight curvature due to the nonlinear nature of heating and cooling of the breeder liquid in some regions. The maximum coolant temperature occurs at the closed end of the cylinder and has a value of 525°C for our current design.

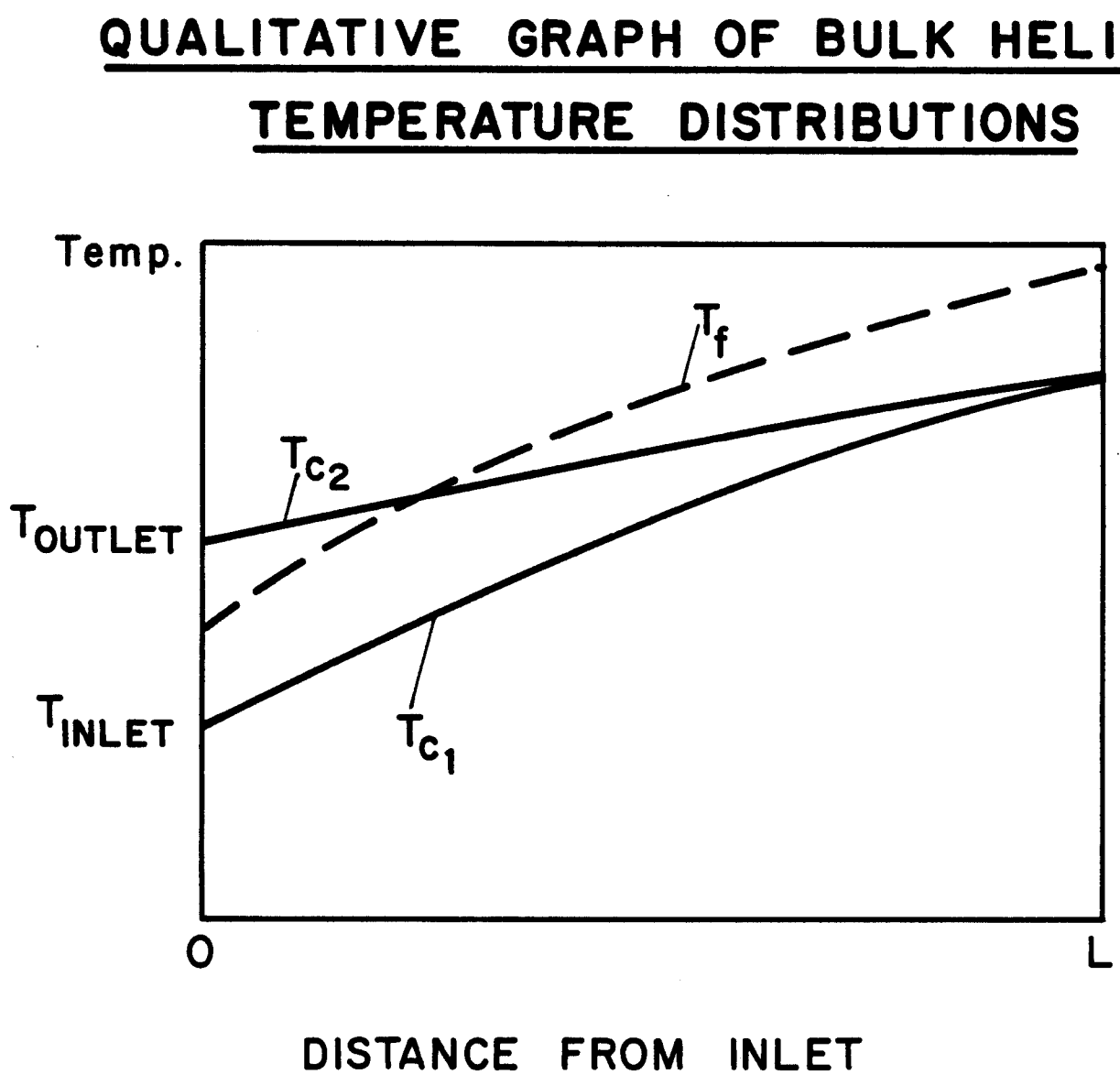

Fig. 5.4-12. Qualitative graph of bulk temperature distributions.

Because the coolant temperature rise is nearly linear and the rate of decrease of the neutron wall loading on this "worst case" cylinder (as one moves away from the horizontal plane of the plasma chamber toward the cylinder closed end) is nearly linear in this region, the peak structural temperature would occur at a location near the closed end of the cylinder at the surface of the outer HT-9 steel wall; an estimated 10-12 cm from the closed end of the tube. Now the temperature rise to the peak structural temperature can be easily calculated if one assumes the structural wall outer surface is an adiabatic boundary. This is again a conservative assumption because in actuality the wall will be at a higher temperature than the backside of the first wall and will radiate to it, cooling the surface to some extent. Under this assumption the temperature rise to the peak structural temperature is due to the volumetric nuclear heating which occurs in the cylinder and coolant tube wall (~ 39 W/cc) and the transfer of this energy across the film temperature drop in the coolant. This results in a peak structural temperature of 535°C which is within the structural design limit for the stagnant lithium-lead cylinder operating at near atmospheric pressure.

The final consideration for the blanket design is an estimate of the pressure drop. Given the sizing of the helium gas coolant tubes it is reasonable to assume that the dominant pressure drop and therefore pumping power requirements would occur in the blanket cylinders and their inlet and outlet headers. Our estimate for this pumping power is in the range of 25-50 MW, depending upon the efficiency of the helium circulator and the total length of the coolant tube length between inlet and outlet headers.

5.5 Tritium Inventory and Extraction

5.5.1 Blanket

The liquid metal alloy $Li_{17}Pb_{83}$ was selected as the breeder material over a solid ceramic breeder for several reasons, namely;

- the liquid metal alloy has a low tritium solubility,
- the liquid metal will distribute the heat more homogeneously in the blanket,
- the high neutron flux in this compact reactor will not cause detrimental radiation damage in the liquid metal as it would in a solid breeder.

Once the liquid metal alloy had been selected as the breeder material with flowing helium as the primary heat transfer fluid, the choices for tritium extraction from the breeder were either circulation of the liquid alloy to an external tritium extraction system, or in-situ removal of the tritium. The option of static containment of the alloy within the blanket cylinders with tritium extraction by permeation through the steel (HT-9) tubes was selected because,

a) the need for additional liquid metal plumbing fixtures within the compact reactor blanket was alleviated,

b) the corrosion of ferritic alloys by this liquid alloy in a flowing system with a temperature differential begins to approach an unacceptable amount as the temperature approaches 500°C,

c) the MHD losses due to flowing liquid metal in the magnetic field are eliminated.

5.5.1.1 Tritium Inventory

Based upon the option selected for tritium removal, i.e., permeation of tritium through the blanket cylinders into either the helium coolant or the

plasma chamber, an estimate of the tritium partial pressure in the blanket cylinders and the total tritium inventory in the breeder can be calculated. At steady-state the permeation of tritium from the blanket will equal the rate, $\dot{T}$, at which tritium is bred in the blanket. For the reactor operating at a nominal fusion power of 1000 MW and a tritium breeding ratio of ~ 1.1, $\dot{T}$ is approximately 28 moles T_2/d.

The permeation rate constant, ψ_{T_2}, for tritium in ferritic steel (HT-9) as a function of temperature, T, is expressed by the relationship,[1]

$$\psi_{T_2} = \frac{1.8 \times 10^3}{\sqrt{3}} \exp\left(-\frac{11{,}100}{RT}\,\frac{\text{cal}}{\text{mole}}\right) \frac{\text{mole } T_2 \cdot \text{mm}}{\text{d} \cdot \text{m}^2 \cdot \text{atm}^{1/2}}$$

where R = gas constant and T = °K. Because oxygen is used in the helium coolant to chemically combine with the tritium, an oxide coating will exist on the helium side of the coolant gas tubes. This oxide coating decreases the tritium permeation rate.[2] For this study a reduction factor of approximately 10 times is assumed.

The design of the helium coolant tubes within the blanket cylinders suggests that the coolant tubes must completely cover the inner wall of the large cylinders, particularly those cylinders closest to the plasma, in order to dissipate the high nuclear heating rate. In such a case the liquid metal breeder will not be in contact with the cylinder walls so that all the tritium permeation will be through the walls of the coolant tubes. Based upon the thickness of the wall of these tubes, their total surface area and a mean temperature of 410°C, the total tritium permeation through these tubes can be calculated, and must be equal to $\dot{T}$, i.e.,

$$Perm_{T_2} = \frac{1.1 \times 10^{-2} \text{ mol } T_2 \cdot \text{mm}}{10 \times m^2 \cdot d \cdot torr^{1/2}} \times \frac{3953 \text{ m}^2}{0.9 \text{ mm}} \times P_{T_2}^{1/2} = \dot{T} .$$

The tritium pressure, P_{T_2}, within the liquid alloy is calculated to be 33 torr (4.4 kPa). The solubility of tritium in the alloy at ~ 410°C, follows the Sievert's relationship,

$$C = K_s P_{T_2}^{1/2}$$

in which

$$K_s = 1.4 \times 10^{-2} \text{ wppm} \cdot torr^{-1/2} .$$

For the total inventory of the LiPb alloy in the blanket, 521 tonnes, the tritium inventory is 42 g.

In some of the blanket cylinders at the rear of the blanket, in which the heat generation is low, fewer coolant tubes are needed in each cylinder and some of the tritium will diffuse through the large cylinder walls. In this case, the surface areas of the tubes and the cylinders will be additive. If all the blanket cylinders followed this pattern then the partial pressure of tritium in the liquid is calculated to be 23 torr (3 kPa), slightly reduced from the previous case, and the tritium inventory is only 35 g. In either case, the tritium inventory is low, 35-42 g. Of some concern in these sealed capsules is that the tritium concentration in solution will approach saturation so that the following reaction would occur

$$Li_{17}Pb_{83(liquid)} + \frac{17}{2} T_2 = 17 \, LiT_{(solid)} + 83 \, Pb_{(liquid)} .$$

Such precipitation reactions have been studied by Valeckis[3] using the hydro-

gen titration method. He has estimated that precipitation would occur in the $Li_{17}Pb_{83}$ system at approximately 12 appmH. Based upon the Sievert's constant at 773 K (4 appmH$\cdot$kPa$^{-1/2}$), the partial pressure of H_2 required to initiate precipitation is 16 kPa (~ 120 torr). For T_2, which has a $\sqrt{3}$ greater partial pressure at the same concentration in the alloy, a partial pressure of 208 torr T_2 would be required to initiate precipitation of LiT. The previous calculations show that the T_2 pressure within the capsules should be only 16% of the limiting value; therefore, precipitation within the capsules should not occur.

5.5.2 Tritium Recovery from Helium

A process for the extraction of tritium from the helium, used as the heat transfer fluid in the first wall module and the breeder blanket, is required which can reduce the elemental, T_2, partial pressure to < 10^{-9} torr. Such a low T_2 pressure is necessary in order to maintain tritium permeation through the steam generator at an acceptable level of 10-100 Ci/d. Calculations show that all of the tritium entering the helium in the HWL breeder blanket must be removed in-situ in order to maintain the T_2 concentration < 10^{-9} torr. In the present case the tritium generation rate, $\dot{T}$, = 3.2 x 10^{-4} mole T_2/s; the He flow rate, $\dot{m}$ = 560 kg/s (1.4 x 10^5 moles He/s) and the total He pressure, P_{He} = 70 atm; based upon these parameters the mole ratio nT_2/n_{He} = 2.3 x 10^{-9} per pass of the He. The total P_{T_2} is

$$P_{T_2} = [nT_2/n_{He}]P_{He} = 1.2 \times 10^{-4} \text{ torr} ,$$

much greater than the required 10^{-9} torr.

Two chemical reactions are examined in order to decrease the T_2 pressure, namely (a) oxidation, and (b) formation of DT.

a. Oxidation

The desired $P_{T_2} < 10^{-9}$ can be achieved if all of the tritium is immediately oxidized by the addition of O_2 so that the following equilibrium is maintained,

$$T_2 + \frac{1}{2} O_2 = T_2O \ .$$

The equilibrium constant, K_{H_2O}, equals 2×10^{13} $atm^{-1/2}$ at 800°K; therefore, for $P_{O_2} = 10^{-2}$ torr and $P_{T_2O} = 10^{-2}$ torr the $P_{T_2} = 1.4 \times 10^{-13}$ torr, well below the required $P_{T_2} < 10^{-9}$ torr. The pressure of oxygen is maintained by the addition of O_2. The P_{T_2O} is maintained when a side-stream of the He coolant is cooled to 100°C and passes through a desiccant bed of molecular sieves which has a capacity to hold 20 g T_2O per kg of molecular sieves. Such a process appears to be feasible and requires that only 1.2% of the He flow be diverted to the side-stream.

In order for the oxidation/desiccant scheme to be viable, all of the tritium entering the He must be oxidized. This step has been the subject of considerable controversy recently, because the gas phase oxidation of tritium at such low concentrations without the aid of a catalyst is very slow.[4] Some catalytic effect due to the intense photon and particle radiation within the blanket would be expected; however, no experimental evidence is available. A recent experiment,[5] in which tritium gas was mixed with air and placed in the gamma and neutron flux of a fission reactor, appeared to indicate that the auto-catalyzed oxidation of tritium was retarded by the external radiation;

however, it should be remembered that such external radiation is known to lead to the formation of a complex mixture of nitrogen oxides[6] and that such species would compete and retard the formation of tritium oxide.

Based upon our review of the relevant experiments, we propose a model which predicts the in-situ formation of T_2O. Experiments which determine tritium oxidation in the gas phase are not relevant to the case of the oxidation of tritium which arrives by diffusion through a metal wall, in this case ferritic steel HT-9. It is well accepted that tritium (hydrogen) diffuses through metals in the atomic state and would, therefore, arrive at the metal/helium interface in the atomic state. These H atoms form an adhesive bond with the metal surface, until two H atoms come close enough to form an H_2 molecule and break away from the metal surface. The ability of a metal surface to hold H atoms was shown recently in an experiment[7] in which low energy H beams (< 3 eV) were directed at a clean Ni surface. In this case, the reflection of the H beam was nearly zero because the H atoms were chemically attached to the Ni surface.

The detachment of H atoms from a metal surface has been characterized[8] by a phenomenological rate constant for molecular recombination, k_r. A fundamental parameter in k_r has been shown to be α which characterizes the "cleanliness" of the metal surface. For a clean metal surface $\alpha = 1$ while for a dirty surface (oxidized) $\alpha \sim 10^{-4}$. For the case of oxygen addition to the helium, the surface of the ferritic steel must be covered with a film of oxide, Fe_2O_3. In this case, $\alpha = 0$ could be a good approximation which means no T_2 would be released; however, we know that tritium is released from oxides, although its molecular form is questionable. It is well-known that the diffusion of H atoms through an oxide is much slower than through a

metal,[8] presumably due to the formation of OH radicals. Such entities would exist on the Fe_2O_3 surface of the steel so that some of the ferric ions would be reduced to the form $Fe(OT)_2$ which would dehydrate, as follows

$$Fe(OT)_2 = FeO + T_2O \ .$$

Subsequently, the oxygen in the helium would reoxidize the iron to Fe_2O_3. Such a proposed mechanism would compete with the direct formation of molecular T_2 for which $\alpha \sim 0$; therefore, the release of T_2O from an oxidized surface in the presence of excess oxygen appears more probable.

The effect of gamma radiation on the diffusion of tritium in steel has been shown to have no effect.[9] Because of the large flux of such radiation in the HWL blanket, this observation lends validity to our calculations of the permeability of tritium through the breeder containment tubes.

b. Formation of DT

In this scenario, the partial pressure of tritium, P_{T_2}, in the helium is reduced by addition of D_2 into the He so that the following reaction occurs,

$$D_2 + T_2 = 2\ DT \ .$$

The equilibrium constant for this reaction is

$$K_P = \frac{P_{DT}^2}{P_{D_2} \times P_{T_2}}$$

and above 300°K, $K_p \sim 4$.[10]

The importance of this reaction is that at low tritium concentrations in the gas phase and $P_{D_2} > 10^3 P_{T_2}$, the permeation of tritium has been shown[2] to depend upon $P_{T_2}^{1/2}$ of the uncombined tritium. This value can be calculated from K_P and rearrangement of terms gives,

$$P_{T_2}^{1/2} = \frac{P_{DT}}{P_{D_2}^{1/2} \times K_P^{1/2}} .$$

The permeation of tritium through the steam generator at an average temperature of ~ 400°C can now be calculated by the relationship,

$$Perm_{T_2} = \phi_{T_2} \times \frac{S_A}{\omega_T} \times \frac{P_{DT}}{P_{D_2}^{1/2} \times K_P^{1/2}}$$

where

ϕ_{T_2} = the permeation coefficient for the SG tubes (670 Ci·mm/d·m^2·torr$^{1/2}$)

S_A = surface area of the SG tubes (4.4 x 10^3 m^2)

ω_T = wall thickness of the SG tubes (1 mm).

In order to determine the pressure parameters for the relationship it will be assumed that the fractional quantity, η, of the helium stream sent for tritium removal is 0.1. Then,

$$P_{DT} = 2 \times P_{T_2} \text{ (in the helium per pass)} \times 1/\eta$$

$$= 2 \times (1.2 \times 10^{-4} \text{ torr}) \times 1/0.1$$

$$P_{DT} = 2.4 \times 10^{-3} \text{ torr}$$

$$P_{D_2} = 10^3 P_{DT} = 10^3(2.4 \times 10^{-3} \text{ torr}) = 2.4 \text{ torr} .$$

Incorporation of all these terms into the permeation calculation gives

$$Perm_{T_2} = \sim 2300 \text{ Ci/d} .$$

This is 23 times larger than the desired release. In order to reduce this permeation to 100 Ci/d the P_{D_2} would have to be increased ~ 500 times to 1200 torr. At such a high P_{D_2} the D_2 would permeate through the coolant tubes in the blanket and into the plasma chamber. This is the reason that D_2 was used instead of H_2 for the swamping material. More important is the fact that D_2 would permeate into the capsules of $Li_{17}Pb_{83}$ in the blanket. The plateau pressure for the precipitation of LiD in the LiPb alloy is estimated[3] to be approximately 170 torr D_2. Therefore, most of the Li in the breeder would be precipitated as mixed LiD + LiT solid; consequently, the bred tritium release would be severely retarded.

Another factor which must be considered is that the dilution of tritium with D_2 will increase the load to be processed in the isotopic separation system. This expense can be estimated from the volume flow rate, F (kmol/h), for DT (56 mol/d) plus the amount of excess D_2. When the D_2 concentration is 10^3 times greater than the DT concentration, F = 2.34 kmol/h. If a cryogenic distillation system is used for the isotopic separation, Ontario Hydro[11] suggests that the major expense is determined by the internal circulation in the largest distillation column, V (kmol/h) which is defined as

$$V = F\left(1 - \frac{Y_\omega}{Y_F}\right) \frac{r}{\alpha - 1}$$

where: Y_ω = the tritium concentration in the return stream from the column

Y_F = the tritium concentration to the column

$r = V/V_{min}$

α = relative volatility for D_2/DT.

For our estimate, we will take $Y_\omega/Y_F = 0$, $r = 1.3$ and $\alpha = 1.33$ at 20°K; therefore V = 9.2 kmol/h. The capital cost for such a distillation system approximately follows the relationship,

$$\text{Cost} = AV^{0.366}$$

where A = \$2.5 million. In the present case, the cost would be a modest \$5.6 million. The power consumption, W, for this distillation can be approximated by the relationship, $W = BV^{0.81}$ where B = 30 kW. For the present case, W = 180 kW, a very small fraction of the total power produced by the reactor.

The conclusions of this scenario for D_2 swamping to diminish the permeation of tritium through the steam generator are as follows:

a) at a concentration of $D_2 > 10^3$ T_2 the permeation of tritium is reduced but the tritium release is >> 100 Ci/d. The D_2 swamping technique might be useful in conjection with an additional barrier, such as a double-walled steam generator.

b) the cost and power consumption for the isotopic separation system to handle the increased amount of D_2 + DT are minimal and would not negate the use of such a technique.

Based upon the above conclusions, the oxidation of tritium in the helium followed by its removal on a desiccant is favored at this time to retard the permeation of tritium through the steam generator.

5.5.3 Tritium Implantation and Diffusion in the First Wall

The first wall is subjected to a continuous flux of energetic D + T particles which become implanted at a characteristic depth in the wall. Most of these atoms diffuse to the plasma side of the wall and detach as molecules. Some fraction of these atoms diffuse to the coolant side of the wall where the tritium contaminates the heat transfer fluid. Several models[8,12] proposed to estimate the tritium diffusion to the coolant have shown that for a stainless steel first wall the tritium contamination may reach tens of grams per day.

In order to estimate the contamination of the helium coolant in the HWL first wall the following assumptions were made:

1. The flux of D + T atoms chiefly originates from the halo plasma at an average energy of 200 eV. The halo plasma for a HWL reactor has not been defined but would be generically similar to the INTOR halo plasma,[13] for which the D + T particle flux is 2.5×10^{16} atoms cm^{-2} s^{-1}.
2. Because the tubing forming the first wall has a thin wall, 1 mm, the temperature across the wall is nearly isothermal, $\Delta T = 21°C$, and the average temperature is 414°C.
3. Most of the reactor implantation diffusion calculations have utilized austenitic stainless steel as the first wall material. Because the HWL blanket utilizes ferritic steel, the implantation and diffusion for α Fe has been utilized which gives a steady-state value[12] of ~ 0.3 g(T)/d for a T flux of 1×10^{16} T atoms/$cm^2 \cdot s$, and a total wall area of 10^2 m^2, 1 cm thick.

Based upon the above assumptions the permeation flux of tritium to the helium coolant can be scaled by the relationship,

$$\text{Perm}_{T_2} = \frac{0.3\ g(T)}{d} \left(\frac{1.25 \times 10^{16}\ T\ \text{atoms/s} \cdot \text{cm}^2}{1 \times 10^{16}\ T\ \text{atoms/s} \cdot \text{cm}^2}\right)\left(\frac{106\ \text{m}^2}{100\ \text{m}^2}\right)\left(\frac{1.0\ \text{cm}}{0.1\ \text{cm}}\right)$$

$$\text{Perm}_{T_2} = 4\ g/d\ .$$

The helium will also receive some tritium by permeation through the back side of the first wall, which is exposed in the plasma chamber in front of the breeder blanket; however, the P_{T_2} in this region is very low, $\sim 10^{-6}$ torr, so that only $\sim 7\ mgT_2/d$ would permeate through the first wall.

The amount of tritium accumulation in the helium in the first wall coolant is small compared with the amount permeating into the helium from the breeder blanket, i.e. 28 moles T_2/d (168 gT/d). The combined amounts (172 g/d) of tritium can easily be removed from the helium by use of the oxidation/desiccation process proposed in the previous section.

References for Section 5.5

1. M.A. Abdou et al., "Blanket Comparison and Selection Study," Argonne National Laboratory, ANL/FPP-83-1, October 1983, p. VII-160.

2. J.T. Bell, J.D. Redman and H.F. Bittner, "Tritium Permeability of Structural Materials and Surface Effects on Permeation Rates," Proc. ANS Mtg. Tritium Tech. in Fission, Fusion and Isotopic Applications, April 1980, Dayton, OH, pp. 48-53.

3. E. Valeckis, "Thermodynamic Investigations of the Li-Al and Li-Pb Systems by the Hydrogen Titration Method," J. Less-Common Metals 73, 49-60 (1980).

4. J.R. Robins, F.E. Bartoszek and K.B. Woodall, "A Review of Tritium Conversion Reactions," Canadian Fusion Fuels Technology Project, Report No. F84027, June 27, 1984.

5. C.E. Easterly and M.R. Bennett, "Radiation Catalyzed Conversion of Tritium Gas to Tritiated Water," Nuclear Tech./Fusion 4, 116-120 (1983).

6. J.W.T. Spinks and R.J. Woods, An Introduction to Radiation Chemistry, Wiley, New York, 1976, pp. 217-220.

7. M.I. Baskes, "Dynamical Calculation of Low Energy Hydrogen Reflection," Sandia National Laboratory, SAND84-8729, June 1984.

8. R.A. Kerst and W.A. Swansiger, "Plasma Driven Permeation of Tritium in Fusion Reactors," J. Nuclear Materials 122 & 123, 1499-1510 (1984).

9. R.A. Causey and L.M. Steck, "The Effect of Gamma Radiation on the Diffusion of Tritium in 304 Stainless Steel," J. Nucl. Materials 122 & 123, 1518-1522 (1984).

10. P.C. Souers, "Cryogenic Hydrogen Data Pertinent to Magnetic Fusion Energy," Lawrence Livermore National Laboratory, UCRL-52628 (March 15, 1979).

11. S.K. Sood and O.K. Kveton, "Mirror Advanced Reactor Study," Chpt. 16.5.1, Lawrence Livermore National Laboratory (in press).

12. B.L. Doyle and D.K. Brice, "Steady State Hydrogen Transport in Solids Exposed to Fusion Reactor Plasmas, Part II: Application of Theory," J. Nuclear Materials 122 & 123, 1523-1530 (1984).

13. INTOR Group, International Tokamak Reactor, Phase Two A, Part I, Int'l. Atomic Energy Agency, Vienna, 1983, pp. 328-339.

6. Limits on Radiation Effects in Magnets

6.1 Superconducting Magnet

The shield thickness and configuration depend on the radiation limits for the superconducting (S/C) magnet. The philosophy in this work is to use the latest information for these limits with possible extrapolation to future performance levels in order to achieve the thinnest possible inboard shield that can protect the magnets from the 10 MW/m^2 neutron wall loading environment. The magnet components most sensitive to radiation in a fusion reactor are the superconductor, the stabilizer and the insulators. To obtain high magnetic fields, the superconductor material was chosen to be Nb_3Sn for which the upper critical field is 22 T at 4.2 K. Normal liquid helium (LHe-I) at 4.2 K is used as the coolant.

6.1.1 Damage to the Superconductor

The most important property for the superconductor is the critical current density (J_c). This gives the maximum current density that it can carry and still remain superconducting. Radiation damage to the superconductor produces defects. The radiation induced changes in J_c depend on the details of the defect structures and their flux pinning capabilities.[1] Unlike NbTi where a monotonic decrease in J_c is observed with neutron fluence, an initial increase of J_c with neutron fluence for Nb_3Sn was observed due to enhanced flux pinning.[2] Radiation effects in compound superconductors (Nb_3Sn) differ considerably from those in alloy superconductors (NbTi) owing to the long-range ordered atomic structure.

Most available experimental data involve irradiating the samples at fission reactor ambient temperatures.[3,4] Experiments performed with irradiation at cryogenic temperatures (5-6 K) showed that the initial J_c increase is

larger by ~ 10% than that obtained with samples irradiated at reactor ambient temperatures.[5] This is due to the fact that the defect mobility and subsequent cascade collapse during the high temperature irradiation result in lower flux pinning and a smaller J_c increase. It was also observed that the relative increase in J_c with neutron fluence is larger for higher applied fields.[5] The value of J_c reaches a maximum at fluences of ~ 4 x 10^{18} n/cm^2 (E > 0.1 MeV) and thereafter, a monotonic decrease in J_c with fluence is seen. An 80% increase in J_c with fluence was measured at a field of 10 T after irradiation to a fluence of ~ 4 x 10^{18} n/cm^2 (E > 0.1 MeV) in the High Flux Beam Reactor (HFBR) at 400 K.[3] A larger increase in J_c is expected at the field of 12.3 T considered in this study.

While room temperature annealing of NbTi results in ~ 70% recovery of the decrease in J_c[1] and hence is beneficial, room temperature annealing of Nb_3Sn results in recovering the initial increase in J_c by irradiation. This recovery increases with field. This implies that annealing of high field Nb_3Sn magnets should be avoided. Hence, the maximum allowable neutron fluence should not be reached until the end of life of the magnet. A lifetime fluence limit of 4 x 10^{18} n/cm^2 (E > 0.1 MeV) (~ 0.002 dpa) has been quoted by different researchers.[3,6] This corresponds to the fluence at which the change in J_c is zero at an applied field of 10 T (the point where J_c is maximum). However, the experimental results measured at 10 T after irradiation at 400 K show that J_c drops to its preirradiation value at a fluence of ~ 10^{19} n/cm^2 (E > 0.1 MeV).[3] Figure 6-1 reproduced from Ref. 3 shows these results. This implies that higher fluences can be used without degrading J_c much below its original unirradiated value. In this work we use a fluence limit of 4 x 10^{19} n/cm^2 (E > 0.1 MeV) (~ 0.02 dpa) which is an order of

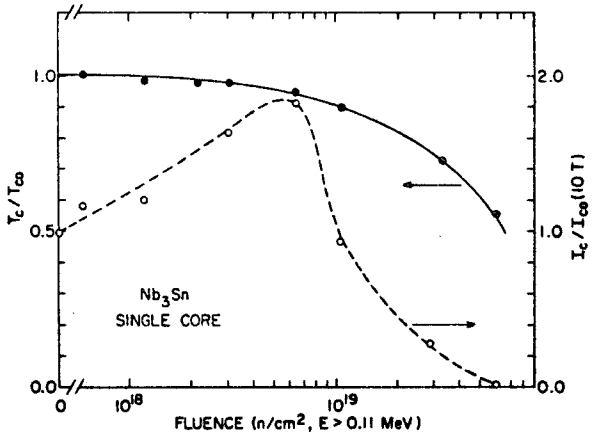

Fig. 6-1. The reduced critical temperature (midpoint of resistive transition) and the reduced critical current (measured at 10 T) are plotted as a function of neutron fluence (HFBR). The open circles and dashed curve are associated with the right ordinate, the close circle and solid curve with the left ordinate. The curves are drawn as guides for the eye only.

magnitude higher than the quoted limit. This is based on the prediction that the higher fields and lower temperatures used in this design will result in large initial increases in J_c with irradiation. Furthermore, the effect of heat treatment of the Nb_3Sn superconductor filaments has not been investigated. Extensive studies on the effect of heat treatment on J_c for NbTi have indicated that cold work develops fine scale, heterogeneous microstructure that pins fluxoids effectively and enhances J_c.

6.1.2 Damage to the Stabilizer

Most designs for fusion magnets have adopted the conservative principle of cryogenic stabilization. The stabilizer is used to provide an alternate low resistance path for the current when a part of the superconductor is driven normal by any instability. A low stabilizer resistivity is required such that the resistive heat (I^2R) produced by the current flowing in it can be removed by the coolant and the temperature kept below the critical temperature for the superconducting mode to resume. The resistivity of the stabilizer at the operating magnetic field and temperature is, therefore, the important parameter.

Neutron irradiation at cryogenic temperatures produces immobile point defects in the stabilizer which decrease the mean free path of the conduction electrons resulting in a radiation induced resistivity $\Delta\rho_r$. This radiation induced resistivity, which is related to damage in the stabilizer, must therefore be limited to a maximum value for the magnet to be cryostable. The upper limit on the total resistivity at the field B is given by

$$\rho_{max}(B) = q''_{max} A_{st} P / I^2 \ , \qquad (6.1)$$

where A_{st} is the stabilizer cross section area, P is the wetted perimeter and I is the conductor current. q''_{max} is the maximum heat flux that can be removed by the coolant. It is clear that the resistivity limit depends on the magnet design parameters.

Copper and aluminum are the two stabilizer candidates. Because of its strength, fabricability and small radiation induced resistivity, copper appears to be the favored material. Determination of the dpa rate limit in Cu is complicated by the dependence of the resistivity at the operating field on the radiation induced resistivity and the purity of Cu. This dependence is usually represented by the Kohler plot.[7] Furthermore, partial recovery (80-90%) of radiation induced defects can be achieved by room temperature annealing.[8]

We have generated charts for determining the maximum allowable damage rate in copper stabilizer.[9] An algorithm for determining the dpa rate limit for given magnet design and reactor availability requirements is summarized in the flow chart of Fig. 6-2. The charts used to determine the limit on radiation induced resistivity and the minimum time before the first magnet anneal are given in Figs. 6-3 and 6-4, respectively.

In this design we assume a maximum S/C current density of 8×10^4 A/cm^2. The Cu:S/C ratio is taken to be 16:1 and the conductor packing factor is assumed to be 85%. This implies an average winding pack current density of 4000 A/cm^2. The conductor is assumed to have a square cross section with 50% of the conductor perimeter being wetted by the LHe-I coolant.

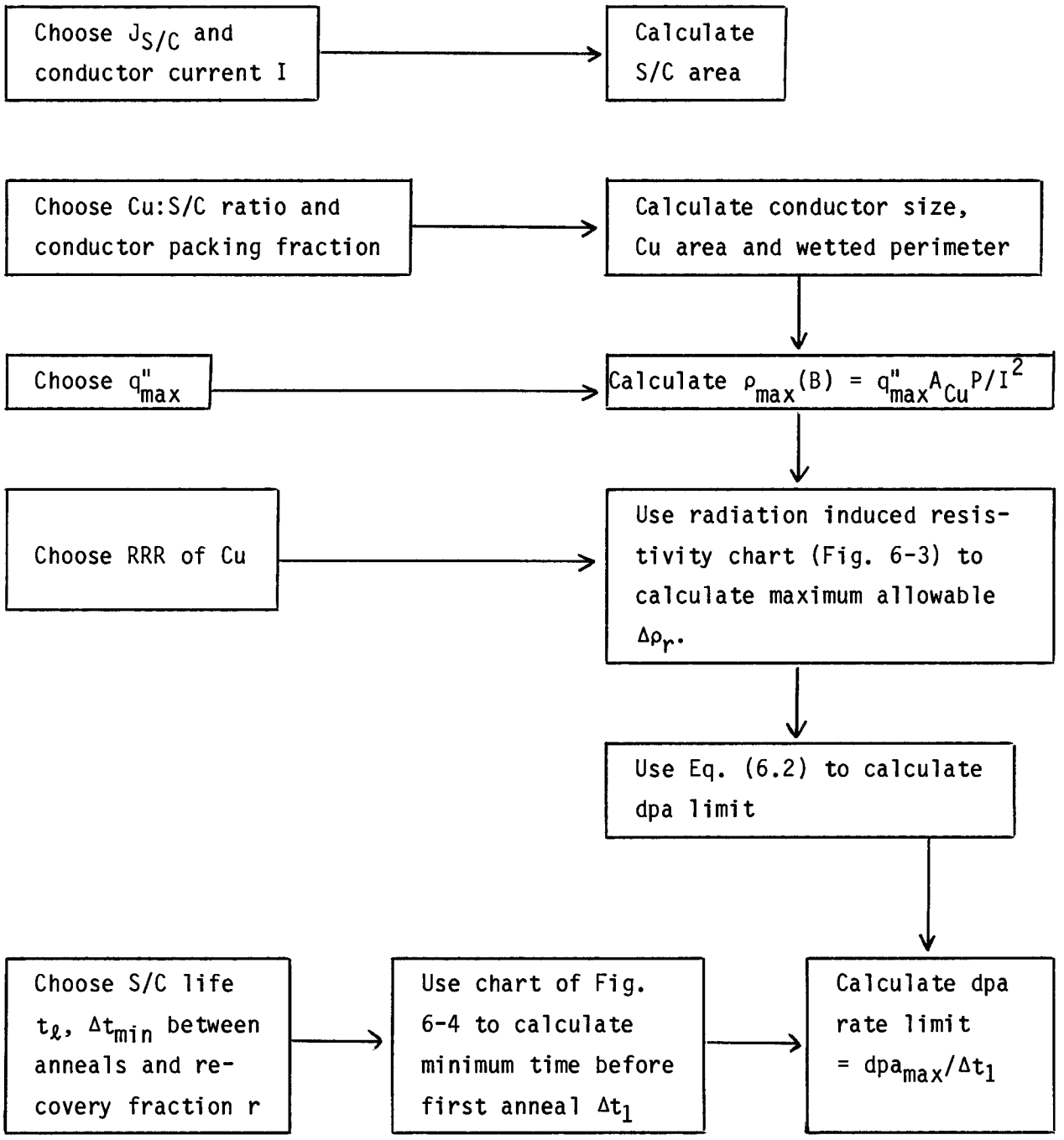

Fig. 6-2. Flow chart for calculating dpa rate limit in Cu.

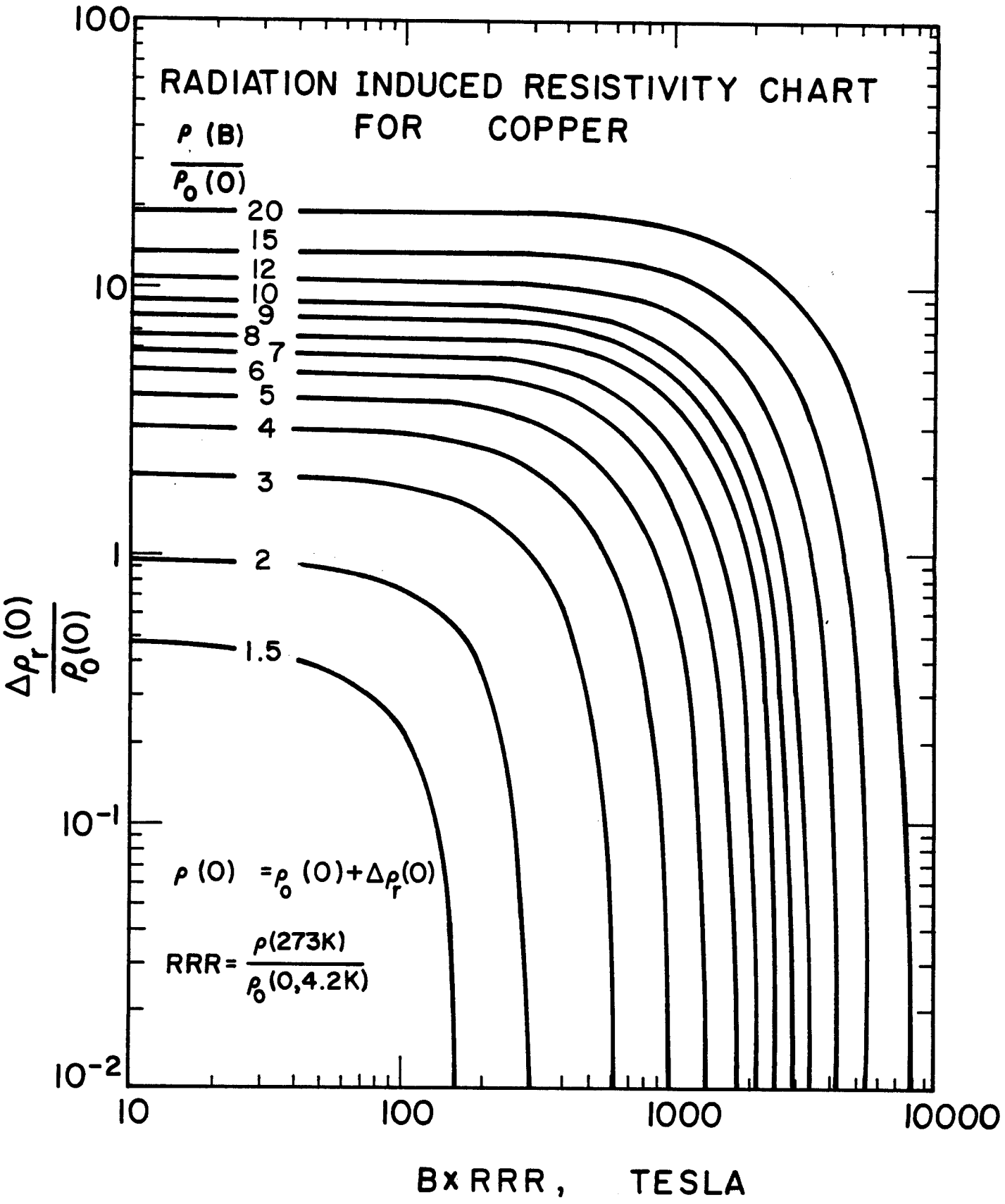

Fig. 6-3. Radiation induced resistivity chart for Cu.

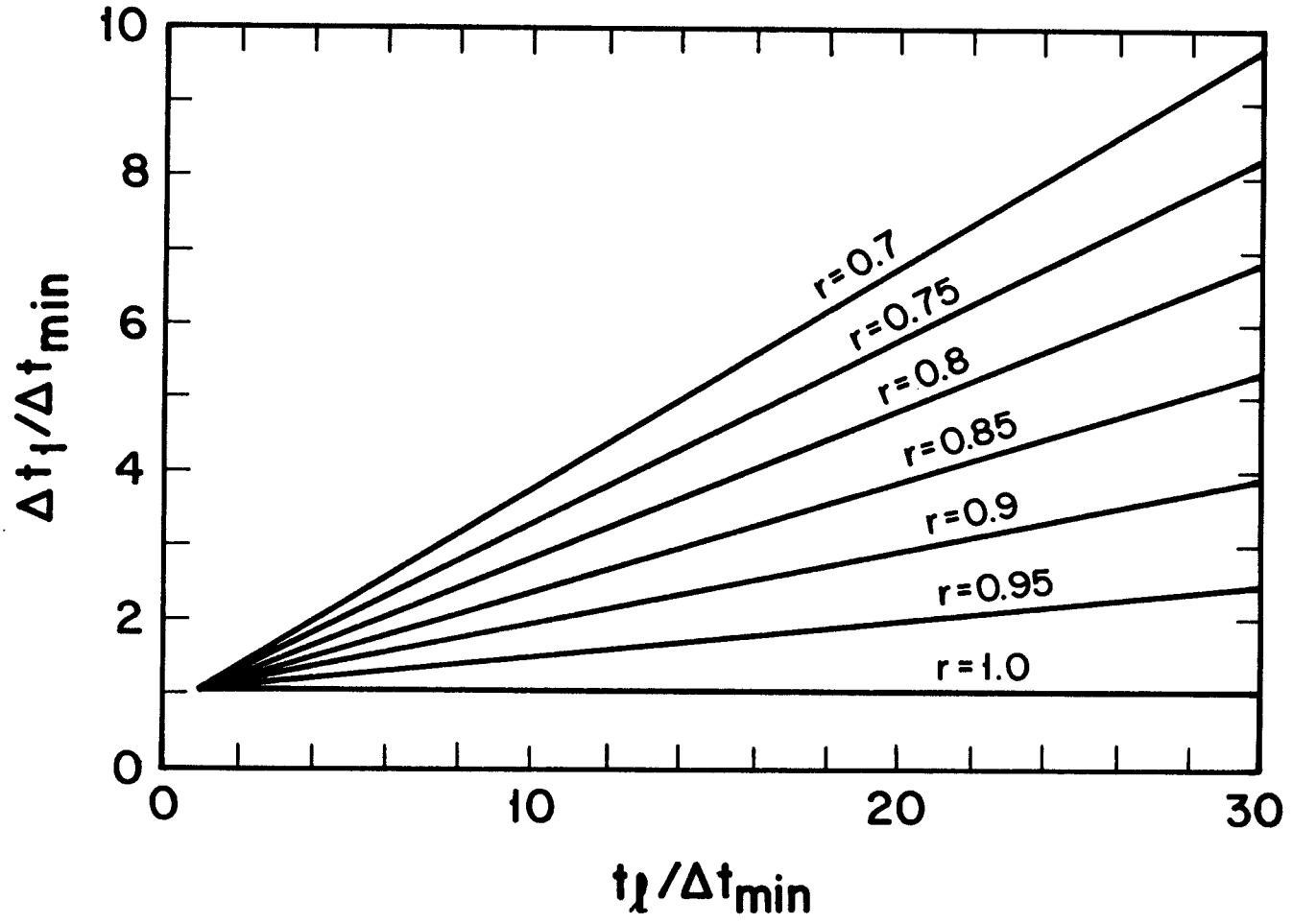

Fig. 6-4. Chart to determine minimum time required before first magnet anneal.

LHe-I can handle a heat flux of up to 0.3 W/cm^2. The coolant must be able to remove not only the I^2R heat produced in abnormal conditions but also the continuous heat production resulting from nuclear heating in the magnet. Hence, the value of q''_{max} used in Eq. (6.1) should be less than 0.3 W/cm^2 to allow for a margin that can handle nuclear heating. In this study, we considered q''_{max} to be 0.29 W/cm^2 leaving a 0.01 W/cm^2 margin to handle nuclear heating. Half hard Cu with a residual resistivity ratio RRR = 80 is considered here. The relation between $\Delta\rho_r$ and Cu dpa is taken to be

$$\Delta\rho_r = 300[1 - e^{-240\ \text{dpa}}]\ \text{n}\Omega\ \text{cm} . \qquad (6.2)$$

It was obtained by Guinan et al.[10] using the neutron spectrum at the MARS[11] central cell S/C coils.

Originally, we assumed an operating current in the conductor of 500 A yielding a conductor size of 0.354 cm. Using a maximum heat flux of 0.29 W/cm^2, Eq. (6.1) yields $\rho_{max}(B)$ = 96.62 nΩ cm. Using the chart in Fig. 6-3 implies that the radiation induced resistivity should not exceed 17.4 nΩ cm. This relatively low limit on radiation induced resistivity is due to the large Cu magnetoresistivity at 12.3 T which was calculated to be 77 nΩ cm. Using Eq. (6.2) gives a dpa limit of 2.5 x 10^{-4}. The reactor life was assumed to be 24 FPY. The minimum time between magnet anneals determined from availability considerations was set to be 1 FPY. Assuming a recovery fraction of 0.85, the chart in Fig. 6-4 indicates that the time before the first magnet anneal should be at least 4.45 FPY and eleven magnet anneals will be needed during the 24 FPY reactor life. This implies that the dpa rate should not exceed 5.6 x 10^{-5} dpa/FPY if an operating conductor current of 500 A is used. The 66 cm

thick optimized shield that gives a neutron fluence at the S/C of 4 x 10^{19} n/cm^2 (E > 0.1 MeV) was found to yield a dpa rate of ~ 1.5 x 10^{-3} dpa/FPY in the Cu stabilizer. This implies that the magnet will not be unconditionally cryostable if a conductor current of 500 A is used.

There are several options to remedy this situation. One can rely on end zone stabilization where the conductor can recover by heat transfer along the conductor axis. Other stabilization mechanisms such as adiabatic stabilization can be considered. Another possibility is using Al stabilizer because of its much smaller magnetoresistivity. However, Al has a much larger radiation induced resistivity for the same neutron fluence (saturation resistivity is 800 nΩ cm versus 300 nΩ cm for Cu). Furthermore, extra structure is needed to provide strength which reduces the stabilizer area or increases the coil cross section area. Our calculations indicate that Cu is preferable to Al in this design.

If unconditional cryostability is required without increasing the inboard shield thickness, it will be necessary to reduce the conductor current and conductor size. This is equivalent to dividing the conductor into several smaller conductors to enhance the cooled area. The total coil cross sectional area remains the same. The maximum conductor current that can be used for the magnet to be cryostable with a peak dpa rate of 1.5 x 10^{-3} dpa/FPY is 52 A. This corresponds to a conductor size of 0.114 cm. It is interesting to note that Eq. (6.2) implies a saturation value of 300 nΩ cm for the radiation induced resistivity in Cu. Hence, if the magnet is designed such that the coolant can remove the I^2R heat produced by the residual resistivity, magnetoresistivity, and the saturation radiation induced resistivity, it will be unconditionally cryostable regardless of the amount of damage produced in the

stabilizer. In such a design, no limit needs to be specified for the dpa rate and no magnet annealing will be necessary. In order to achieve this, the conductor current should not exceed 35 A implying that the conductor size should be 0.093 cm at most. It is clear that the limit on dpa rate can be removed completely by a small reduction in conductor size and current. Therefore, a conductor 0.093 x 0.093 cm in size which carries 35 A was chosen for this design. Such small conductor sizes can be achieved by designing a braided conductor with a small current flowing in each braid. The braided conductor can be placed in a steel jacket. Such a design is possible based on experience with the Westinghouse Nb_3Sn LCP forced flow conductor.[12] It should also be noted that the largest damage to the stabilizer occurs only in the innermost layers of the coil. Hence, a graded coil can be used with larger conductor sizes and currents used in the outer grades.

6.1.3 Nuclear Heating Limit

The heat flux margin that can be used by nuclear heating is 0.01 W/cm^2. For the chosen conductor parameters, this corresponds to a volumetric power density of ~ 170 mW/cm^3. This is the maximum allowable peak power density in the winding pack resulting from nuclear heating. This is a very large value and does not impact the shield design. However, much lower power densities are required to avoid excessively high cryogenic refrigeration and plant cost. The 66 cm thick optimized shield used in this study yields a peak power density of ~ 1.3 mW/cm^3. Since the power density decreases as one moves towards the outer layers of magnet and these high power densities are obtained only on the inboard section of the coil where limited shielding space is available, this does not result in an excessive cryogenic heat load. The total power generated in the inboard sections of the twelve coils is ~ 3 kW.

6.1.4 Dose Limit to the Insulators

The insulators are intended to carry the Lorentz forces on the conductors, provide space for liquid helium coolant, and prevent shorting or breakdown between turns of the magnet or to the magnet case. The strength and resistivity of the insulators are the important properties. Experimental data for fiber-reinforced organic insulators indicate that the mechanical properties degrade at a lower dose than do the electrical ones.[6]

Mechanical strength tests of irradiated magnet insulators have shown that polyimides are 5 to 10 times more radiation resistant than comparably prepared epoxies.[13] These results indicate that more than 65% of the compression strength of glass filled fiber (gff) polyimide is retained up to a dose of $\sim 10^{10}$ rad. In these experiments, samples of several millimeters thick cylindrical rods of polyimide were gamma irradiated at 5 K and the mechanical properties (flexural and compression strengths) were determined at 77 K and 300 K. The samples are representative of relatively thick sheets of insulators placed between conductors. Both compression and interlaminar shear are important in this mode of application of the insulator materials.

Recently, thin disks of gff epoxies and polyimides were irradiated at 325 K and tested at room temperature. The disks are 0.5 mm thick and 11.1 mm in diameter.[14] These are representative of the case when thin sheets of insulators are sandwiched between large conductor plates and held in compressive load only. The samples were irradiated to mixed gamma and neutron doses of $\sim 4 \times 10^{11}$ rads. Static compression tests were made to a maximum stress level of 2750 MPa with no failures observed. This indicates that dose limits of $\sim 4 \times 10^{11}$ rads can be used for the polyimide insulator provided it is used in the form of thin disks loaded in compression only. The insulator may have to be a

composite of thin sheets of insulator sandwiched between metal plates. Helium flow channels could be cut into this composite material and the shear stresses could be born by the metallic component.[15] In this study, a gff polyimide is used as electrical insulator. The end of life dose limit for the insulator is taken to be 4×10^{11} rad.

Aluminized mylar has been used in previous designs as superinsulator (thermal insulator). However, recent experiments showed a large drop in its strength after irradiation to 6×10^{8} rads.[16] No failure of any type was observed in aluminized Kapton up to a dose of 10^{10} rads implying that it can serve as superinsulation at these doses.[17] The superinsulator is located in front of the magnet case and is, therefore, exposed to doses higher than those in the electrical insulators. It is, therefore, essential to use a superinsulator that can withstand higher radiation doses. For this reason aluminum sheets supported with glass paper are used for superinsulation in the inboard leg of the S/C magnet. These are believed to stand very high radiation doses. Aluminized Kapton can be used in the outboard side where large shielding space is available.

6.2 Normal Magnet

In this magnet, there is concern with both electrical and mechanical degradation of the ceramic insulation and the electrical resistivity of the copper conductor due primarily to neutron-induced transmutations. An additional irradiation problem is radiolytic decomposition of the water coolant leading to corrosion/erosion product formation. Among the most important mechanisms mentioned above, only one was found as lifetime limiting for the normal coil,[18] namely the neutron-induced swelling in the ceramic insulator.

There are common ceramic insulators that are used for the insulation in the normal conducting coils, such as alumina (Al_2O_3), magnesium oxide (MgO), and spinel ($MgO \cdot Al_2O_3$). The ceramics are available in a compacted powder or solid form. A reasonable experimental data-base on neutron-induced swelling exists for these materials.[19] Al_2O_3 is the most fully-developed ceramic. However, it suffers from microcracking that results from anisotropic swelling. MgO is a well-developed ceramic with good physical properties. It is a candidate for those applications where Al_2O_3 is appropriate, whereas for high irradiation environments MgO is preferable. MgO is the most popular form of powdered insulators being used in high irradiation fields. MgO powder has been used successfully in highly irradiated normal magnets.[20] Available evidence suggests that there are probably no life-limiting mechanisms associated with neutron damage for the powdered insulators[21] with the possible exception of degradation of the electrical properties. Spinel is of particular interest in the high neutron irradiation environment because of the superior absence of swelling, particularly in the single crystal form.

A stress analysis shows that 3 vol.% neutron-induced swelling in the insulator can be accommodated in the normal magnet structure without causing stress problems.[11] Therefore, the neutron fluence limits[19] for the use of the solid polycrystalline spinel, magnesia, and alumina in normal magnets are 4×10^{22}, 10^{22}, and 5×10^{20} n/cm^2 ($E_n > 0.1$ MeV), respectively, in the temperature range 100-300°C. These are based on 3 vol.% radiation-induced swelling in spinel and MgO, and one-tenth (factor of safety) of the fluence for observed microcracking in the Al_2O_3.

References for Section 6

1. B. Brown, J. Nucl. Mat. 97, 1 (1981).

2. C. Snead, Jr. and D. Parkin, Nucl. Technology 29, 264 (1976).

3. C. Snead, Jr. et al., J. Nucl. Mat. 103 & 104, 749 (1981).

4. D. Parkin and D. Schurtzen, Nucl. Technology 22, 108 (1974).

5. B. Brown et al., J. Appl. Phys. 49, 4144 (1978).

6. R. Van Konynenburg and M. Guinan, "Relative Radiation Sensitivity of Insulators, Stabilizers, and Superconductors," UCID-19292, Lawrence Livermore Laboratory Report (1982).

7. F. Fickett, "Magnetoresistivity of Cu and Al at Cryogenic Temperatures," Proc. 4th Intl. Conf. Magnet Technology, CONF-720908, pp. 539 (1972).

8. B. Brown et al., J. Nucl. Mat. 52, 215 (1974).

9. M. Sawan, "Charts for Specifying Limits on Copper Stabilizer Damage Rate," J. Nucl. Mat. 122 & 123, 1376 (1984).

10. M. Guinan et al., "Defect Production and Recovery in FCC Metals Irradiated at 4.2 K," Proc. 3rd Top. Mtg. Fusion Reactor Materials, Albuquerque, NM, Sept. 1983.

11. B. Logan et al., "The Mirror Advanced Reactor Study (MARS) Final Design Report," UCRL-53333-83, Lawrence Livermore National Laboratory (1984).

12. P. Sanger et al., "Design Considerations for the Nb_3Sn Forced Flow Conductor for LCP," Proc. 7th Symp. on Engineering Problems of Fusion Research, IEEE publication #77CH1267-4-NPS, pp. 948 (1977).

13. R. Colman and C. Klabunde, J. Nucl. Mat. 103 & 104, 717 (1981).

14. R. Shmunk et al., "Tests on Irradiated Magnet Insulator Materials," Proc. 3rd Top. Mtg. on Fusion Reactor Materials, Albuquerque, NM, Sept. 1983.

15. K. Agarwal, General Dynamics, private communications (July 1983).

16. S. Takamura and T. Kato, J. Nucl. Mat. 103 & 104, 729 (1981).

17. C. Long et al., "Effects of Radiation at 5 K on Organic Insulators for Superconducting Magnets," Special Purpose Materials Progress Report, U.S. DOE Report DOE/ER004811, pp. 73 (1981).

18. L.A. El-Guebaly et al., "MARS Axicell Radiation Damage and Shielding Analysis," Nuclear Technology/Fusion 4, No. 2, Part 3, p. 1171 (1983).

19. L.A. El-Guebaly, "Material Considerations for ICRH Ceramic-Filled Waveguide Launchers," University of Wisconsin Fusion Engineering Program Report UWFDM-579 (1984).

20. J.H. Schultz, "Design Practice and Operational Experience of Highly Irradiated, High Performance Normal Magnets," J. Fusion Energy 3, No. 2, p. 119 (1983).

21. F. Clinard, "Status of Inorganic Insulators for Fusion Magnets," presented at the Workshop on Insulators for Fusion Magnets, Philadelphia, Pennsylvania, Dec. (1983).

7. ADVANCED SHIELD DESIGN

7.1 Introduction

The field of high power density compact tokamak research has established the needs for advanced shielding design to protect the superconducting (S/C) magnet from the intense neutron source. The cost of the tokamak reactor is extremely sensitive to the inboard shield thickness. Millions of dollars could be saved for every cm shaved off of the inboard shield thickness. On this basis, methods to improve the shielding capability of the inboard region are needed by innovative materials and/or geometric design modifications.

The optimum inboard shield design depends on the allowable radiation damage limits for the S/C magnet. The radiation effects of concern in the S/C magnet are the nuclear heat load, the atomic displacement rate (dpa) in the stabilizer, the fast neutron fluence in the superconductor, and the dose to the insulators. The inner leg of the S/C magnet is operating in a severe radiation environment and is designed for high performance (high magnetic field, high current density, etc.). The limited space available for the inboard shield to protect the S/C magnet from the intense neutron source (10 MW/m^2 wall loading), strongly suggests the need for a shield optimization study to minimize the four most important responses mentioned above.

The S/C magnet is liquid helium I cooled. It utilizes highly radiation resistant electrical and thermal insulators, namely the GFF polyimide and the glass-paper supported Al sheets, respectively. The production of the 12.3 T magnetic field mandates the use of Nb_3Sn as the superconductor. The S/C magnet shielding requirements are set by a number of radiation limits. These limits are discussed more fully in Section 6 and in some cases the conventional limits were pushed to allow for progress in the the next 5-10 years.

In summary, the end of life peak dose in the GFF polyimide was taken as 4 x 10^{11} rad. The limit on the nuclear heat load in the S/C magnet is design-dependent. Although winding pack peak power densities as large as ~ 0.1 W/cm^3 can be tolerated by the HeI cooling system, much lower power densities are preferable to avoid excessively high cryogenic plant cost and power. To avoid degradation of the critical current density for the superconductor material, the peak neutron fluence (E_n > 0.1 MeV) in the S/C magnet should not exceed 4 x 10^{19} n/cm^2 at the end of the reactor life. The conductor is designed in a way that allows the magnet to be unconditionally cryostable regardless of the damage produced in the stabilizer. This implies that no upper limit on the dpa rate needs to be specified and no magnet annealing is required during the reactor life.

Both S/C and resistive coils are required to produce the "bean" shaped plasma. The copper resistive magnet encircles the inner leg of the S/C magnet and is embedded in the inboard shield. It should be placed close to the plasma with minimal shield to effectively produce the "bean" shape. The insulator could be the weak point in the performance of the normal magnet, unless it is properly chosen. The structural degradation of the insulator appears to be lifetime limiting for the normal magnet. The high fast neutron fluence at the inboard first wall mandates the use of a highly radiation resistant insulator, such as MgO in powder form. In the back layers of the magnet where stresses are severe, the solid spinel can be used up to its limit of radiation stability since it offers the lowest degree of swelling among its class of cubic ceramics. The fast fluence limits for the compacted powder MgO and solid polycrystalline spinel are taken as 2.35 x 10^{23} and 4 x 10^{22} n/cm^2 (E_n > 0.1 MeV), respectively, based on 60% filling factor for the powdered MgO (67 v/o swelling) and 3 v/o swelling in the spinel.

7.2 Normal Magnet Shielding

In view of the fact that the peak neutron wall loading at the inboard shield is ~ 10 MW/m^2, the normal magnet is highly irradiated. It is designed to operate for 24 full power years (FPY); the designed lifetime of the reactor. The one-dimensional calculations result in an end of life peak neutron fluence (E_n > 0.1 MeV) of ~ 4 x 10^{24} n/cm^2 for the case where the normal coil is positioned with no intervening shield between its coil case (0.02 m thick) and the first wall. This indicates that some shielding needs to be introduced in front of the normal magnet in order to satisfy the design limits for the insulators. The most effective material in attenuating the fast neutrons is tungsten and our results show that 16 cm of W-shield [80 v/o W (95% d.f.), 10 v/o Fe 1422, and 10 v/o H_2O] adequately protect the normal magnet. Moreover, the MgO powder insulator can be used in the front 14 cm thick layers of the magnet and the spinel in the back layers. In the calculations the 20 cm thick normal magnet composition was taken as 64 v/o Cu, 24 v/o insulator, and 12 v/o H_2O.

7.3 Inboard Shield Optimization

The primary motive for the optimization study is to find an optimal combination of the shielding materials that minimizes the fast neutron fluence in the S/C magnet which was found to be the design driver for the shield. However, it is beneficial from the cost standpoint to reduce the nuclear heating as much as possible. The inboard region is represented schematically in Fig. 7-1. The space for the normal magnet and the shield is constrained to 0.66 m in addition to 0.11 m thick cryostat (Fig. 7-2 details the composition). In this regard the use of tungsten in the shield is essential to provide adequate protection for the S/C magnet. A series of one-dimensional

Schematic of the Inboard Shield, normal and S/C magnets
Radius (m)
Thickness (cm)
0.00
52
Void
0.52
11
Cryostat
0.63
50
S/C Coil
1.13
11
Cryostat
1.24
3
Void
1.27
66 cm
26
Shield
1.53
2
coil case
1.55
20
Normal Magnet
1.75
2
coil case
1.77
16
W-Shield
1.93
1
First Wall
1.94
9
scrape off zone
2.00
60
Plasma
2.60
60
3.20
10
scrape off zone
3.30
Blanket / Shield

Figure 7-1.

Fig. 7-2

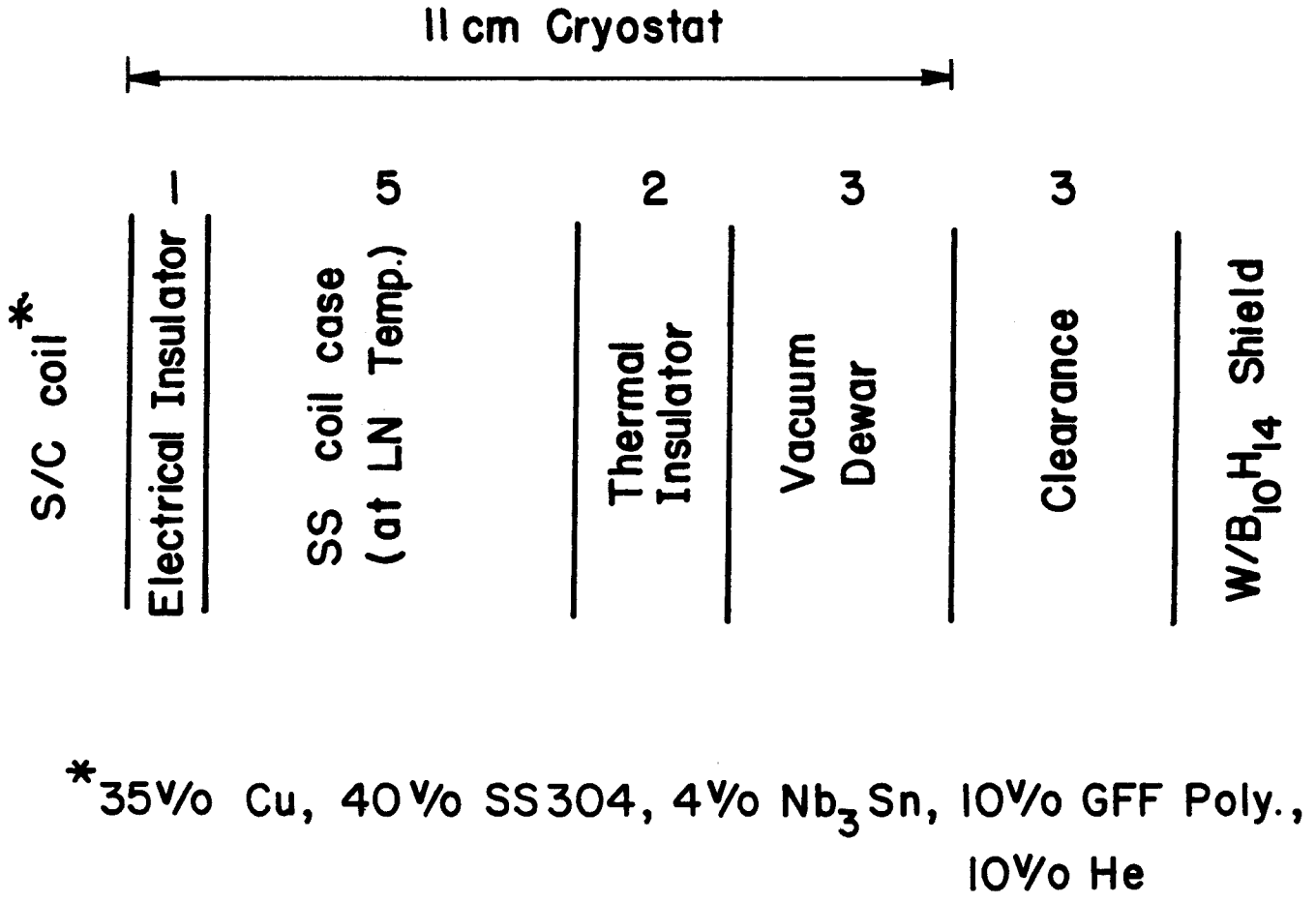

*35V/o Cu, 40V/o SS304, 4V/o Nb_3Sn, 10V/o GFF Poly., 10V/o He

Fig. 7-2. Details of the S/C magnet cryostat.

(1-D) calculations was performed to determine the optimal shield configuration using the discrete ordinates code ONEDANT,[1] the cross section library XSLIB (30 neutron and 12 gamma energy groups) based on the ENDF/B-V evaluation, and the P_3-S_8 approximation, in toroidal cylindrical geometry.

Several materials have been considered for the shield to reduce the fast neutron fluence and the nuclear heating in the S/C magnet. These materials are tungsten (W), stainless steel (Fe 1422), boron carbide (B_4C), titanium hydride (TiH_2), lead (Pb), and boron hydride[2] ($B_{10}H_{14}$) - a new material for shielding applications. The hydrides are effective in minimizing the fast neutron fluence due to the high hydrogen content which helps moderate the neutrons via elastic scattering interactions. The borides are superior in reducing the nuclear heating due to the remarkably high absorption cross sections of boron for intermediate and low energy neutrons.

Boron hydride is a well-developed material. It has been produced commercially on a large scale although it is presently expensive for small quantities (~ \$450/kg). It is quite reactive, kinetically stable up to 150°C, and decomposes at higher temperatures. Thus, to avoid the reaction of the products with air it must be kept in an inert atmosphere; it slowly hydrolyzes in water. It has a density of 0.94 g/cm^3 at room temperature and a melting point of 100°C.[3] It should be emphasized that the $B_{10}H_{14}$ will only be placed at the back of the shield where the temperature is surely below its melting point. Also, the extent of radiation damage of $B_{10}H_{14}$ in this position needs to be carefully examined.

There is some concern for using $B_{10}H_{14}$ in the shield from the safety standpoint. However, it is a useful candidate and its applicability for fusion reactor shielding deserves further consideration. A much more stable

product is obtained by a series of reactions in which acetylene is inserted into the $B_{10}H_{14}$ structure to give $B_{10}C_2H_{12}$. This compound shows an enhanced thermal stability compared to the parent $B_{10}H_{14}$. It is stable up to 400°C and has a melting point of ~ 300°C. A very large number of other derivatives are known and a very large number of polymers have been produced. All of these have enhanced thermal stabilities. However, none of them provides neutronically the required properties as compared to the parent $B_{10}H_{14}$, as shown later.

TiH_2 (95% d.f.), B_4C (87% d.f.), and $B_{10}H_{14}$ shield layers were used separately to back up the W-shield between the normal and superconductor magnets (see Fig. 7-1). In all shields, 10 v/o Fe 1422 structure, 10 v/o H_2O, and 90% ^{10}B in B were used. The thicknesses of these layers were varied between zero (an all W-shield) and 0.14 m and the total shield thickness was kept fixed. A comparison between the effectiveness of these shielding materials in reducing the radiation effects in the S/C magnet is outlined in Figs. 7-3 through 7-6. As mentioned before hydrides are effective in minimizing the fast neutron fluences while borides are superior in reducing the nuclear heating. Furthermore, boron hydride has proven to be competitive with the other conventional shielding materials and has the beneficial effect of minimizing both responses simultaneously. The more stable compound $B_{10}C_2H_{12}$ was also examined as a shield. It results in 20 and 33% increases in the fluence and nuclear heating, respectively, compared to the $B_{10}H_{14}$-shield. Thus, it is anticipated that the even more stable compounds, such as $B_{10}C_3H_{14}$ and $B_{10}C_4H_{16}$, will provide less attractive neutronics performance.

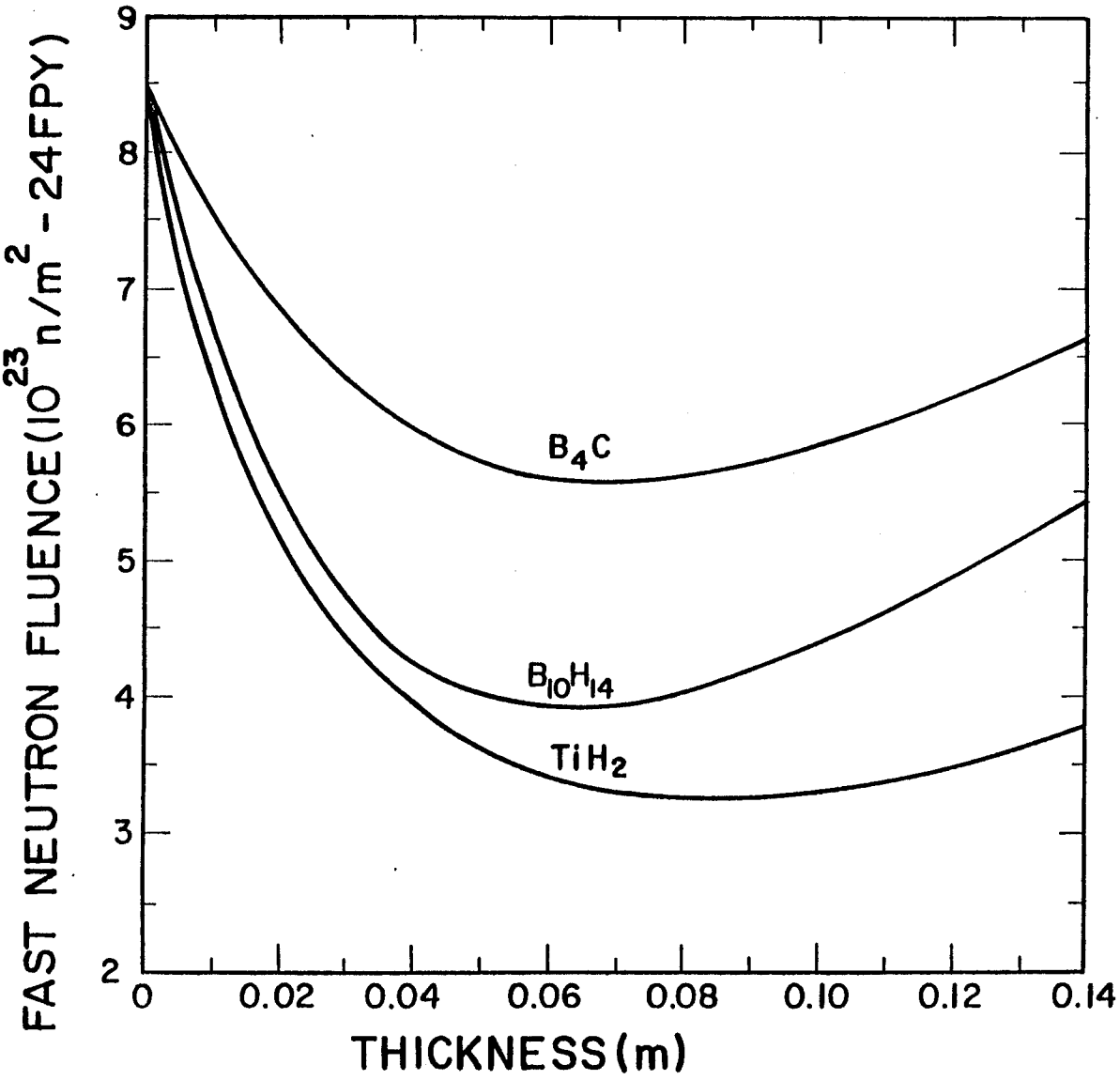

Fig. 7-3. Peak fluence in the S/C magnet versus the backup layer thickness.

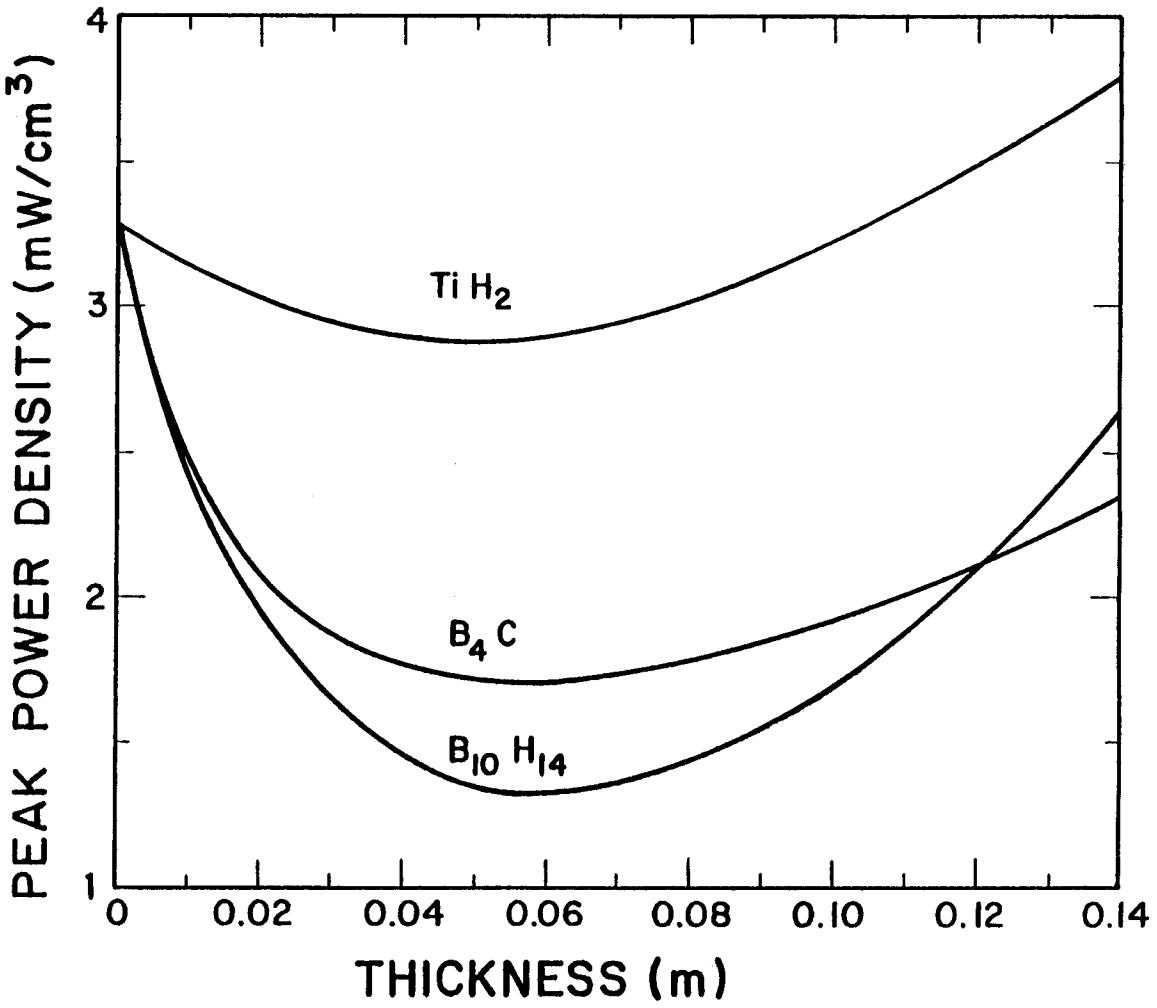

Fig. 7-4. Impact of varying the backup layer thickness on the nuclear heating in the S/C magnet.

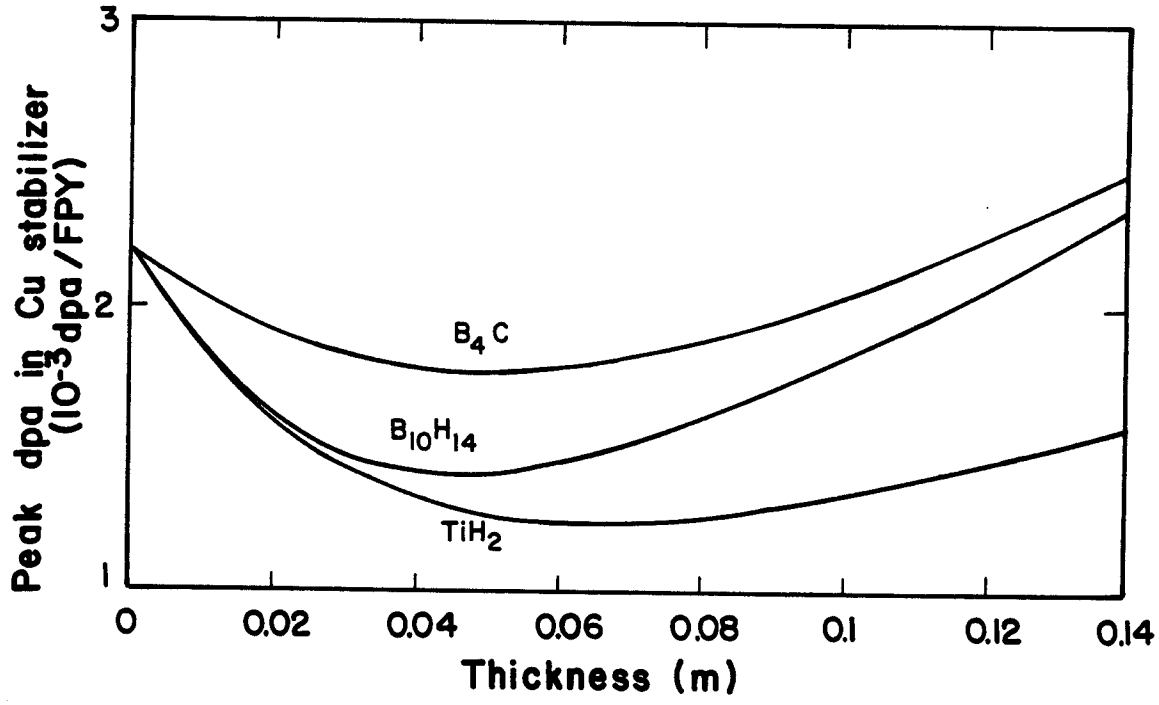

Fig. 7-5. Variation of the dpa in the stabilizer with the backup layer thickness.

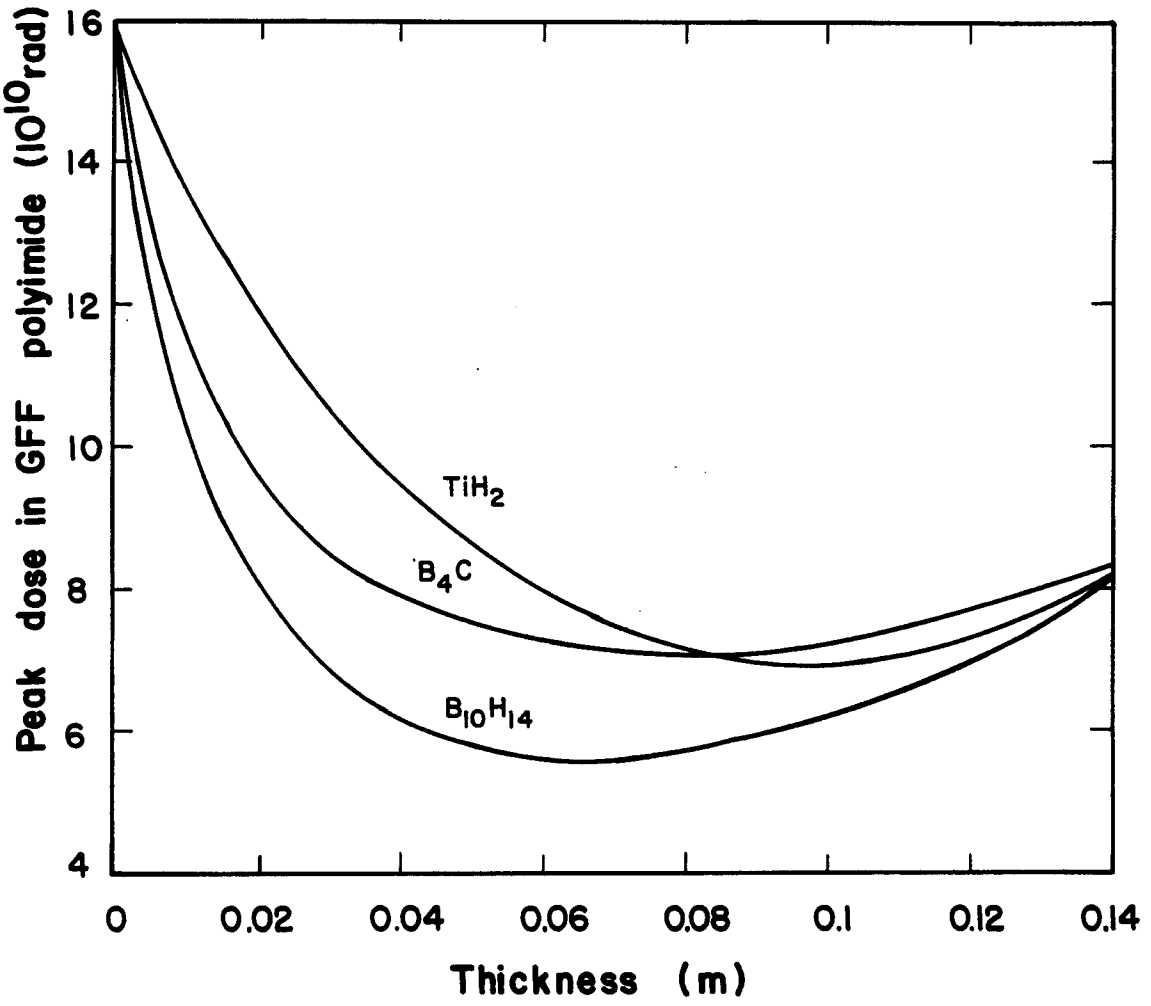

Fig. 7-6. Effect of the backup layer thickness on the dose in the electrical insulator.

An attempt was made to reduce the nuclear heating without substantially affecting the fluence by using borated water to cool the shield. The solubility of boric acid in water has a strong temperature dependence. For an inlet coolant temperature of ~ 100°C in the inboard shield, the maximum allowable concentration of boric acid in water is ~ 11 vol.%[4] Our results show that the borated water was only effective in the case of the W/TiH_2 shield where the power density was reduced by ~ 30%. However, a lower nuclear heating was achieved with the optimum combination of water cooled $W/B_{10}H_{14}$ shield.

The effect of the water content in the inboard shield was examined. To minimize the fast neutron fluence, as little water as possible is required for the cases of W/TiH_2 and $W/B_{10}H_{14}$ shields. Thus, the water content in the shield should be dictated by cooling requirements, rather than neutronics performance. In order to meet the cooling demand for this high wall loading reactor, a 10 vol.% water content was considered in the shield. If all steel or tungsten shields are used the optimal water contents are 30 and 18 vol.%, respectively.

The optimum thicknesses of the B_4C, TiH_2, and $B_{10}H_{14}$ shields that minimize the fast neutron fluence are 0.07, 0.08, and 0.06 m, respectively (Fig. 7-3). Table 7-1 summarizes the radiation effects in the S/C magnet for the different optimal shields. The results are also presented by bar charts in Fig. 7-7. Evidently, the $W/B_{10}H_{14}$ shield is the best for meeting the combined criteria of reducing both responses and, hence, provides the thinnest possible inboard shield.

Table 7-1. Peak Radiation Effects in S/C Magnet

($10\ MW/m^2$ at inboard shield)

Optimum Shield Composition	Fast Neutron Fluence (10^{19} n/cm^2)	Nuclear Heating (mW/cm^3)	dpa in Cu Stabilizer (10^{-3} dpa/FPY)	Dose in GFF Polyimide (10^{10} rad)
Fe[a]	26.25	11.28	8.39	44.07
W[b]	7.37	2.65	2.16	12.25
W/B_4C[c]	5.57	1.73	1.82	7.10
W/TiH_2[d]	3.31	2.13	1.29	6.28
$W/B_{10}H_{14}$[c]	3.94	1.31	1.48	5.59
Design Limits	4	~ 1	-	40

a 30 v/o borated water

b 18 v/o H_2O, 10 v/o Fe 1422 structure

c 10 v/o H_2O, 10 v/o structure

d 10 v/o borated water, 10 v/o structure

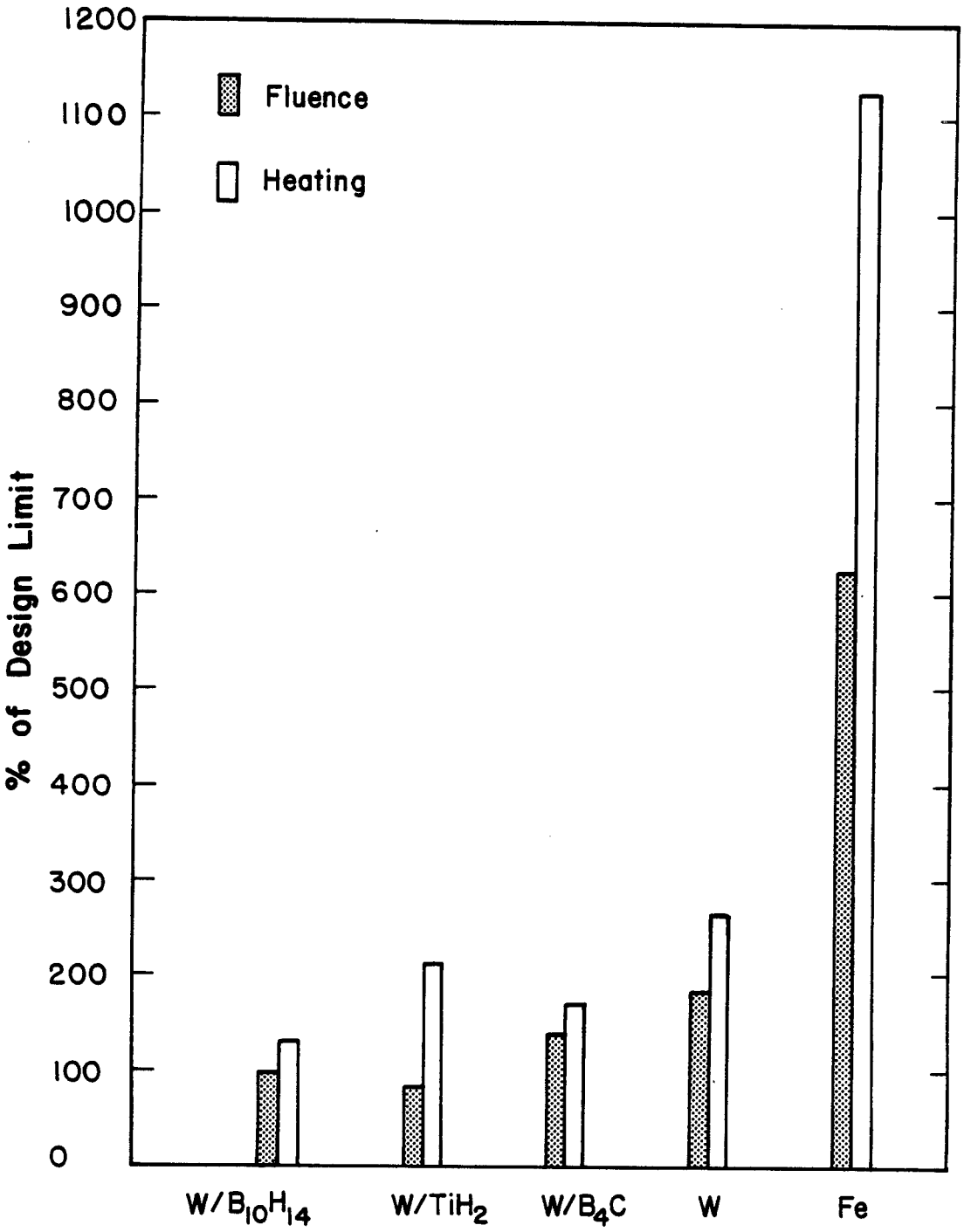

Fig. 7-7. Comparison of the effectiveness of the optimal shields.

The option of using lead in the shield was also investigated. The motivation for considering Pb for the shield is that ~ 80% of the nuclear heating in the S/C magnet is gamma heating and Pb is a good gamma absorber. A 2 cm thick layer of Pb-shield was added behind the $W/B_{10}H_{14}$ shield and the clearance zone thickness between the shield and the S/C magnet was reduced to 1 cm. The effect on the two most important responses is reported in Fig. 7-8b along with the integrated total nuclear heating in the S/C coil per unit length. It is worth mentioning that the gamma heating in the S/C coil results from gamma rays:

- transported from the shield,
- generated in the coil case and vacuum dewar,
- generated in the S/C coil itself.

Baking the $W/B_{10}H_{14}$ shield with Pb-shield helps attenuate the first source of gamma rays and in order to attenuate the other two sources a 2 cm thick Pb-shield was added inside the cryostat as shown in Fig. 7-8c. In this case, the Pb-shield is cooled at LN temperature and should be strong enough to pass the magnetic forces to the coil case. It is clear, from the comparison of Fig. 7-8c with the other cases, that the Pb in this position is very effective in reducing the nuclear heating. A final option was considered where the $W/B_{10}H_{14}$ shield thickness was increased by 2 cm (keeping the W to $B_{10}H_{14}$ ratio the same). Fig. 7-8d reveals that a remarkable decrease in the fast neutron fluence and the total nuclear heating is achieved in this case. Therefore, the nuclear heating in the S/C magnet can be reduced by increasing the thickness of the optimal $W/B_{10}H_{14}$ shield which is more effective than using $W/B_{10}H_{14}$ and Pb shields. This conclusion is in agreement with previous

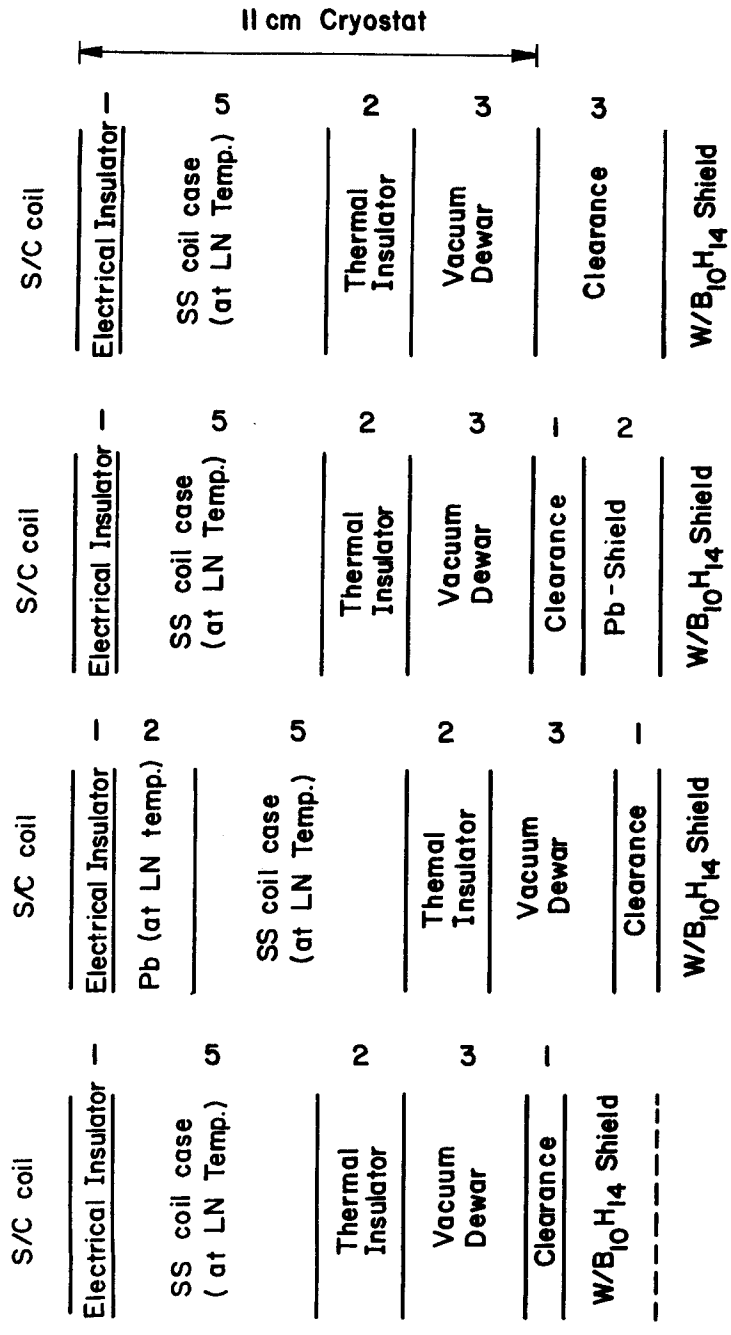

	Fluence (10^{19}n/cm^2)	Peak Nuclear Heating (mW/cm^3)	Total Nuclear Heating (W/m)
a)	3.94	1.31	1127
b)	3.54	1.24	957
c)	3.73	0.99	931
d)	2.74	1.07	791

Fig. 7-8. Modified cryostat to reduce the nuclear heating in the S/C magnet.

studies[5,6] in which the shielding effectiveness of the Pb was examined. The analysis was carried out for the $W/B_{10}H_{14}$ shield and is expected to hold true for the other optimal shields.

The optimization study was performed for 10 MW/m^2 neutron wall loading. The actual wall loading at the inboard shield varies between 3 and 9.3 MW/m^2 (see Section 5.3.2). Decreasing the wall loading by a factor of 2 will thin the shield by ~ 0.04 m.[6] Thus, parts of the inner leg of the S/C magnet where the wall loading is less than 10 MW/m^2 are slightly overshielded. Also, in the regions above and below the normal magnet the S/C magnet is overshielded since tungsten is more effective than the normal magnet materials in attenuating the radiation.

As mentioned in Section 5.3.3, using a neutron multiplier (such as Pb, Be) in the first layers of the inboard shield enhances the tritium breeding in the outboard blanket. The effect of replacing the front W-shield layers above and below the normal magnet region (where the S/C magnet is overshielded) by Pb or Be-shield is shown in Fig. 7-9. The Pb-shield acts slightly better than the Be-shield, and is less expensive. Thus, the front 13 cm thick layer of the W-shield can be replaced by the Pb-shield and the design limits for the S/C magnet are still all met.

7.4 Outboard Shield

The outboard shield is designed to protect the outer leg of the S/C magnet. It backs up the breeding blanket and performs the dual function of reflector and shield. The space is not an overriding constraint in the outboard side. The radial dimension of the S/C magnet is determined by maintenance considerations to provide enough space between the coils to allow for removing the blanket modules.

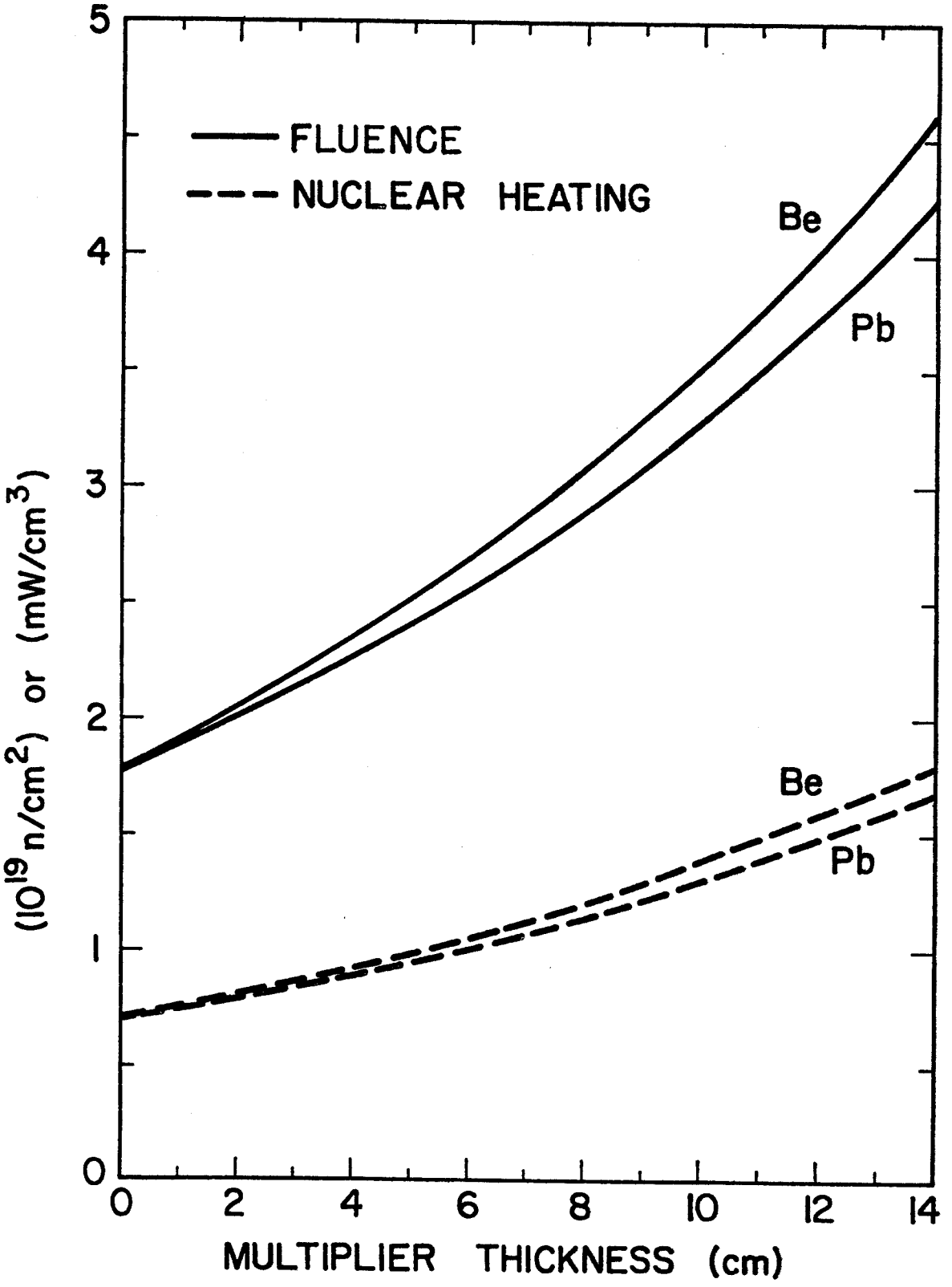

Fig. 7-9. Effect of replacing the front layers of W-shield above and below the normal magnet region on the fast neutron fluence and peak nuclear heating in the S/C magnet.

The 1-D calculations show that 0.5 m of reflector/shield (90 vol.% Fe 1422, 10 vol.% H_2O) adequately protect the S/C magnet. Although the reactor configuration discussed in Section 5.2 indicates that the outboard legs of the S/C magnet are not directly behind the blanket modules, the reflector/shield was designed to protect the corners of the magnet adjacent to the blanket modules (point A, Fig. 7-10). The space between the blanket modules is filled with shielding material and the radiation effects at the midplane of the S/C magnet (Section I, Fig. 7-10) are listed in Table 7-2.

Table 7-2. Peak Radiation Effects in the Outer Leg of the S/C Magnet

(12 MW/m^2 at the outboard blanket)

	At Corner (point A)	At Midplane (Section I)
Fast neutron fluence (n/cm^2)	1.13×10^{19}	3.47×10^{15}
Nuclear heating (mW/cm^3)	0.685	1.84×10^{-4}
dpa in Cu stabilizer (dpa/FPY)	2.39×10^{-4}	7.80×10^{-8}
Dose in GFF poly. (rad)	3.69×10^{9}	9.90×10^{6}

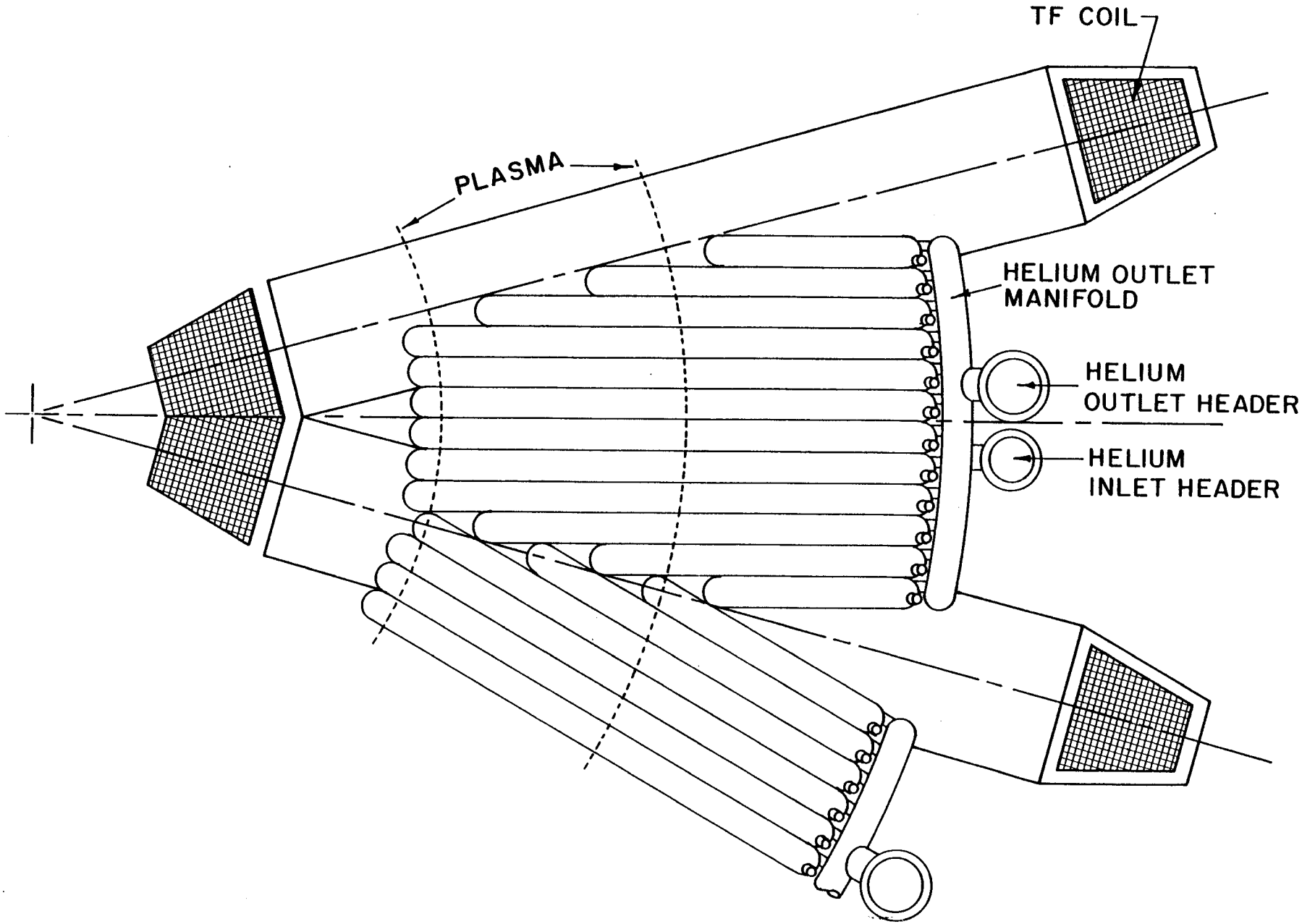

Fig. 7-10. Top view of the reactor showing the two extreme cases of the radiation effects in the outer leg of the S/C magnet.

References for Section 7

1. R.D. O'Dell et al., "User's Manual for ONEDANT: A Code Package for One-Dimensional, Diffusion-Accelerated, Neutral Particle Transport", LA-9184-M, Los Alamos National Laboratory (Feb. 1982).

2. L.A. El-Guebaly and E.M. Larsen, "Boron Hydride: New Material for Fusion Reactor Shielding Applications", ANS Trans. 47 (1984).

3. Gmelin, Handbuch der Anorganische Chemie Band 54, Borverbindungen Teil 20, Bor-Wasserstoff Verbindungen, Springer-Verlag Berlin (1979).

4. Von Stackelberg et al., Electrochem. 43, 21 (1937).

5. L.A. El-Guebaly et al., "MARS Axicell Radiation Damage and Shielding Analysis", Nuclear Technology/Fusion, 4, No. 2, Part 3, p. 1171 (1983).

6. H. Attaya, L. El-Guebaly, G. Emmert et al., "Blanket and Shielding Considerations for Advanced Tokamak Reactor Concepts", University of Wisconsin Fusion Engineering Program Report UWFDM-562 (Nov. 1983).

8. SUPER DESIGN CODE INTERFACE DEVELOPMENT

In all of the design processes of magnetic fusion reactors, information exchange is needed between the different plasma physics, magnet, neutronics, etc., computer codes. There could be possible error and/or a great deal of work in the process of feeding this information from one or more codes to another. To avoid that, and to make the design process as accurate as possible, we should have a fusion design code that takes over control of all the best codes that are usually used in the design, prepares their inputs, runs them, interprets their output and make their output available as input for other codes that need them. It is also possible for the design code to run the different codes in an iterative scheme to meet a prespecified design point. The existence of such a code would not eliminate the need for system codes like the one we used in this project (TSC-FEDC). Usually such system codes contain a very simplified models for physics, magnets, etc. This allows one to perform inexpensive parametric surveys to chose initial design parameters, and from there the design code would verify this design point.

We have accomplished important steps in this desired and required goal; these are described briefly below, with more details to be published in the near future.

8.1 MIG: MCNP Input Generator Code

The computer code MIG prepares the input for the neutronic code MCNP[1] from the input of the magnet design code EFFI.[2] EFFI has been the most widely used magnet code in the magnet design of both tokamak and mirror devices. MCNP, on the other hand, is a sophisticated, and probably the most accurate 1-D, 2-D and 3-D neutronic code. MIG prepares all the required surfaces and cells that are needed to simulate all the magnets in the device.

With small modification of the input of EFFI, MIG can take care of the symmetry, and according to user request it can add on the winding pack layers with different materials and thicknesses that represent the dewar, the helium gap, etc.

Y. Gohar (ANL) has used MIG to obtain the MCNP input for all the magnets in the Fusion Power Device (FPD). To this input he added the input that represents the halo and the blanket shield. This work of Gohar is the first complete 3-D neutronic analysis for c-shaped coils. Figure 8-1 shows results of Gohar's work.

8.2 NIG: Nastran Input Generator Code

NIG is a computer code that generates NASTRAN (stress analysis code) input from the input and the output of EFFI. Currently NIG can produce two types of NASTRAN elements. These are the beam element and the hexa element. Figure 8-2 shows NASTRAN output that uses NIG output for hexa elements which represent the ATF (Advanced Toroidal Facility at ORNL) coil.

8.3 NEWLIT: Neutron Wall Loading In Torus

This code calculates the uncollided neutron current (wall loading) and flux in toroidal systems. The code can be easily incorporated in systems or design codes to obtain the poloidal variation of the wall loading in toroidal systems. Neutron wall loading can be calculated either by Monte Carlo codes such as MCNP,[1] which by their statistical nature are very expensive, or by codes that use deterministic methods, which are limited either to circular or D-shape plasma and allow for few limited first wall shapes.[3,4]

NEWLIT uses ray tracing techniques to determine the extent of the plasma contribution to the neutron current and flux at a given point at the wall. These quantities are then determined by numerical integration over that plasma

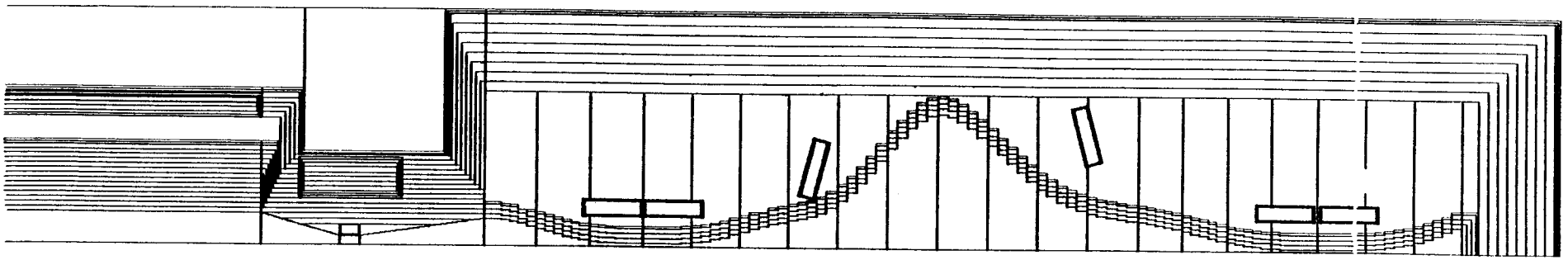

z-x plane

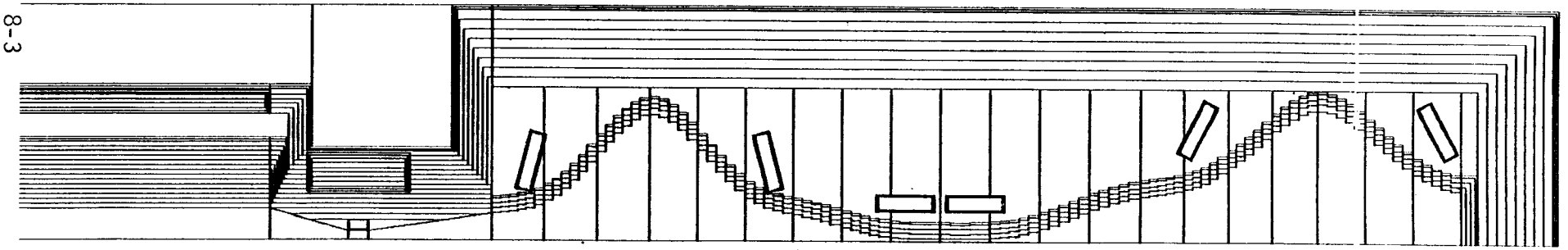

z-y plane

Fig. 8-1. Application of MIG.

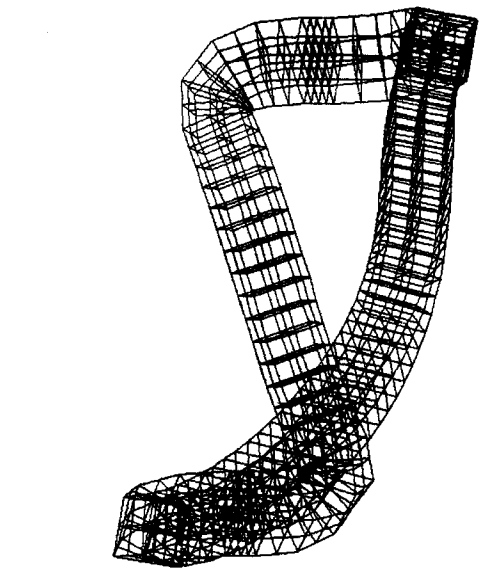

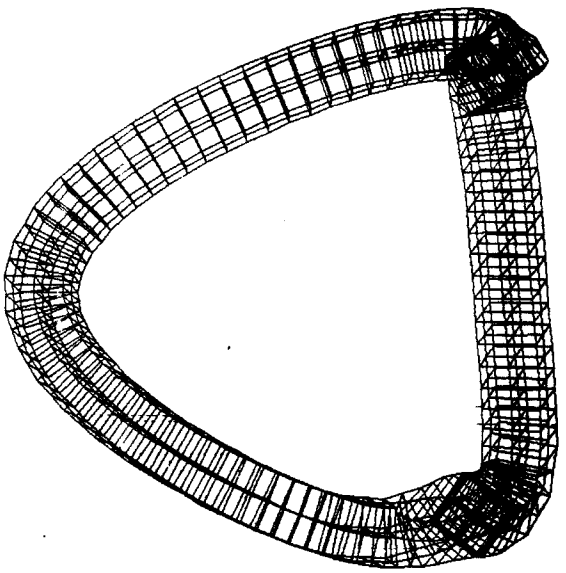

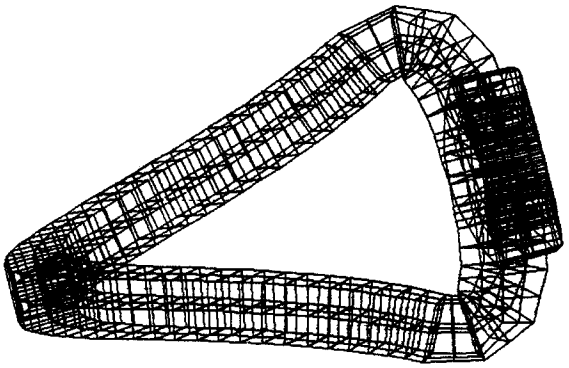

Fig. 8-2. Application of NIG.

zone. The source distribution within the plasma is taken into account by properly representing the different magnetic flux surfaces. The boundary of the plasma as well as the first wall can take any shape.

Figure 8-3 shows a comparison between the results of NEWLIT and the results from MCNP for the neutron wall loading of INTOR. The substantial agreement between the two codes is obtained with NEWLIT computer time that is about two to three orders of magnitude less than MCNP computer time. Figure 8-4 shows the poloidal wall loading distribution for STARFIRE and INTOR. Figure 8-5 shows a comparison between the wall loadings of a D-shape and a bean-shape plasma with the same fusion power.

References for Section 8

1. "MCNP - A General Monte Carlo Code for Neutron and Photon Transport," LA 7396-M, Los Alamos National Laboratory (1981).

2. S.J. Sackett, "EFFI - A Code for Calculating the Electromagetic Field, Force and Inductance in Coil Systems of Arbitrary Geometry," UCRL-52402 (1978).

3. W. Price and D. Chapin, "Neutron Wall Loading Distributions in Circular Cross Section Tokamak," MATT-1102, Princeton University (1975).

4. W. Dänner, "Neutron Flux Asymmetry in Toroidal Geometries," Max-Planck Institut für Plasmaphysik Report IPP-4/102 (1972).

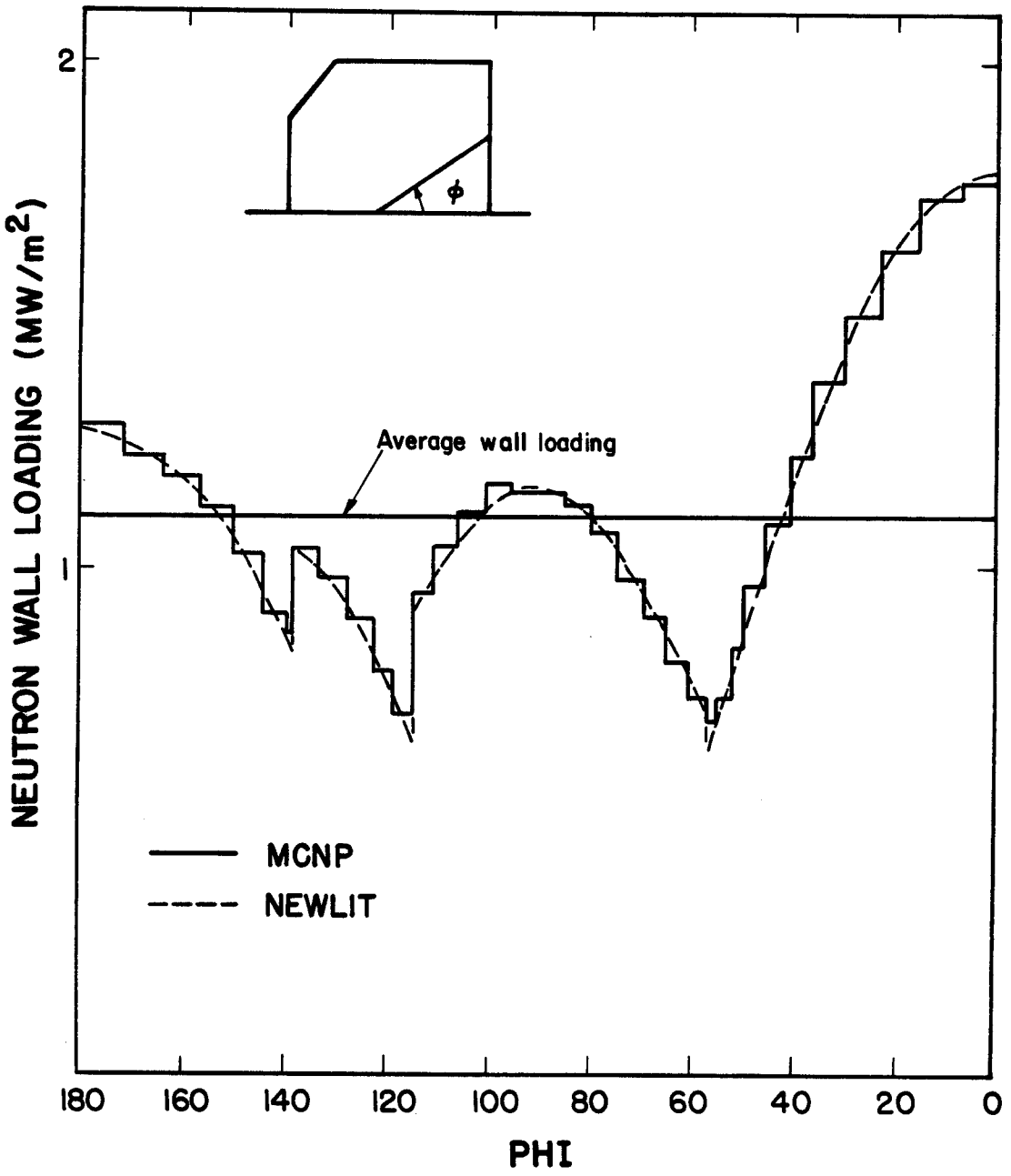

Fig. 8-3. Neutron wall loading in INTOR.

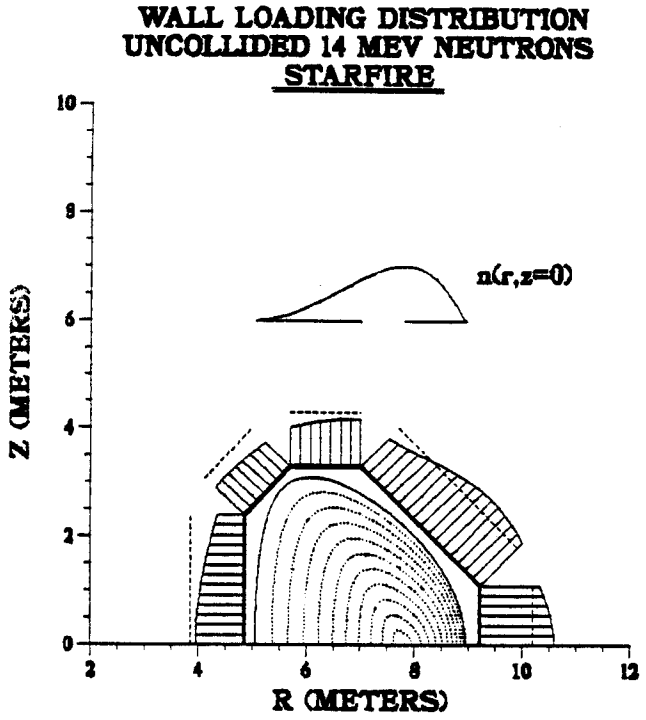

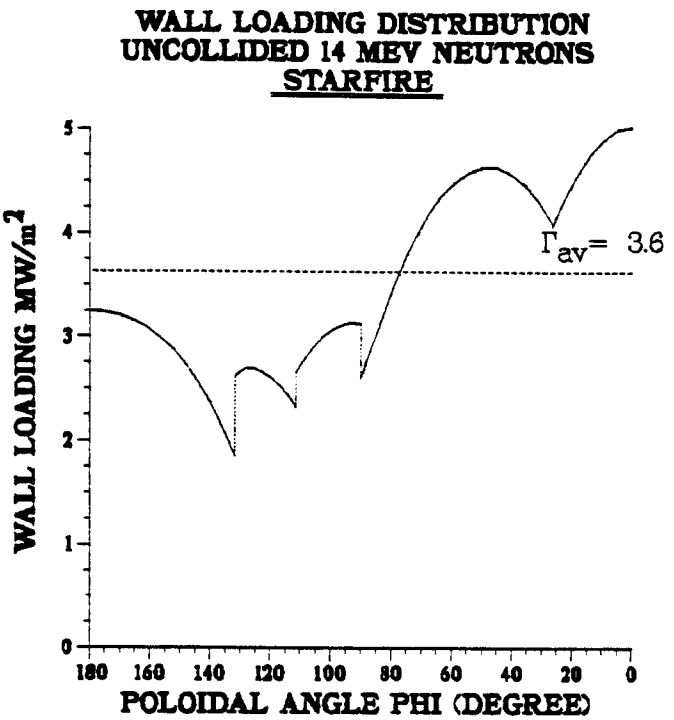

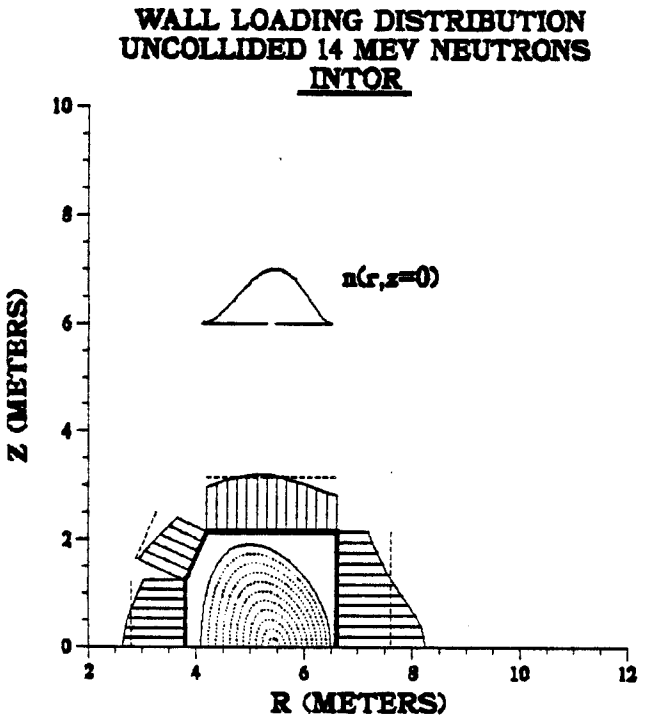

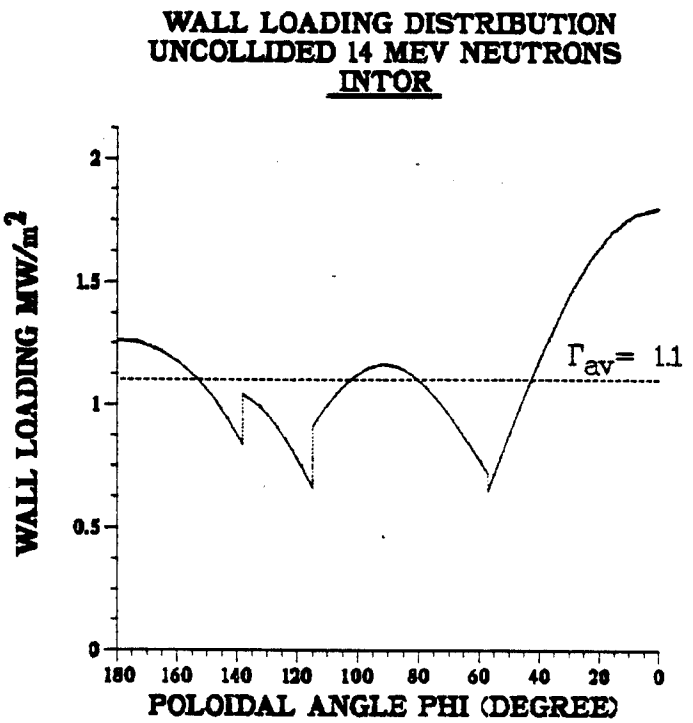

Fig. 8-4. Neutron wall loading in STARFIRE and INTOR.

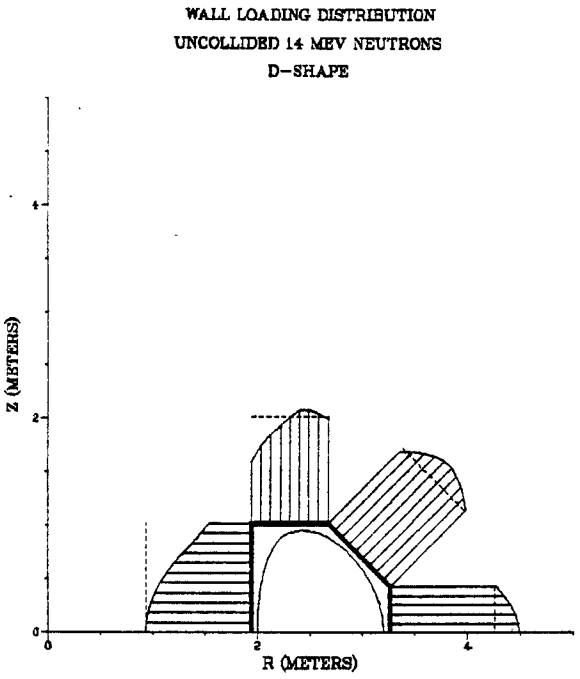

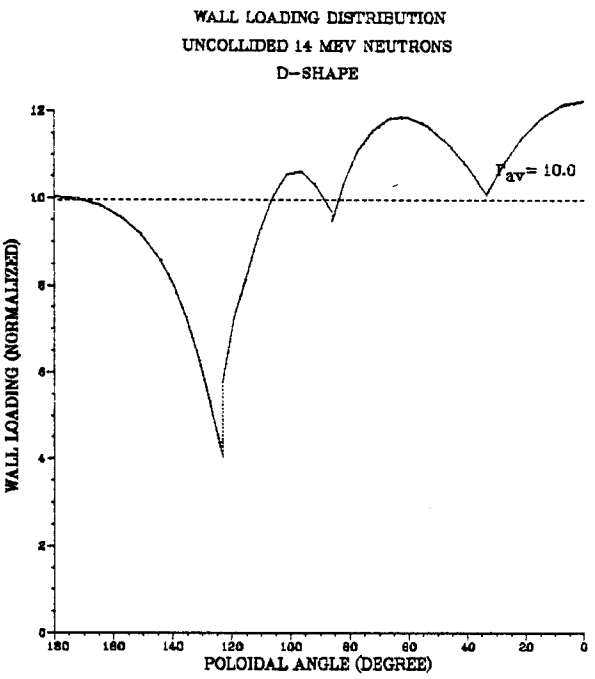

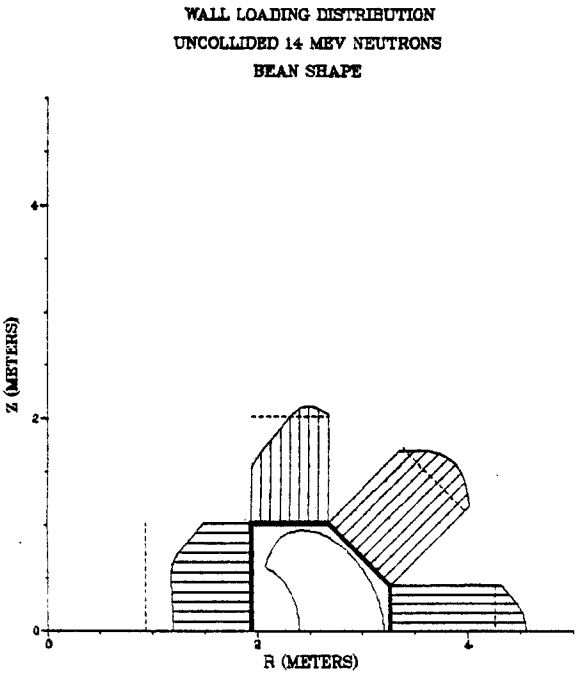

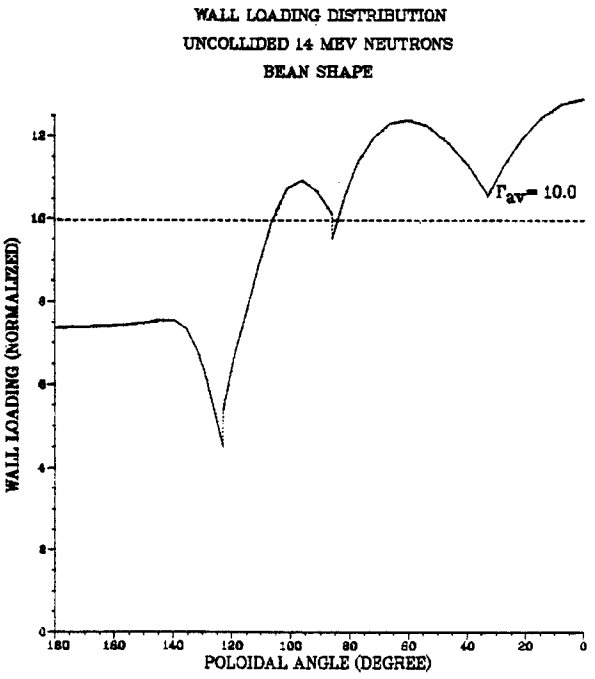

Fig. 8-5. Neutron wall loading for D-shape plasma and for bean-shape plasma (same fusion power).

9. SUMMARY

This study has focused on some innovations which would produce a more desirable and economical tokamak reactor than more conventional designs. In particular, the exciting new possibility of reaching very high beta regimes using bean shaped plasmas led to a concentration on compact reactors. Compact was defined here as a system having high power density, high wall loading, and low mass utilization. This may be the best way to realize the advantages of high beta without requiring very large unit size reactors.

The general conclusion that a compact reactor represents the most effective means of utilizing high beta resulted from the parametric studies conducted in this study. Parameter space was investigated and led, along with the neutronics calculations, to a reference case for the other areas of the study. The parameters varied included neutron wall loading, average beta, toroidal field, inboard shield thickness, plasma radius, and aspect ratio. To accomplish the parametric survey, the FEDC tokamak system code was modified and used.

In order to reach the reference operating point, a scenario was envisioned in which the plasma contour would continuously vary from a low beta D-shape to a high beta D-shape, with a high beta "bean" shape as an intermediate stage. MHD equilibrium calculations were done while seeking a suitable poloidal field (PF) coil set. In this phase of the study, a potentially severe difficulty for small radius, high beta plasmas was identified: If the PF coils, except for one bean coil, must not interlock the toroidal field (TF) coils, the PF coils may simply be too far from the plasma to adequately shape the contour. This tentative conclusion must be checked by other numerical codes and further work.

In defining a reference point, the computer code used in this study assumed INTOR confinement scaling for the plasma. A variety of more recent scaling laws exist, and their impact on the design was assessed. In general, unless one of the most pessimistic scalings is used, the reference point has an adequate ignition margin.

A high power density tokamak blanket was designed which appears to be safe, maintainable, easily fabricated, and which may last for a reasonably long time. The blanket is made from large bore HT-9 tubes which contain static $Li_{17}Pb_{83}$ cooled by helium gas. Tritium is removed from the breeder by diffusion through the coolant tube wall to the helium and then oxidized. This high wall loading (HWL) blanket should have general applicability in future tokamak designs.

The advanced shielding designs for the inboard region of this system represent a significant step forward. The use of boron hydride or titanium hydride significantly reduces the thickness of shield required to protect the magnets from radiation damage or excessive nuclear heating. The designs evolved in this study should also have applicability in near term facilities such as TFCX and INTOR.

Several advances were made in the area of large computer code development. As a result of this study two interfaces were established among important computer codes. The first one is MIG which couples the EFFI and MCNP codes, and the second interface is NIG which couples the EFFI and NASTRAN codes. These interfaces greatly facilitate the transfer of information among those codes. An efficient neutronics code was developed to describe the poloidal variation of neutron wall loading given an arbitrary plasma shape.

This code will be quite valuable for future parametric studies because it allows the peak wall loading to be calculated with a minimum of computer time.

Finally, progress was made on a broad front of understanding the benefits, and drawbacks of utilizing high beta plasmas in tokamaks. The fact that a completely self-consistent reactor design was not evolved only reinforces the difficulty of this area of research and the need to devote larger efforts in the future. Hopefully, this study will have contributed some of the tools and understanding needed to solve these problems.